ELECTRON SPIN RESONANCE SPECTROSCOPY OF INORGANIC AND BIOLOGICAL MOLECULES

By

CLIFTON HOWARD DURHAM, JR

A DISSERTATION PRESENTED TO THE GRADUATE COUNCIL OF
THE UNIVERSITY OF FLORIDA
IN PARTIAL FULFILLMENT OF THE REQUIREMENTS FOR
THE DEGREE OF DOCTOR OF PHILOSOPHY

UNIVERSITY OF FLORIDA

1974

to

My Parents

ACKNOWLEDGEMENTS

The author extends his deep appreciation to Professor William Weltner, Jr., whose encouragement, professional guidance, and resolute patience made this work possible. Thanks are also due to the other members of the author's Supervisory Committee, Professors W.S. Brey, Jr., S.O. Colgate, E.J. Gabbay, and K.C. Leibman, for their advice and support during the course of this work. The author acknowledges a special debt of gratitude to Dr. J.M. Brom, Jr., for his collaboration, constant support, and numerous informative discussions during the matrix isolation portion of this work.

The author would also like to thank the members of Professor Weltner's research group, particularly K.I. Dismuke, W.D. Hewett, J.V. Martinez, and D.C. Schloenagle, for their support and helpful discussions during the past four years. The author greatly appreciates the expert discussions about and the superb fabrication of experimental apparatus given by A.P. Grant, J.L. Soles, D.J. Burch, C.D. Eastman, and R.D. Ottinger.

The completion of this dissertation would not have been possible without the love and support of the author's wife, Susan, to whom the author extends a very special appreciation.

The author would also like to acknowledge the support of the Air Force Office of Scientific Research (AFOSR) and the National Science Foundation (NSF) during this work.

TABLE OF CONTENTS

Page

ACKNOWLEDGEMENTS iii

LIST OF TABLES vii

LIST OF FIGURES ix

ABSTRACT xii

INTRODUCTION ELECTRONIC SPIN RESONANCE SPECTROSCOPY OF INORGANIC AND BIOLOGICAL MOLECULES 1

PART ONE ELECTRON SPIN RESONANCE AND OPTICAL SPECTROSCOPY OF DIATOMIC NIOBIUM OXIDE IN INERT MATRICES AT 4°K ESTABLISHMENT OF ITS GROUND ELECTRONIC STATE 3

Chapters

I INTRODUCTION: THE NbO MOLECULE 3

- The Nature of the Problem 3
- The Importance of the Problem 3
- The Technique of Matrix Isolation 10
- Electron Spin Resonance Spectroscopy 16

II EXPERIMENTAL: THE NbO MOLECULE 23

- Materials 23
- Methods of Preparation of NbO 23
- Cryogenic Apparatus 25
- Spectrometer Instrumentation 33
- Experimental Procedures 34
- Experimental Problems 36

III THE ESR SPECTRUM OF THE NbO MOLECULE 39

- Introduction 39
- The General Hamiltonian 41
- The Spin Hamiltonian 45
- Angular Variation of the ESR Spectrum 49
- The Observed NbO Spectrum 54
- Consideration of the Expected g-Tensor for NbO 57

Page

Fitting the NbO ESR Spectrum 63
θ Versus H Curve 67
Forbidden Transitions 90
Site Effects 93
Nuclear Electric Quadrupole and Zeeman Effects 97
Discussion: A-Tensor 103
Discussion: g-Tensor 110

IV THE OPTICAL ABSORPTION SPECTRUM OF THE NbO MOLECULE 114

The Blue System ($^4\Sigma^- - {}^4\Sigma^-$) 114
The Red Systems 123
The Infrared Absorption Spectrum 133

V CONCLUSIONS: THE NbO MOLECULE 136

Results 136
Comparison with Other Diatomic Oxides 136

PART TWO ELECTRON SPIN RESONANCE SPECTROSCOPY OF PHENOTHIAZINE RADICAL CATION COMPLEXES WITH DEOXYRIBONUCLEIC ACIDS 138

VI INTRODUCTION: TRICYCLIC ANTIPSYCHOTIC DRUGS AND NUCLEIC ACIDS 138

Tricyclic Antipsychotic Drugs 138
Nucleic Acids 144
The Interaction of DNA with Other Molecules 152
Drug-Macromolecular Interactions 161

VII EXPERIMENTAL: INTERACTION OF PHENOTHIAZINE DRUGS WITH NUCLEIC ACIDS 164

Materials 164
Methods of Preparation 164

VIII THE EXPERIMENTAL FLOW SYSTEM FOR STUDY OF PHENOTHIAZINE DRUG RADICAL COMPLEXES WITH DEOXYRIBONUCLEIC ACID 171

Cavity and Sample System Considerations 172
The Flow System 186
Fluid Mechanical Considerations 194
Analysis and Discussion of Results 196

IX THE ESR SPECTRA OF PHENOTHIAZINE DRUG RADICAL COMPLEXES WITH DNA 212

Page

The Experimental Spectra . . . 212
Discussion: A-Tensor . . . 214
Discussion: g-Tensor . . . 223
The Observed Magnetic Parameters . . . 225
Computer Simulation . . . 231
Concluding Remarks . . . 238

APPENDIX A DIAGONALIZATION OF THE NbO EFFECTIVE SPIN HAMILTONIAN . . . 240

APPENDIX B COMPUTER TECHNIQUES FOR THE NbO MOLECULE . . . 243

QSIGMA2 Program Listing . . . 252

BIBLIOGRAPHY . . . 260

BIOGRAPHICAL SKETCH . . . 272

LIST OF TABLES

Table		Page
I	ESR Lines Assigned to NbO in Ne and Ar Matrices	68
II	Transition Probabilities Relative to a Fully Allowed ESR Transition for $M_I = -5/2$ θ Versus H Curve	88
III	Transition Probabilities Relative to a Fully Allowed ESR Transition for $M_I = -7/2$ θ Versus H Curve	89
IV	Comparison of the Magnetic Parameters of VO and NbO	104
V	Comparison of Observed NbO Absorption Bands for the $^4\Sigma^-$ System in Gas and in a Ne Matrix at 4°K	116
VI	Observed NbO Absorption Bands for X System in a Ne Matrix at 4°K	117
VII	Unperturbed Band Positions and Vibrational Frequencies in Excited Electronic States of NbO $^4\Sigma^-$ and X Systems	120
VIII	Interaction Between Vibrational Levels of Upper Electronic States in $^4\Sigma^-$ and X Systems in NbO	121
IX	Observed Absorption Bands of NbO in a Ne Matrix at 4°K in the Region 540 to 740 nm	127
X	Observed Absorption Bands of $Nb^{16}O$ in an Ar Matrix at 4°K in the Region 540 to 740 nm	129
XI	Comparison of $Nb^{16}O$ Spectra in Ne and Ar Matrices in the 540 to 740 nm Region with the Strong Bands Observed in the Gas Phase	130
XII	Varian E-3 ESR Spectrometer Scan Time Calibration Data for Use with Flow System	191
XIII	Variation in Measured Volume Flow Rates Using a 1-cc Syringe and FA378 Flow Cell for 90 Percent Flow and Range Setting X1	193
XIV	Dimensions (in inches) of Parallel Flow Cells Used with the Varian E-3 ESR Spectrometer	198

Table		Page
XV	Volumes of Flow Cells Used with the Varian E-3 ESR Spectrometer	199
XVI	Magnetic Parameters for DNA-Bound Radical Cations of Chlorpromazine (CPZ), Triflupromazine (TFP) and Methiomeprazine (MMP	227
XVII	Estimations of the Coefficients of the Nitrogen 2s and $2p_z$ Atomic Orbitals in the Molecular Orbital of the Odd Electron of DNA-bound Drug Radicals	230
XVIII	FORTRAN Implementation: List of Principal Variables	250

LIST OF FIGURES

Figure Page

1. Matrix isolation technique as applied to high-temperature molecules 12
2. Schematic diagram of inductively heated tungsten Knudsen cell 26
3. Basic design features of liquid-helium Dewar used for ESR studies. 28
4. Basic design features of liquid-helium Dewar used for optical studies 29
5. Basic design features of variable-temperature liquid-helium Dewar used for optical studies 30
6. The ESR spectrum of a linear molecule ($S = 1/2$) randomly oriented in a solid matrix 52
7. ESR spectrum of NbO isolated in a Ne matrix at 4°K. 55
8. ESR spectrum of NbO isolated in an Ar matrix at 4°K. 56
9. The "apparent" g-values for ESR transitions of a $^4\Sigma$ molecule as a function of the spin-spin coupling parameter $D/g_e\beta_e B_o$ 62
10. ESR spectrum of NbO isolated in a Ne matrix at 4°K. 69
11. ESR spectrum of NbO isolated in an Ar matrix at 4°K. 70
12. Linear molecules oriented in a matrix with their axes parallel to the flat surface of the sapphire rod 71
13. Coupling of nuclear spin angular momentum $\bar{I}$ and electronic spin angular momentum $\bar{S}$ in (a) a weak magnetic field $\bar{H}$ and (b) a strong magnetic field $\bar{H}$ 73
14. Energy levels and X-band transitions for $S = 1/2$, $I = 9/2$ for the spin Hamiltonian discussed in the text 84
15. θ versus resonance field 87

Figure Page

16. Orientation of NbO molecules with respect to the plane of the sapphire rod when viewed from (a) a line normal to the rod surface and (b) along the plane of the rod 95

17. Schematic molecular orbital diagram for the valence electrons of NbO 108

18. The observed $^4\Sigma^-$ and perturbing X systems of NbO in an Ne matrix at 4°K. 115

19 Vibrational levels in the excited electronic states of NbO $^4\Sigma^-$ and perturbing X systems and their interactions. 118

20. The observed $Nb^{16}O$ absorption bands in the region 540-740 nm in a Ne matrix at 4°K 124

21. The observed $Nb^{16}O$ absorption bands in the region 540-740 nm in an Ar matrix at 4°K. 126

22. The observed $Nb^{16}O$ and $Nb^{18}O$ infrared absorption bands in a Ne matrix at 4°K. 134

23. Schematic representation of the Watson-Crick-Wilkins double helix of DNA with planar aromatic molecules intercalated between adjacent nucleotide base pairs 156

24. Schematic representation of a rectangular parallelpiped TE_{102} microwave cavity illustrating both electric and magnetic field contours within the cavity. 174

25. Schematic diagram of Teflon cell frame for perpendicular flow through the Varian E-3 microwave cavity 179

26. Schematic diagram of Teflon cell frame for parallel flow through the Varian E-3 microwave cavity. 180

27 Details of DPPH probe used with parallel and perpendicular flow cells to allow g-factor determinations 184

28. Schematic representation of flow system as used with the Varian E-3 ESR spectrometer, showing syringe pump, cell arrangement, microwave cavity, and collection tube. 189

29 Relationships among the various parameters of the flow system used with the Varian E-3 ESR spectrometer. 201

30 Comparison of parallel flow ESR spectra obtained using the PA14A and PA37B cells discussed in the text, illustrating the effect of different cell designs on the observed spectrum 203

Figure Page

31. Parallel flow ESR spectra obtained using the PA37B cell discussed in the text, illustrating the effect of increasing rate of shear on the spectrum observed. 206

32. Comparison of perpendicular flow ESR spectra obtained using the PE1A and PE3B cells discussed in the text. 207

33. Effects of varying the nucleotide base pair to radical drug cation ratio (NP/R) on the observed orientation effects, illustrating their dependence on solution viscosity. 210

34. X-band ESR spectrum of the chlorpromazine radical cation complex with salmon sperm DNA. 213

35. X-band ESR spectrum of the triflupromazine radical cation complex with salmon sperm DNA. 215

36. X-band ESR spectrum of the methiomeprazine radical cation complex with salmon sperm DNA. 216

37. X-band ESR spectrum of the chlorpromazine radical cation complex with calf thymus DNA 217

38. Computer simulated spectrum of the chlorpromazine radical cation complex with DNA (random orientation). 232

39. Computer simulated ESR spectra of the random orientation of complexes of the radical cations of chlorpromazine, triflupromazine, and methiomeprazine with salmon sperm DNA. 234

40. Flow diagram of program QSIGMA2 used to solve spin Hamiltonian matrix for NbO. 246

41. Flow diagram of subroutine EIGN used in program QSIGMA2 to diagonalize spin Hamiltonian matrix for NbO. 248

Abstract of Dissertation Presented to the Graduate Council of the University of Florida in Partial Fulfillment of the Requirements for the Degree of Doctor of Philosophy

ELECTRON SPIN RESONANCE SPECTROSCOPY OF INORGANIC AND BIOLOGICAL MOLECULES

By

Clifton Howard Durham, Jr.

December, 1974

Chairman: Professor William Weltner, Jr.
Major Department: Chemistry

NbO molecules, produced by the vaporization of a mixture of Nb metal and solid Nb_2O_5 or by passing O_2 gas over hot Nb metal, were trapped in solid neon or argon at 4°K and investigated by electron spin resonance (ESR) and optical spectroscopy. Analysis of the ESR spectrum established that the molecule has a $^4\Sigma^-$ ground electronic state (derived from a $\delta\sigma^2$ configuration) exhibiting large nuclear hyperfine splittings from interaction with the $^{93}Nb(I = 9/2)$ nucleus. Essentially all lines were accounted for as effectively $\Delta M_I = 0, \pm 1, \pm 2$ transitions (or as multiple trapping sites). Nuclear hyperfine and g-tensor elements have the following values in a neon matrix: $g_{||} = 2.0023$, $g_{\perp} = 1.9577$, $A_{||}(^{93}Nb) = 1587$ Mhz, and $A_{\perp}(^{93}Nb) = 1647$ MHz. The magnetic parameter b, found to be approximately $0.15\ cm^{-1}$ in the gas-phase optical spectrum, is here determined to be $0.165\ cm^{-1}$. These magnetic parameters are in accord with the expected electronic properties of NbO (assuming the A values are positive) and are compared with those of VO. Both $Nb^{16}O$ and $Nb^{18}O$ have been investigated by optical spectroscopy and the spectra correlate well with gas-phase

data. The $^4\Sigma^- \leftarrow X^4\Sigma^-$ blue system appears at 461.4 nm in a neon matrix and contains several vibrational perturbations. At least five systems of bands appear between 540 and 740 nm. It is conjectured that the progression with (0,0) at 655.3 nm is a $^4\Sigma^- \leftarrow X^4\Sigma^-$ transition and that the remaining bands arise from a $^4\Pi \leftarrow X^4\Sigma^-$ system where the upper state is partially Hund's case (c) coupling. In the infrared the vibrational transition of Nb^{16}O appears as a triplet at 965.5, 973.0 and 977.1 cm^{-1} in neon; a similar triplet was recently observed by other workers in argon matrices.

A flow system has been developed for use with TE$_{102}$ rectangular parallelepiped microwave cavities which is useful in ascertaining whether or not planar aromatic radicals interact with double helical nucleic acids through an intercalative mode of binding. The apparatus has been used to demonstrate intercalation of the radical cations of the phenothiazine drugs chlorpromazine, triflupromazine, and methopromazine with calf thymus and salmon sperm DNA. The observed ESR spectra are readily interpreted in terms of Lerman's intercalation model in which the planar aromatic phenothiazine system intercalates between adjacent nucleotide base pairs by local extension and unwinding of the DNA helix. The anisotropy exhibited by the g- and A-tensors of the DNA-bound radical cations is that expected for planar aromatic systems in a pseudopolycrystalline environment. The data indicate delocalization of the unpaired electron in the DNA-bound radicals and are fully explained by the assumption that the plane of the radical is perpendicular to the DNA helical axis. The development of these experimental technique provides a convenient method which may be extended to further studies with other phenothiazine drugs (or other paramagnetic intercalating agents) and various types of nucleic acids or complexes.

INTRODUCTION

ELECTRON SPIN RESONANCE SPECTROSCOPY OF INORGANIC AND BIOLOGICAL MOLECULES

As its title implies, this study is concerned with electron spin resonance (ESR) spectroscopy as applied to two rather different areas of interest. Therefore, this study is divided into two parts. Part One is concerned with determining the electronic ground state of diatomic niobium oxide, NbO, through the use of ESR spectroscopy. The results of the ESR work are supplemented by results from optical spectroscopic techniques. Part Two is concerned with the interactions of radical ions derived from tricyclic antipsychotic drug molecules with deoxyribonucleic acid (DNA), the macromolecule now known to be the carrier of genetic information in cellular nuclei. These interactions have been studied by utilizing ESR spectroscopy and other techniques.

The reason for uniting results from two such diverse areas into one comprehensive study is twofold. First, as detailed in the appropriate sections which follow, each area is of great importance and interest in itself. Secondly, this study is meant to illustrate how one experimental technique, in this case electron spin resonance spectroscopy, can be used to obtain vital and relevant information in two seemingly dissimilar areas. Clearly the end result of such a study is also twofold. Not only is vital and relevant information obtained concerning the two problems, but the researcher is also afforded the opportunity to study and apply a particular technique to a broad degree, thereby adding an understanding more thorough in its content than is possible by applying a given experimental method to only one small area of its applicability

This philosophy is entirely appropriate to both the spirit of modern technology and the nature of this particular study.

PART ONE

ELECTRON SPIN RESONANCE AND OPTICAL SPECTROSCOPY OF DIATOMIC NIOBIUM OXIDE IN INERT MATRICES AT 4°K: ESTABLISHMENT OF ITS GROUND ELECTRONIC STATE

CHAPTER I

INTRODUCTION: THE NbO MOLECULE

The Nature of the Problem

The ground state of NbO has not been established as $^4\Sigma^-$ (derived from a $\sigma\delta^2$ configuration), but a recent gas-phase study [1] and an infrared investigation in argon matrices [2] support such an assignment. VO, the lightest Group VB diatomic oxide, has been found to have a $^4\Sigma^-$ ground state [3] while the heaviest of these oxides, TaO, has a $^2\Delta_r$ ground state derived from a $\sigma^2\delta$ configuration [4-6]. As in the Group IVB diatomic oxides, TiO, ZrO, and HfO, there is effectively a transposition of the occupied σ and δ molecular orbitals down the Periodic Table, but in that case it appears to occur at ZrO [7]. Earlier studies of the NbO molecule in the gas phase [8,9] were unable to establish definitely the nature of the ground state.

The Importance of the Problem

The question naturally arises as to why knowledge of the ground electronic state of the NbO molecule is desirable other than as an intellectual exercise. There are numerous molecules which are observed only under the high-temperature conditions such as those which exist in the atmospheres of stars, in arcs, and in the vapor phase over very refractory solids [10]. Spectroscopic studies of the molecular species from such sources are in general quite difficult. The molecules are thermally excited into many rotational and vibrational levels, which severely broaden the observed spectral bands and significantly increase their number. Furthermore, even if the analysis problems can be solved, unambiguous determination of the ground electronic state is usually not possible because of other low-lying electronic states significantly populated at the high temperatures. Such species cannot be observed at lower temperatures if experiments are limited to study of the gas phase, but it is possible to trap such molecules in an inert, transparent solid at lower temperatures and then study the trapped molecules. Studies of molecules in such an environment can provide valuable information despite the influence of the inert medium. But why are such studies important?

Stellar and Interstellar Molecules

Stars in the same class as the sun and all cooler stars usually exhibit the spectra of molecules in their atmospheres [11-13]. The sun is a type G star, that is, the yellow star characterized by a temperature of about 6000°K [11]. The disk of the sun is too hot for many molecules to exist there, but its proximity to earth mitigates the effects of low molecular populations and weak molecular spectra. Sunspots are at a lower temperature and observations of these regions have lead to the identification of 11 molecules [10]: OH, NH, O_2, CH, CN, CO, C_2, MgH, SiH, TiO, and CaH. Inconclusive evidence has been obtained for the existence of several other molecules in the sun's atmosphere [10]: BH, ScO, BO, AlO, ZrO, YO, SiF, H_2, NO, SiO, and N_2. With surface temperatures of less than 3000°K, the cooler red stars of classes M, S, R, and N have more abundant molecular populations in their atmospheres. Molecules dominating the spectra of red stars are known to vary with the ratio of oxygen to carbon in their atmospheres [10]. Class M stars are characterized by a strong TiO spectrum exhibiting broad features at 458.5, 476.2, and 495.4 nm [11]. Class S stars exhibit strong ZrO bands [10]. Stars of classes R and N exhibit strong C_2 and CN spectra and are usually called type C or "carbon" stars. Other molecules are also identified in the spectra of stars of these classes [10]. Classes R and N have been found to contain C_2, CH, CN, NH, SiC_2, C_3, and H_2O; class S stars contain ZrO, LaO, YO, SiH, and TiO, and class M stars have been found to contain TiO, VO, MgH, SiH, AlH, ZrO, ScO, YO, CrO, AlO, BO, SiF, SiN, CN, CH, and C_2 molecules. There is also an important role played by molecules in the absorption of light from the inner regions (photosphere) of stars. This "blanketing" effect can seriously distort emitted radiation in certain wavelength regions when molecules such as TiO or C_3 are present in relatively large concentrations [10]. Clearly the study of such high-temperature species in controlled laboratory situations greatly enhances the efforts of astrophysicists in determining stellar compositions and in postulating the mechanisms of stellar chemistry.

It should also be noted that spectroscopic studies have enabled astrophysicists to identify a number of molecular species in the gas between the stars of the galaxy [14]. The first interstellar molecule, CH, was discovered in 1937, and the CH^+ radical, as well as the CN radical, was identified shortly thereafter in spectra taken in the vicinity of a few bright blue-white class O (temperature about 50,000°K) and class B (temperature about 25,000°K) stars [11,14]. In late 1968, interstellar molecules other than diatomics were discovered for the first time [14]. Although more complex molecules have been discovered since, finding NH_3 and H_2O

molecules established two prominent trends observed in interstellar molecular clouds [14]. First, such clouds are very dense in comparison with any other known interstellar region and, secondly, the physical conditions responsible for excitation of the molecules such that they radiate or absorb are very different from terrestrial conditions. Some conditions give rise to an interstellar maser, the predecessor of the laser in that it amplifies radio waves rather than visible light. Other conditions create what might be referred to as an interstellar refrigerator. In fact, at some wavelengths, a molecule such as H_2CO absorbs more energy than the surrounding conditions would seem to allow if the conditions are such that terrestrial laws of thermodynamics are to be applicable. Interstellar research efforts have provided two key conclusions that are quite intriguing [14]. First, formation of molecules per available atom in interstellar space must be a highly efficient type of process. Second, interstellar chemistry seems to favor production of carbon-containing molecules. All of the simplest organic molecules have been found in interstellar space, but many of the even simpler inorganic species such as NO, SO, and SH have never been detected despite meticulous searches. No explanation has yet emerged as to why interstellar chemistry is predominantly organic. Among the molecules that have been detected in interstellar space are the following [14]: CH and CH^+ in 1937, CN in 1939, OH in 1963, NH_3 and H_2O in 1968, H_2CO in 1969, CO, HCN, HC_3N, H_2, CH_3OH, and HCOOH in 1970, CS, NH_2CHO, OCS, SiO, CH_3CN, HNCO, CH_3CCH, and CH_3CHO in 1971, and H_2CS, H_2S, and CH_2NH in 1972.

Although the existence of Nb atoms in stellar atmospheres is well established, NbO, which may be present in cool stars, particularly those of class S in which Zr compounds are prominent, has not been identified [15]. NbO bands at 649.5, 647.4, 648.4, and 615.1 nm are masked by strong ZrO features. There are no NbO bands generally free of mixing with bands from other molecular species (such as ZrO), but at certain phases of a few red variable stars, masking by ZrO and YO is found to be minimal for the NbO bands at 648.4 and 655.1 nm [15]. Although Davis and Keenan [15] report mostly negative results in their study, for the star R Cygni, small dips are observed at 648.4 and 655.1 nm which should not be due to ZrO, YO, or TiO, and can, therefore, be due to NbO. The relevancy of the present study of NbO is obvious.

Refractory Metals and Modern Technology

There are other molecules that are not found in stars but which exist at the same high temperatures and derive their importance from modern technology. Refractory metals are those which are difficult to fuse, extrude, or extrude, and are capable of enduring high temperatures. It is precisely because of their high melting points that refractory metals (tantalum and tungsten, for example) and their oxides and carbides are vital to the missile and space industries. In the past, mass spectrometric studies have played a very important part in determining the molecular species vaporizing from such refractory metals at high temperatures and also have allowed determination of the thermodynamics of the process and the dissociation energies of the molecules. In the final analysis, however, it becomes necessary, for thermodynamic or other reasons, to know the more intimate properties of these high-temperature molecules [10]. Observing them trapped in a solid at 4°K has helped provide such information.

Niobium (called Columbium prior to 1950) was discovered in 1801 by Hatchett in his study of an ore sent to England more than a hundred years earlier by John Winthrop the Younger, first governor of Connecticut [16-18]. Niobium is always found associated with tantalum, and, in ore-dressing, is the last by-product in the form of $K_2NbOF_5 \cdot H_2O$. Extensive ore reserves are found in Africa, Canada, Norway, and the United States. A common process for the extraction of the metal is one in which a fixed quantity of oxide is converted to NbC by the addition of carbon black and subsequent heating in an inert-gas atmosphere. The carbide is then mixed with Nb_2O_5 and the mixture heated in vacuo, Nb metal being formed by the reaction [16] $Nb_2O_5 + 5NbC = 7Nb + 5CO$, since CO is insoluble in Nb. The maximum permissible impurity level for satisfactory Nb usually is 0.20 percent Ta, 0.002 percent Ti, 0.03 percent Si, 0.01 percent Fe, and 0.02 percent C [16]. Niobium is a white, soft, ductile metal which can be more easily worked than Ta and can be rolled so readily. Niobium metal can be punched and can be drawn even against the direction of rolling without splitting. Although Nb does not become so brittle as Ta when heated for short periods of time in air, all annealing processes must take place in vacuo. The metal takes on a bluish coat when exposed to air at ambient temperatures over a long time period and starts to oxidize in air at 200°C. Niobium is 50 percent more expensive volume for volume than tantalum [16], but is only half as dense. Its applications are usually limited to the most costly tubes (transmitter tubes, high-voltage rectifiers, and X-ray tubes) which make a high profit above the total cost. The metal is also used as an alloying agent in carbon and alloy steels as well as with nonferrous metals. These alloys have improved strength and other desirable properties. Niobium is used in arc-welding rods for stabilized grades of stainless steel. Niobium also has superconducting properties and a superconducting magnetic has been made with Nb-Zr wire, which retains its superconductivity in strong magnetic fields [16-18].

Thus, NbO falls into a class of molecules which have important implications in studies of stellar atmospheres and in modern metallurgical technology. Determination of a property such as the ground electronic state of this kind of molecule is readily apparent in view of the preceding discussions.

The Chemical Elements of Life

There is a third area in which it is interesting to speculate upon the importance of niobium. This area concerns the chemical elements of life itself. It was believed until recently that living matter incorporated only twenty of the natural elements, but it has now been shown that a role is played by four others, namely fluorine, silicon, tin, and vanadium [19]. Vanadium, of course, is the lightest of the Group VB transition metals and its chemical properties are similar to those of niobium, the next heavier element of the Group. The twenty-four elements now known to be essential to life are as follows [19]. H, C, N, O, F, Na, Mg, Si, P, S, Cl, K, Ca, V, Cr, Mn, Fe, Co, Cu, Zn, Se, Mo, Sn, and I. Nickel may soon be added to this list [19].

The element of most interest to the present work, vanadium, has been found to be essential in lower plants, certain marine animals, and rats [19]. Research has shown [19] that on a diet from which vanadium is totally excluded, rats suffer a retardation in growth rate of about 30 percent! Furthermore, normal growth can be restored by adding one tenth of a part per million of vanadium to the diet! At higher concentrations, vanadium is known to exhibit several adverse biological effects, but its essential role in trace amounts remains unestablished. High doses of vanadium block cholesterol synthesis and reduce the phospholipid and cholesterol content in the blood [19]. It also promotes the mineralization of teeth and is effective as a catalyst in the oxidation of many biological substances. Clearly it is not improbable that niobium also is an essential element of life and simply has not yet been discovered to fall into that category.

In many cases the exact role of trace elements such as vanadium remains entirely unknown, or at least unclear. This lack of knowledge could conceivably be critical in a period when the biosphere is being increasingly contaminated by synthetic chemicals and subjected to a possibly dangerous redistribution of salts and metal ions [19]. The current discovery of unusual chemical forms of metals (methyl mercury, for example) and a thoroughly complex series of competitive and synergistic relations among mineral salts leads to the realization that the human race is ignorant of many basic facts about how the chemical environment affects its biological fate [19]. The poet Archibald MacLeish described the earth as "a small . . planet . . . of a minor star off at the edge of an inconsiderable galaxy." To rise above such insignificance is the dream of science and it is through continuous study and efforts to understand the physical nature of the world that this will be achieved. Consequently, a knowledge of the ground electronic state of the NbO molecule is not merely an exercise to hone the intellectual axe, but is important in its own right as adding essential information to the existing body of scientific and technical data.

The Technique of Matrix Isolation

The study of high-temperature molecules such as NbO in a solid at 4°K has been mentioned in the preceding discussion. This method is called matrix isolation. Matrix isolation has been defined [10,20] as a technique for trapping molecules as isolated, noninteracting entities in an inert solid (matrix) in order to investigate their properties, usually by spectroscopic methods. The primary assumption of this technique is that the molecular information gained is gas-like within small limits. Extensive details and reviews of matrix isolation as applied to atomic and molecular studies are to be found in the literature [10,20-24]. The common technique of treating solid samples by diluting with KBr and forming a compressed disk of finely dispersed solid in a KBr matrix may be crudely considered as a progenitor of the present form of matrix isolation [23].

Matrix isolation is usually achieved by the simultaneous condensation (deposition) of gaseous sample material with a large excess (10^2 to 10^4 molar ratios) of inert material. The trapped molecules do not undergo extensive translational motion (diffusion) and are usually (but not always) prevented from rotating, but may vibrate with frequencies that are close to the gas-phase values. As a result, the spectra obtained are frequently much simpler than those obtained for any other state of matter, particularly if low temperatures are employed in the experiments [20-24].

One common form of matrix isolation requires the use of high-temperature Knudsen cells for the production of molecular species and cryogenically cooled surfaces for the trapping of these species in an inert-gas matrix. Such an arrangement is indicated schematically in Figure 1. Another method creates pseudo-high-temperature conditions by subjecting sample material to radiation from high-energy sources such as microwave or electric discharges, ultraviolet (UV) lamps, or gamma rays, or by electron or ion bombardment.

The matrix material itself can be any gas which will not react with the trapped molecule and which is readily and rigidly solidified. The rare gases are usually used because they are relatively inert and offer a wide range of melting points and atomic sizes. The common cryogenates

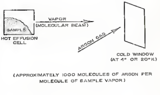

Figure 1 Matrix isolation technique as applied to high-temperature molecules.

(refrigerants) in use are liquid He (boiling point 4.2°K), liquid H_2 (boiling point 20.4°K), and liquid N_2 (boiling point 77.4°K). Pumping on the cryogenate can reduce these temperatures to 1.2°K for liquid He and 15°K for liquid N_2. The temperatures usually employed for matrix formation are about 20°K for Ar, Xe, Kr, and N_2, and 5°K for Ne. Neon can be used only with liquid He as the cryogenate since it melts at 24°K and diffusion in the solid state probably begins at about 12°K. The solid rare gases exhibit vapor pressures of roughly 10^{-10} torr at these low temperatures. The trapping surface is usually cooled by introducing a controlled leak of liquid or gaseous cryogenate to a cold block that is in good thermal contact with the trapping surface. Also in use are "Cryotips" utilizing the Joule-Thompson effect in the expansion of He or N_2 gas at high pressure. The most suitable trapping surfaces for the various spectroscopic regions are crystalline quartz or Si for the far infrared (IR), CsI, KBr, NaCl (IR), quartz, LiF (to 105 nm), CaF_2 (visible, UV), and sapphire rod or some other nonconducting material for electron spin resonance (ESR) studies. The choice of matrix gas is determined to a large extent by the effect the solid matrix will have upon the trapped molecule. The objective in matrix isolation is to trap the molecules in a condition as similar to the gas phase as possible; as expected, the matrix composed of the least-polarizable atoms perturbs the trapped molecule least. Neon is thus usually found to be the best matrix gas.

Advantages of Matrix Isolation

The primary advantage of making spectroscopic measurements on a molecule at 4°K lies in the fact that at such a low temperature the molecule is in its lowest energy state and vibrational or electronic transitions induced by appropriate electromagnetic radiation always begin from that level. Although this greatly simplifies the spectra that are obtained, the trapping of the molecule in the inert medium does cause some alteration of its properties. A variety of fundamental molecular properties can be obtained from matrix isolation studies: vibrational frequencies (IR), geometry (IR), electronic levels (near IR, visible, UV, vacuum UV), and spin densities and electronic configuration (ESR). The essential advantages of matrix isolation spectroscopy over gas-phase spectroscopy at the present time may be summarized as follows.

(a) The ability to observe normally unstable or highly reactive species at leisure.

(b) The ability to reduce and eliminate thermally induced rotational and vibrational excitation, particularly for high-temperature species. As a result, there are no "hot" bands and the vibrational bands are sufficiently narrow to allow accurate frequency measurements and permit generous use of isotopic substitution. Furthermore, the sensitivity is enhanced.

(c) The ability to build up sufficient concentration to observe species of low abundance or spectral features with low absorption coefficient.

(d) The ability to conduct controlled diffusion experiments in order to follow the production of polymers, possibly to the actual point of crystal formation, thereby obtaining information bridging the behavior of the molecular and solid crystalline states.

(e) The ability to make use of the preferential orientation of some species in matrices, which is particularly important in the case of high-temperature molecules since preparation of real single crystals of such molecules is quite impossible.

Disadvantages of Matrix Isolation

The disadvantages of the technique may be summarized as follows.

(a) The most common and readily identified disadvantage is the frequency shift from the gas-phase values, an effect observed for rotational, vibrational, and electronic transitions. Matrix vibrational shifts in Ne usually amount to about 4 percent. Frequencies in Ne matrices are often lower than the gas-phase values and frequently data from Ne and Ar matrices will bracket the gas data.

(b) The shapes and widths of bands vary greatly in matrices, depending upon the extent of the interaction between the isolated sample molecules and the matrix. In matrix absorption spectra the bands in a particular progression include transitions from the vibrational level $v'' = 0$ in the ground state to $v' = 0, 1, 2, \ldots$ in an excited state. The bands in a particular progression will always have the same shape, a fact which is useful in identification, moreover, matrix perturbations can be extremely helpful here. The departure of lineshape from the usual Lorentzian form is generally attributable to (1) the occupation of multiple sites in the matrix, and/or (2) the simultaneous excitation of lattice modes. These criteria apply if isolation is really occurring and dimers or large clusters are not also present in significant concentration. The trapped molecules can occupy positions in the lattice which are energetically similar (perhaps substitutional and interstitial sites, for example), in which case closely spaced multiple bands will appear, corresponding to a single band in the gas phase. Site splitting is typically a few cm^{-1} in magnitude and is sometimes difficult to resolve. In many cases site splitting can be reduced or even completely eliminated by the irreversible process of annealing the matrix. This is done by allowing the matrix to warm, followed by rapid quenching to the original low temperature. The term "annealing" is used in this context to imply relieving of strain, with perhaps some solid-state diffusion. Striking proof of the multiple site hypothesis has come from ESR spectra of atoms trapped in matrices. Of more significance is the fact that such spectra at 4°K provide a sensitive indication of the electronic properties of the molecule in its ground state.

(c) In most cases matrix studies yield no rotational structure, although the molecules H_2O, HCl, NH_3, and NH_2, for example, have been found to have interesting rotational motion in matrices.

(d) A further disadvantage is that incomplete isolation of the sample sometimes occurs.

Electron Spin Resonance Spectroscopy

ESR Studies of Matrix-Isolated Molecules

ESR studies of diatomic molecules containing a metal atom have not been made in the gas phase and it is unlikely that they will be in the near future since existing microwave techniques cannot accommodate studies of molecules that are stable with respect to the solid phase at temperatures in excess of 1000°K. The technique of matrix isolation was first applied to the study of the spectroscopic properties of high-temperature molecules in an IR investigation of B_2O_2 and B_2O_3 [25] and LiF [26]. Early ESR work using the matrix technique as applied to high-temperature molecules reported results for $Cu(NO_3)_2$ and CuF_2 [27], ScO, YO, and LaO [28], VO [3], AlO [29], and BC_2 [30]. Results have since been reported on ESR studies in matrices for BO [31], MgH, CaH, SrH, and BaH [32], ZnH, CdH, and HgH [33], BeH [34], BS [35], and RhC [36].

Transition-Metal Diatomic Oxides

The gaseous transition metal monoxides present intriguing problems in several related fields [37]. This group contains some of the most stable diatomic molecules known and their stability and open-shell electron configurations lead to the appearance of allowed electronic transitions in the visible region of the spectrum. Some of these are observed in the spectra of cool stars, as mentioned previously. The electronic states involved are often of high multiplicity. Consequently, analyses of the transitions present interesting challenges to conventional high-resolution spectroscopy, while the formulation of the energy levels of the states themselves pose theoretical problems. However, the lighter members ScO, TiO, and VO are simple enough to permit ab initio calculations of their electronic structures. Important results have recently come from studies of some of these diatomic oxides by matrix-isolation spectroscopy. The matrix method has supplemented information from gas-phase spectroscopy about nuclear hyperfine structure, which is important in the ground states of some of these molecules.

The Electron Spin Resonance Phenomenon

Since Zavoisky's first ESR experiment with $CoCl_2$ H_2O in 1944, the principles of ESR spectroscopy have been thoroughly studied and are discussed in detail in a number of excellent references [38-44]. The basic principles of the resonance phenomenon will be discussed here before detailed considerations of the application of ESR spectroscopy to the NbO molecule are considered in Chapter III.

Like all forms of spectroscopy, ESR monitors the net absorption of energy from a radiation field when molecular species change their energy state. The electromagnetic radiation field has associated with it orthogonal oscillating electric and magnetic fields. Most forms of spectroscopy utilize the interaction of the electric field component with molecular species. The energy required to promote an electron from its ground energy state to excited energy states is absorbed in the form of a radiation quantum with an energy hν, where h is Planck's constant (6.626196 x 10^{-27} erg-sec) and ν is the frequency of the radiation in units of hertz (Hz). Two conditions must be met for absorption to occur. First, the quantum (hν) of radiation must correspond exactly to the separation (ΔE) of energy levels between which a transition is to occur, that is,

$$h\nu = \Delta E . \qquad (1)$$

This relation is known as the resonance condition. Second, the oscillating electric (or magnetic) field component of the radiation must be able to stimulate an oscillating electric (or magnetic) dipole in the molecule. If this condition is met, the transition is said to be "allowed."

If a molecule contains a magnetic dipole, an interaction with the magnetic component of a radiation field is expected. Such absorptions are indeed observed but the presence of a static magnetic field is often required. The electrons and nuclei of a molecule both provide magnetic dipoles. ESR spectroscopy deals mainly with the electron magnetic dipoles and nuclear magnetic resonance (NMR) spectroscopy deals with the nuclear magnetic dipoles. A rigorous description of the electron spin resonance phenomenon must come from quantum theory, but useful analogies from classical physics may be drawn.

The magnetic dipole of an electron may be thought of as arising from the fact that the electron is a charged particle and that a moving charge created a magnetic field. The magnetic dipole may arise from the motion of the electron about the nucleus of an atom (called the orbital magnetic dipole) or from the spinning of the electron about an axis through its center (called the spin magnetic dipole). In most cases more than 99 percent of the total electron magnetic dipole is due to the latter effect. Magnetic dipoles may be characterized by a quantity called the magnetic dipole moment, $\bar{\mu}$, which is defined in terms of the interaction of a magnetic dipole with a magnetic field. This is a vector quantity, that is, has a direction as well as a magnitude, and all such quantities will be indicated in this work by a vertical bar over the symbol representing the magnitude of the vector quantity, hence, $\bar{\mu}$. The magnetic dipole moment in effect measures the strength of the magnetic dipole in a unit magnetic field.

Magnetic moments tend to be oriented by a magnetic field $\bar{H}$. Since work must be done to disorient a magnetic moment, it is obvious that there is a potential-energy difference between a condition of arbitrary orientation of $\bar{\mu}$ and $\bar{H}$ and one in which $\bar{\mu}$ and $\bar{H}$ are parallel (the state of minimum energy). The amount of work W required to disalign $\bar{\mu}$ from $\bar{H}$ is given quantitatively by

$$W = -\bar{\mu} \cdot \bar{H} \qquad (2)$$

Equation (2) can be rewritten as

$$W = -\mu_z H , \qquad (3)$$

when $\bar{\mu}$ and $\bar{H}$ are parallel. Here H is the magnitude of the magnetic field $\bar{H}$ and μ_z is the projection of $\bar{\mu}$ along the z-direction, which is arbitrarily taken as the direction of $\bar{H}$.

All electrons have an intrinsic spin characterized by a spin angular momentum $\bar{p}$. $\bar{p}$ and $\bar{\mu}$ are always proportional, that is,

$$\bar{\mu} = \gamma\bar{p} , \qquad (4)$$

where the proportionality constant γ is called the magnetogyric ratio. It is a unique result of the quantum theory that the component of $\bar{p}$ (and hence of $\bar{\mu}$) along a given direction can have only two values. Taken along the z-axis, the component p_z is given by

$$p_z = M_S h/2\pi , \qquad (5)$$

where $M_S = \pm 1/2$ and is called the spin quantum number. For classical motion,

$$\gamma = -e/2\ mc , \qquad (6)$$

where e is the charge on the electron (4.803250 x 10^{-10} esu), m is the mass of the electron (9.109558 x 10^{-28} g), and c is the speed of light (2.9979250 x 10^{10} cm/sec). Equations (4), (5), and (6) then lead to the relation

$$\mu_z = -(eh/4\pi mc)M_S \qquad (7)$$

Equation (7) applies to the classical motion of a charge about a stationary center. It also applies to the orbital motion of an electron around a nucleus. However, spin angular momentum is strictly a quantum mechanical effect and cannot be described accurately by classical analogs. For electron spin, Eq. (7) must be rewritten as

$$\mu_z = -g(eh/4\pi mc)M_S = -g\beta_e M_S , \qquad (8)$$

where β_e (= eh/4πmc = 9.274096 x 10^{21} erg/G) is called the Bohr magneton and g (= 2.002319278) is called the g-factor of the electron

The electron g-factor is one of the most accurately known of the physical constants [45] and it is remarkable that the theory of quantum electrodynamics is able to account for this factor within experimental error. The g-factor is a number that might be applied to any spinning object with a magnetic moment parallel to its axis of rotation [46]. The earth itself almost conforms to this description and if its north and south magnetic poles were not slightly disaligned with respect to its north and south geographic poles, it would conform exactly. If a spinning object with these properties is placed in an external magnetic field, it will precess, that is, its axis of rotation will slowly move around in a cone. The frequency of the precession depends on the product of two factors. (a) the strength of the external field and (b) the ratio of the object's magnetic moment to its angular momentum of rotation. Although the external magnetic field can be varied at will by the experimenter and adjusted to any desired strength, the ratio just mentioned is a property of the spinning object itself. This ratio has a unique value for the electron, and other kinds of particles have their own unique ratios. Since it is only the ratios for the various particles and not the separate values of the angular momentum and magnetic moment that are needed for interpreting numerous phenomena, the measurement of the ratios to a high degree of accuracy has been the object of intensive research [46]. The g-factor of a particle is the index of this ratio.

Substitution of Eq. (8) in Eq. (3) reveals that the energies E of electron-spin magnetic moments in a magnetic field are given by

$$E = g\beta_e H M_S = (\pm 1/2) g\beta_e H . \qquad (9)$$

This equation is often called the electron Zeeman energy. If a sample is subjected to electromagnetic radiation, it is found that at a certain magnetic field H_r absorption will occur. By applying the first condition for absorption, it is clear that at H_r the energy quantum hν must match that separation of electron energy levels, which from Eq. (5) is $g\beta_e H_r$. Thus the resonance condition is

$$h\nu = \Delta E = g\beta_e H_r \; . \tag{10}$$

H_r is called the resonance magnetic field. For a typical ESR experiment, hν corresponds to an energy of about 10^{-3} kcal/mole and it is unlikely that radiation in the microwave region can cause any direct chemical effects. The second condition for absorption is satisfied when the magnetic field component of the incident microwave radiation is polarized perpendicular to the direction of the static field, a condition easily met at microwave frequencies. Eq. (10) is satisfied over a wide range of frequencies and magnetic fields. For reasons of sensitivity, frequencies in the microwave region are used. Typically, for $\nu = 9.5$ GHz, $H_r = 3400$ G.

From Eq. (10) it is evident that there are two possible experimental approaches to the detection of resonant absorption. H can be held constant and ν varied or vice versa. The former case corresponds to fixing the spacing of the energy levels and adjusting hν to fit that spacing. This corresponds to the practice followed in most forms of spectroscopy since the energy levels are usually fixed by the molecular structure. The truly unique aspect of ESR (and NMR) spectroscopy is that the energy levels can be tuned by varying H to fit a fixed quantum of radiation. For experimental reasons this latter method is preferred and ESR spectra plot intensity versus magnetic field rather than frequency (or wavelength).

CHAPTER II

EXPERIMENTAL: THE NbO MOLECULE

Materials

Niobium metal powder (99.9+% pure) and niobium pentoxide (99.99+% pure) were obtained from Spex Industries, Inc. Enriched oxygen $^{18}O_2$ (93+% pure) was obtained from Miles Laboratories, Inc. The $^{16}O_2$ and the rare gases argon and neon were Airco research grade. Tungsten rod and tubing for sample cell fabrication were obtained from General Electric or Fansteel Metallurgical Corporation. All materials were used without further purification except for outgassing the sample and liquid-nitrogen trapping of the rare gases as described below.

Methods of Preparation of NbO

Diatomic niobium oxide molecules were prepared by the vaporization of an intimately mixed sample of Nb metal powder and finely powdered Nb_2O_5 (Nb:O molar ratio approximately 1:1) or by passing $^{16}O_2$ or $^{18}O_2$ over Nb metal powder contained in a tungsten Knudsen cell. In the former case the Nb/Nb_2O_5 mixture was contained in a resistance-heated tungsten cell or a thick-walled tungsten Knudsen cell inductively heated by a Lepel 5-kW unit. These methods of preparation are analogous to methods used to produce the other two Group VA diatomic oxides, VO and TaO, in similar matrix-isolation studies. Kasai [3] generated VO diatomic molecules by heating a mixture of vanadium metal powder and V_2O_5 (V:O molar ratio approximately 1:1) to about 1800°C in a tungsten cell. At this temperature VO is known to be the major species present in the vapor phase [47]. Weltner and McLeod [6] generated diatomic tantalum oxide molecules either by the vaporization of solid Ta_2O_5 or by passing $^{16}O_2$ or $^{18}O_2$ into a tantalum Knudsen cell at about 2000°C. It is known that at approximately 1950°C TaO and TaO_2 are present in roughly equal amounts in the equilibrium vapor over Ta_2O_5 [48].

Several studies [49-55] have shown that the reduction of Nb_2O_5 by Nb metal and the oxidation of Nb metal by O_2 gas yield predominantly NbO and NbO_2 as volatile oxides. In the present work the results of earlier mass spectrometric and thermodynamic studies [52] were useful in establishing the initial conditions for vaporization. The success of the methods used is demonstrated by the presence of strong ESR and optical signals clearly attributable to NbO with a cell surface temperature of 1900 to 2000°C. Also expected to be produced in at least equal amounts is NbO_2 [52]. Since solid Nb_2O_5 *in vacuo* at temperatures greater than about 900°C is subjected to thermal dissociation [51] according to the equation $Nb_2O_5(s) = 2NbO_2(g) + 1/2\ O_2(g)$ and since the vapor pressure of Nb metal at the operating temperatures is of the order of 10^{-7} torr [16,18,56], neither the pentoxide or Nb atoms is expected to be a contaminant in the sample matrix. The volatilization of NbO involves the processes [52]

$$NbO(s,l) \rightarrow NbO(g) ,$$

$$2NbO(s,l) \rightarrow NbO_2(g) + Nb(s) ,$$

and the volatilization of NbO_2 the processes [52]

$$NbO_2(s,l) \rightarrow NbO_2(g) ,$$

$$NbO_2(s,l) \rightarrow NbO(g) + O(g)$$

Cryogenic Apparatus

The cell and furnace arrangements, liquid-helium Dewars, and electron spin resonance apparatus used in the present matrix-isolation studies will be discussed in general terms with particular attention given to procedures devised for generation of NbO diatomic molecules. The liquid-helium Dewars were adapted from the design of Jen, Foner, Cochran, and Bowers [57] and the extensive work of Weltner and coworkers [6,20,25,27,58-61]. Three different types of Dewar arrangements were used with the furnace section, which is constructed to accommodate either inductive or resistive heating of the sample cells.

The design and dimensions of the thick-walled tungsten Knudsen cells used with inductive heating are shown in Figure 2. The cell is held at the center of the water-cooled, copper induction coil by three 1/16-inch tungsten rods. The particular design shown in Figure 2 was utilized for Nb/Nb_2O_5 sample mixtures. For passing O_2 gas over Nb metal powder the cell design in Figure 2 was modified by drilling a 0.125-inch hole through the center of the bottom of the cell. Small pieces of clean tungsten foil were also placed inside the cell to promote adequate circulation of O_2 gas over the Nb metal powder. The cell was connected to a 1-liter glass bulb of O_2 gas by means of a 1/8-inch O.D. tungsten tube which was tapered at one end to fit tightly into the hole through the bottom of the cell and was of sufficient length (approximately 3 inches) to extend beyond the induction coils to be attached to a length of 1/8-inch I.D. copper tubing. The copper tubing was connected to the O_2 bulb via an Edwards needle valve and suitable glass connectors.

The resistively heated cells were constructed from 1-inch lengths

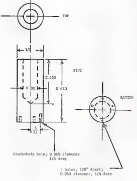

Figure 2 Schematic diagram of inductively heated tungsten Knudsen cell, dimensions given in inches, cap to cell is not shown but has a 1/16-inch diameter effusion hole

of 1/8-inch O.D. thin-walled tungsten tubing with an effusion hole (1/16-inch diameter) centered on the length of the tube. End plugs for these cells were constructed from 1/8-inch solid tungsten rod and were 1/8-inch in total length with one half of this length machined to fit securely into one end of a particular individual cell. The complete resistance cell, end plugs included, was attached to the water-cooled, copper electrodes of the furnace flange by two tungsten straps which were securely attached to the electrodes with tungsten screws. Resistance cells were used exclusively with Nb/Nb_2O_5 mixtures after attempts with a design modified to permit passage of O_2 gas over Nb metal powder showed that at the necessary experimental temperature range of 1900 to 2000°C the thin-walled tungsten cells readily ruptured, presumably due to reaction with O_2 and/or the sample. Consequently, all experiments flowing O_2 gas over hot Nb metal powder were done using inductive heating and thick-walled tungsten Knudsen cells.

The basic features of the liquid-helium Dewar used for ESR studies are shown in Figure 3 along with a furnace arrangement utilizing resistive heating. In the figure the sample cell is shown in a vertical position, however, in most experiments the cell was maintained in a horizontal position because this yielded better results. Figure 4 shows the optical Dewar assembly with the furnace arrangement for inductive heating. The optical Dewar arrangement most frequently used, however, was a variable-temperature, liquid-helium Dewar, essential features of which are shown in Figure 5.

The flat trapping surface in the ESR Dewar arrangement is a single crystal sapphire rod (length 1 1/4 inches, width 1/8 inch thickness 3/64 inch), flat on both sides, with one end embedded securely into the inner

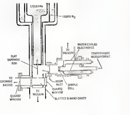

Figure [illegible]: Basic design features of liquid helium Dewar used for ESR studies; furnace arrangement for resistive heating only

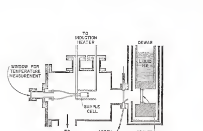

Figure 4. Basic design features of liquid-helium Dewar used for optical studies, furnace arrangement for inductive heating only

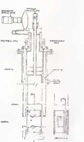

Figure 5 Basic design features of variable-temperature liquid helium Dewar used for optical studies; furnace arrangement on [illegible]

liquid-helium Dewar which is cooled to 4°K (see Figure 3). No accurate temperature measurements were made on the rod itself, but single-crystal sapphire has a very high thermal conductivity and is expected to thermally equilibrate quite rapidly with the liquid-helium Dewar. The versatility of this experimental arrangement arises from the fact that the sapphire rod can be lowered or raised and rotated about its vertical axis by any angle either inside or outside the resonance cavity by a vacuum-tight bellows assembly located at the top of the Dewar. The cavity is designed to permit simultaneous spin resonance and photolysis experiments but this capability was not utilized in the present work. As shown in Figure 3, when the rod is outside the cavity, it is in line with the rare gas inlet nozzle and can be rotated so that the rare gas and molecular beam of high-temperature molecules originating in the furnace section are simultaneously deposited on the flat surface of the sapphire rod. The sample cell was about 5 inches from the rod surface. The Dewar arrangement and furnace assembly are connected by a double gate-valve system to permit the furnace assembly to be removed from the Dewar without breaking the vacuum. The Dewar itself hangs from fixed rails above the spectrometer magnet and the entire Dewar arrangement is rolled between the pole faces of the magnet until the ESR resonance cavity is properly positioned. The sapphire rod is then lowered into the cavity and a short length of waveguide, projecting from the Dewar and partitioned from the cavity by a mica window preserving the high vacuum in the cavity, is connected to the spectrometer microwave bridge. The spin resonance spectrum can then be measured with the sapphire rod turned in any direction relative to the magnetic field. Quartz windows are mounted in the sides of the Dewar at the level of the flange connected to the furnace. This provides openings so that light can be passed through the flat surfaces of the sapphire rod to measure the optical absorption spectrum of the same matrix investigated by ESR. These windows also conveniently allow viewing of the rod during and after deposition of the matrix. This arrangement of Dewar and furnace makes it possible to trap molecules vaporized from solids at temperatures up to 2500°K.

Independent pumping of the Dewar and furnace by mechanical and 2-inch silicone-oil diffusion pumps allows rapid downward pumping and gives ultimate background pressures with liquid nitrogen and helium in the Dewar and liquid nitrogen in the furnace trap of approximately 7×10^{-8} torr in the Dewar and 7×10^{-6} torr in the furnace with the connecting gate valve closed. The furnace background pressure drops to roughly 1×10^{-7} torr when the gate valve is opened. Similar independent pumping of the Dewar and furnace arrangements is used for the optical Dewar systems and comparable background pressures are obtained there also.

The furnace and Dewar arrangement of Figure 4 is a convenient one for optical studies. There are two important design features incorporated into this arrangement. First, the deposition window can be rotated 90° about a vertical axis. A matrix can be applied through one of three ports and then by turning the window through 90° into the optical beam a spectrum of the matrix can be taken. Of course, this does not allow simultaneous matrix deposition and spectral measurement. The second important feature is that the deposition window is surrounded on all four edges by the copper block, which is in turn in contact with the liquid-helium cryogenate on four sides. This system makes for efficient heat removal from the window, which is absolutely essential when working with high-temperature species and particularly with neon as a matrix gas. The optical studies in the present work utilized a cesium iodide window in this system both for deposition and port windows. Cesium iodide is very well suited to these studies, particularly since it is transparent in the desired infrared range of 1 to 50 μm as well as in the 200 to 800 nm visible range [62,63].

Most of the work done on an optical Dewar system used the more versatile variable-temperature Dewar arrangement (see Figure 5). The only change from the previously discussed optical Dewar arrangement is that a new type of liquid-helium Dewar is used. A reservoir of liquid helium is connected to a copper block (containing the CsI window to be cooled to 4°K) by 1/8-inch stainless-steel tubing. The helium flows through channels in the copper block and then to an outlet containing a Hoke micrometer needle valve. The reservoir is pressurized at 2.5 psi so that liquid helium is forced over into the copper block at a rate determined by the needle valve setting. A Chromel versus Au-0.02 at.-percent Fe thermocouple in conjunction with a Leeds and Northrup volt potentiometer was used for temperature measurements on the CsI window.

Spectrometer instrumentation

ESR spectra were recorded on a Moseley model 2D-2 X-Y recorder with the Varian V-4500 instrument employing superheterodyne detection. The magnetic field was measured with an accuracy of ±0.5 G by using an Alpha Scientific model 675 NMR fluxmeter whose frequency was determined with a Beckman 6121 counter. The X-band ($\nu \cong 9.4$ GHz) microwave cavity frequency was determined with a Hewlett-Packard high-Q wavemeter.

Optical spectra were recorded over the range 300 to 800 nm on a Jarrell-Ash 0.5 m Ebert scanning spectrometer with a grating blazed at 500 nm and equipped with an RCA 931A photomultiplier tube. Relative band positions are generally measurable to ±0.5 nm although absolute positions as determined by Hg arc lines are considered accurate to about ±0.1 nm. A General Electric tungsten lamp provided the continuum light source

Infrared spectra were recorded over the range 4000 to 200 cm^{-1} on a Perkin-Elmer 621 grating infrared spectrometer with an accuracy of ±1 cm^{-1}.

Cell temperatures were measured with a Leeds and Northrup vanishing-filament optical pyrometer through an O-ring sealed glass viewing port (see Figures 3 and 4) equipped with a magnetic shutter to prevent vaporization products from forming a film on the glass. The pyrometer was sighted into a black-body hole (see Figure 2) in the bottom of the tungsten Knudsen cell and on the center portion of the resistively heated cells.

Experimental Procedures

The following procedures were typically used prior to and during each experiment. The sample cell, heated either resistively or inductively, was outgassed in the furnace chamber in vacuo at a temperature of 2200 to 2300°C for several hours. The cell was then allowed to cool to room temperature, was removed from the furnace, and filled with sample material, either Nb metal powder or a previously prepared mixture of Nb and Nb_2O_5. The cell was replaced in the furnace and the sample outgassed in vacuo at a temperature of about 1000°C for an hour. The cell was again cooled to room temperature and the system allowed to pump down overnight before running an experiment. At the start of an experiment the cell was slowly brought up to about 1400°C while the Dewar was being prepared.

The liquid-helium Dewar was precooled with liquid nitrogen by filling through the top. The pressure release valve was then replaced and the window temperature of the optical Dewar reached about 80°K in a 10 to 15 minute period. The liquid nitrogen was forced out, the system thoroughly and quickly flushed with dry nitrogen and then helium gases, and liquid helium admitted. It was found to be particularly important to thoroughly flush all liquid nitrogen from the variable-temperature system to prevent blockage in the helium flow to the copper block due to liquid nitrogen freezing in the tubing. Occasional rough pumping on the micrometer outlet line was necessary to circumvent the vapor lock which would prevent the liquid helium from flowing over into the copper block. It was usually the case that once helium flow through the copper block was well established it remained so for the duration of the experiment. This was particularly important after matrix deposition since it was necessary that the window then be maintained near 4°K.

When using the ESR Dewar, a preliminary cooling of the inner helium Dewar with liquid nitrogen as described above was also always carried out. When using the sapphire rod, the rare gas was deposited on both sides of the rod for about 5 minutes before opening the gate valve connecting the furnace to prevent sample from being deposited directly on the rod surface. The sample matrix was also coated with rare gas by a 5-minute deposition after the matrix was formed. Every 5 minutes during the run the rod was rotated by 180° so that it would be coated on both sides. In the optical Dewar only one side of the window is coated, but rare gas was deposited for about 5 minutes both before and after matrix formation as just described. The sample was deposited simultaneously with the rare gas on either the flat sapphire rod for ESR studies or the CsI window for optical studies. The rare gas flow rate was maintained at approximately 0.5 l-atm/hr and the rare gas was precooled with a liquid nitrogen bath immediately before entering the Dewar. The trapping temperature was always near 4°K. Typical deposition times were 50 minutes on the sapphire rod and 30 minutes on the CsI window. Typical Dewar pressures during deposition were about 4 x 10^{-6} torr and typical furnace pressures about

1×10^{-4} torr. The matrix was usually pale green, particularly on the sapphire rod, for those runs in which spectral evidence clearly indicated the presence of NbO in the matrix. The furnace assembly was usually opened to the Dewar only after it could be clearly seen through the side viewing port of the furnace housing that a film or "mirror" was being deposited on the front wall of the furnace. Formation of such a "mirror" invariably proved to be a reliable indication that sample effusion from the cell was satisfactory for matrix deposition. The gate valve connecting the furnace and Dewar was always closed immediately after deposition of the matrix and the cell temperature lowered to about 1400°C until spectral results indicated that sample concentration in the matrix was sufficient without further deposition, at which time the cell was allowed to cool to room temperature.

To raise the window temperature in the variable-temperature Dewar to about 10°K, the micrometer was carefully and slowly closed manually and the rise in temperature followed closely with the thermocouple and by noting the rise in pressure in the Dewar (usually up to the 10^{-4} scale of the ion gauge). The matrices were typically warmed for periods of 5 to 10 minutes and then quenched again to 4°K by opening the needle valve. The optical spectrum was then checked for any changes due to this annealing process.

Experimental Problems

Several experimental problems were encountered in the course of the experimental work in addition to those already mentioned for $Nb(s) + O_2(g)$ experiments with resistive heating. Resistance heating of Nb/Nb_2O_5 mixtures invariably gave good results and no experimental difficulties were experienced. Inductive heating of Nb/Nb_2O_5 mixtures was generally satisfactory, although occasional arcing between the cell and the induction coils was experienced. The best results were always obtained in inductive heating experiments when the contacts of all parts of the inductive heating assembly were scrupulously cleaned with abrasive paper and then washed with alcohol or acetone, the connections also needed to be as tight as possible to give good heating. Inductive heating with $Nb(s) + O_2(g)$ experiments presented several unexpected problems

It was found that the rate of flow of O_2 gas was very important, not only insofar as the amount of NbO formed and deposited in the matrix was concerned, but also because if the flow rate was too high, the sample material was forced to the front of the cell, blocking the effusion hole. The effusion hole was also occasionally blocked by apparent sintering of the sample material even when some diatomic molecules were initially trapped in the matrix. Several runs also yielded inadequate results due to sample material flowing back into the tungsten tube leading to the O_2 bulb, thereby blocking further flow of O_2 gas. After one costly failure with enriched oxygen $^{18}O_2$ a series of "blank" runs was made in which air rather than pure O_2 was allowed into the system. The experience gained here made possible excellent results with future runs. A needle valve setting of 1.88 with a power setting of 60 giving a grid current of 108 mA on the Lepel 5-kW high-frequency induction heater gave a furnace pressure of 2×10^{-5} torr and a Dewar pressure of 2×10^{-6} torr during deposition. Excellent visible and IR spectra were obtained

Other than routine leakage problems in the vacuum system occasionally arising, no other major difficulties were encountered. The sample material left in the Knudsen cell after an $Nb(s) + O_2(g)$ run could be used again as it was found that enough $NbO(s)$ was left in the cell to deposit another matrix at a later date. This was also true with samples left from Nb/Nb_2O_5 experiments. An alternative approach to the Nb(s) + O_2(g) experiments described here would have been to construct Knudsen cells from Nb metal rod or to use coils of Nb wire in the tungsten cells. However, both Nb metal rod and wire are rather expensive.

CHAPTER III

THE ESR SPECTRUM OF THE NbO MOLECULE

Introduction

The fundamental relationship between the frequency ν of the oscillating magnetic field of the applied microwave radiation and the external field H at which resonant absorption occurs is given by Eq. (11),

$$h\nu = g\beta_e H \tag{11}$$

Here, as in Chapter I, h is Planck's constant, β_e is the Bohr magneton, and g is the electron g-factor. In the real world of ESR spectroscopy the unpaired electron seldom enjoys the simple situation indicated by Eq. (11). If Eq. (11) is used merely to describe the field at which resonant absorption occurs for a given energy input, $h\nu$, it is found, for example, that (a) in numerous cases g varies with H and the simple linear relationship between ν and H in Eq. (11) is approximated only at high fields, (b) for crystalline samples the resonant value of H is a function of the angle between the crystalline axes and the applied field so that g is anisotropic, that is, orientation dependent, (c) the numerical value of g and the amount of anisotropy for a given paramagnetic sample vary with the structure of the crystal in which they are examined, (d) in comparing the observed g-values of many paramagnetic ions with the free-ion value there appears to be no simple correlation, and (e) where more than one unpaired electron is present in the paramagnetic sample, several absorption peaks with different g-factors may be observed (or none at all). These considerations clearly imply that the effect of the local environment on g-factors is quite significant, and, consequently, that the energy of the states between which transitions take place is being altered. It therefore becomes necessary to consider how these energy levels are influenced when paramagnetic species are placed in a chemical environment.

An electron spin resonance spectrum is generally a rather complex affair, with lines due to different electronic transitions which may be further divided into additional groups of lines by interaction with a nuclear magnetic moment. The data are usually rendered meaningful by resorting to the theories of quantum mechanics and thereby describing the particular paramagnetic system of interest by means of a spin Hamiltonian operator, $(H_{spin})_{op}$. The spin Hamiltonian has been described [64] as a convenient resting place during the long trek from the fundamental theory of spin resonance to the experimental lines observed with the spectrometer. The spin Hamiltonian was devised initially by Abragam and Pryce [65] in 1951 and is a particular part of the overall Hamiltonian operator, $(H_{total})_{op}$. It is by far the most useful mathematical tool available to the ESR spectroscopist. The theory of the spin Hamiltonian has been treated in exhaustive detail in a large number of excellent texts on the subject [38-44,66-80]. It is beyond the scope of the present work to treat the subject thoroughly, but a brief consideration of the general case and the specific form of the general case applicable to the present studies will be given as an introduction to the detailed consideration of the NbO ESR spectrum.

Since measurement of the ESR spectrum observed under varying conditions of frequency and orientation results in the accumulation of a mass of data, which is not particularly useful unless some simple interpretation can be found, the state of affairs has been expressed conventionally from quantum mechanical considerations in terms of the previously mentioned Hamiltonian, which is an operator that operates upon a wavefunction. When applied to the wavefunction describing a particular system, the Hamiltonian generates the permitted energy levels of that system. While the general Hamiltonian of a system contains many terms and is thoroughly complex, the spin Hamiltonian useful for the purposes of ESR investigations will contain relatively few terms. The advantage of the spin Hamiltonian is that a complete description of the experimental data can be presented by giving the size of the coefficients of these terms, together with the directions of the appropriate axes relative to the symmetry axes of the paramagnetic sample when anisotropy is present

The General Hamiltonian

The complete Hamiltonian of a free paramagnetic entity represents the total energy of the system and may be considered as the sum of all energy contributions. The relative magnitudes of these energy contributions extend over roughly nine orders of magnitude. Clearly, some contributions are more important than others, moreover, only a selected few need be considered explicitly in ESR studies. Representing the complete Hamiltonian operator as in Eq. (12),

$$(H_{total})_{op} = \sum_{i} (H_i)_{op} , \qquad (12)$$

the nature and importance of the individual contributions, $(H_i)_{op}$, will be briefly considered.

$(H_1)_{op}$, given by Eq. (13), is a composite term expressing the total kinetic energy of the electrons, the Coulombic attraction between electrons and nuclei, and the electron-electron repulsion,

$$(H_1)_{op} = \sum_i \{(\bar{p}_i^2/2m) - (Ze^2/\bar{r}_i)\} + \sum_{ij} e^2/\bar{r}_{ij} \quad (13)$$

Here $\bar{p}_i$ is the momentum of the i^{th} electron, $\bar{r}_i$ is its distance from the nucleus, Z is the nuclear charge, and $\bar{r}_{ij}$ is the distance between the i^{th} and j^{th} electrons. The terms are summed over all electrons and yield the unperturbed electronic levels before interaction between spin angular momentum and orbital angular momentum is considered. Separations are of the order of 10^5 cm^{-1} ($\approx 10^{-11}$ erg $\approx 10^2$ kcal/mole) and it is most unusual to have to consider any level other than the lowest. Although usually by far the most dominant term in the overall Hamiltonian, $(H_1)_{op}$ is spin-independent and plays no part in the spin Hamiltonian.

$(H_2)_{op}$ represents that part of the potential energy arising from the electrostatic field of neighboring atoms. This interaction is generally called the crystal (or ligand) field and is given by

$$(H_2)_{op} = \sum_i e_i V(r_i) \ , \quad (14)$$

where $V(r_i)$ is the electrostatic potential at the paramagnetic entity with which each electron interacts. This term plays a major role in the study of single crystals, particularly those of the transition metal group, and usually has a magnitude on the order of 10^4 cm^{-1} ($\approx 10^{-12}$ erg ≈ 10 kcal/mole).

$(H_3)_{op}$ is given by

$$(H_3)_{op} = \sum_{ij} \lambda_{ij} \bar{l}_i \cdot \bar{s}_j \ , \quad (15)$$

where $\bar{l}$ and $\bar{s}$ are the orbital and spin angular momenta of the individual electrons. This is the spin-orbit coupling interaction and the appropriate spin-orbit coupling constant, λ_{ij}, is an energy term which may assume either positive or negative values. If only terms derived from the ground state defined by Eq. (13) are considered, Eq. (15) can be replaced by the simpler form of Eq. (16),

$$(H_3)_{op} = \lambda\bar{L} \cdot \bar{S} \;, \qquad (16)$$

where $\bar{L}$ and $\bar{S}$ are the free-spin values. The magnitude of the spin-orbit interaction is usually $10^2 - 10^3$ cm^{-1} ($\cong 10^{-14} - 10^{-13}$ erg $\cong 10^{-1} - 1$ kcal/mole).

$(H_4)_{op}$ is the term largely responsible for paramagnetism. This is called the electronic Zeeman term and represents the interaction of the angular moments of the electrons with the external magnetic field. The interaction is usually represented by Eq. (17),

$$(H_4)_{op} = \sum_i \beta_e(\bar{l}_i + g_e\bar{s}_i) \cdot \bar{H} \;, \qquad (17)$$

where β_e is the Bohr magneton, g_e is the electron free-spin g-factor, and $\bar{H}$ is the magnetic field vector. This can be written as $\beta_e(\bar{L} + g_e\bar{S}) \cdot \bar{H}$ using the same criterion as in Eq. (16). The energy of this interaction is usually 0 - 1 cm^{-1} ($\cong 10^{-16}$ erg $\cong 10^{-3}$ kcal/mole). In the absence of spin-orbit interaction, the average value of $\bar{L}$, denoted by $\langle\bar{L}\rangle$, is zero and then $(H_4)_{op} = g_e\beta_e\bar{S} \cdot \bar{H}$.

$(H_5)_{op}$ represents the electronic spin-spin interaction energy, which usually has a magnitude of 0 - 1 cm^{-1} ($\cong 10^{-16}$ erg $\cong 10^{-3}$ kcal/mole):

$$(H_5)_{op} = \sum_{ij} [(\bar{s}_i \cdot \bar{s}_j/r_{ij}^3) - 3(\bar{r}_{ij} \cdot \bar{s}_i)$$
$$\times (\bar{r}_{ij} \cdot s_j)/r_{ij}^5] \qquad (18)$$

This interaction may or may not be small (or large) enough to be ignored in considering the spin resonance spectrum.

$(H_6)_{op}$ describes the interaction between the electron angular momenta and the nuclear spin. It may be written as

$$(H_6)_{op} = \sum_i a_i \bar{J}_i \cdot \bar{I}_i \ , \qquad (19)$$

in the general instance, where $\bar{J}_i$ is the total (spin plus orbital) angular momentum of the i^{th} electron, $\bar{I}_i$ is the nuclear spin, and the a_i are the nuclear hyperfine coupling constants. The magnitude of the interaction is of the order $10^{-2} - 10^{-4}$ cm^{-1} ($\cong 10^{-18} - 10^{-20}$ erg $\cong 10^{-5} - 10^{-7}$ kcal/mole). The nuclear hyperfine interaction is invariably treated as the sum of an anisotropic part and an isotropic part in the spin Hamiltonian as given in Eqs. (20):

$$(H_6^{aniso})_{op} = g_e\beta_e g_N\beta_N\{(\bar{I}\cdot\bar{S}/r^3) - 3(\bar{S}\cdot\bar{r})(\bar{I}\cdot\bar{r})/r^5\} \ , \qquad (20a)$$

$$(H_6^{iso})_{op} = (8\pi/3) g_e\beta_e g_N\beta_N|\psi_N(0)|^2 \ . \qquad (20b)$$

Here g_e and g_N are the electronic and nuclear g-factors, respectively, β_e and β_N ($= 5.050951 \times 10^{-24}$ erg/G) are the electronic and nuclear magnetic moments, respectively, r is the distance between electron and nucleus, $|\psi_N(0)|^2$ is the unpaired spin density at nucleus N, and the same criterion is applied as in Eq. (16). These interactions will be treated in extensive detail in the case of the NbO molecule in a subsequent section.

$(H_7)_{op}$ is called the nuclear Zeeman term and represents the interaction between the nuclear spin and the external field

$$(H_7)_{op} = -\sum_i g_N\beta_N\bar{I}_i \cdot \bar{H} \qquad (21)$$

The interaction ranges over the magnitude $10^{-1} - 10^{-4}$ cm^{-1} ($\cong 10^{-17} - 10^{-20}$ erg $\cong 10^{-4} - 10^{-7}$ kcal/mole) and for ESR spectroscopy can usually be neglected except in considering second-order effects in the nuclear hyperfine interaction. Of course, in NMR spectroscopy, this Zeeman term assumes a dominant role in the resonance phenomenon and is extremely important.

$(H_8)_{op}$ represents nuclear electric quadrupole interactions and is of the order $10^{-2} - 10^{-4}$ cm^{-1} ($\simeq 10^{-18} - 10^{-20}$ erg $\simeq 10^{-5} - 10^{-7}$ kcal/mole)

$$(H_8)_{op} = \{e^2\bar{Q}/2I(I + 1)\} \sum_i \{l(l + 1)/r_i^3$$

$$- 3(\bar{r}_i \cdot \bar{I})^2/r_i^5\} \qquad (22)$$

Here $\bar{Q}$ is the electric quadrupole moment of the nucleus, $\bar{I}$ is the nuclear spin, and again the criterion of Eq (16) applies.

The Spin Hamiltonian

General Case

Of the various terms in the general Hamiltonian, $(H_1)_{op}$, $(H_2)_{op}$, and $(H_3)_{op}$ involve too much energy for excitation by ESR. However, $(H_4)_{op}$, $(H_5)_{op}$, and $(H_6)_{op}$ involve energies ideally suited to existing microwave practice and are consequently the main concern of ESR spectroscopy. $(H_7)_{op}$ and $(H_8)_{op}$ are frequently too small to be observed in the presence of the electronic Zeeman term, $(H_4)_{op}$, although they are important in second-order effects in the nuclear hyperfine interaction.

The lowest group of energy levels, that is, the ones between which microwave transitions are induced, depends in a complicated way on the particular ion (if the transition group is being considered), the symmetry and strength of the crystalline field, the spin-orbit coupling, and other effects such as the hyperfine interaction between electrons and nucleus. However, these energy levels, and the experimental spin resonance data obtained from them, can be described by the use of a spin Hamiltonian in a fairly simple way that requires no detailed knowledge of the above effects. Calculations with the total Hamiltonian are very difficult and so a simplified accounting of the more likely interactions is performed with a spin Hamiltonian. Thus, as mentioned previously, the spin Hamiltonian is utilized for a shorthand description of the experimental results in that such parameters as the g-factor, zero-field splittings arising from spin-spin interactions, and nuclear hyperfine constants are determined experimentally and then fitted to models with the aid of the spin Hamiltonian. As a result, reporting the parameters in a standard form simplifies communication and aids the search for suitable models.

The ground state of a paramagnetic entity frequently consists of a group of electronic levels whose separation is a few cm^{-1} or less, while all the other electronic levels lie considerably higher. The behavior of this group can be represented by defining an "effective" spin S such that the total number of levels in the group is 2S + 1, the same as in an ordinary spin multiplet. It is further required that the matrix elements between the various states determined by the full Hamiltonian that describes the system be proportional to those of the effective spin. It is then possible to describe the behavior of this group of levels by a spin Hamiltonian involving just the effective spin, and where hyperfine interactions are present, the nuclear spins. In other words, by convention, S in the spin Hamiltonian is assigned a value that makes the observed number of energy levels equal to 2S + 1. Since in spin systems where only the lower energy levels are inhabited, the higher levels will not be detected experimentally, the value of S determined from the 2S + 1 observed levels corresponds to a fictitious state. As a result, g may vary considerably from the Lande g-factor [72,73] given by Eq. (23),

$$g = 1 + [J(J+1) + S(S+1) - L(L+1)]/2J(J+1) \qquad (23)$$

The Lande g-factor, of course, gives the splitting between multiplet levels in the case of Russell-Saunders coupling and was originally deduced by Landé in the study of atomic spectra.

Abragam and Pryce [65] have shown that the behavior of a spin system can be described by a spin Hamiltonian, and that the splitting, which may be calculated by first- and second-order perturbation theory, is precisely the same as if the orbital angular momentum is ignored and its effect replaced by an anisotropic coupling between the electron spin and the external magnetic field. In other words, the effect of an external magnetic field on the energy levels of paramagnetic species, after taking into account the crystal field and spin-orbit coupling, can be expressed in terms of g-factors which have the same symmetry as the combined crystal field and Jahn-Teller distortion. The Jahn-Teller theorem states that any nonlinear molecule with an orbitally degenerate ground state is unstable and tends to distort in order to remove this degeneracy. If after Jahn-Teller distortion the system assumes axial symmetry, values of $g_{||}$ and $g_{\perp}$ are found which correspond to application of the magnetic field parallel and perpendicular to the axis of distortion, respectively. If no such symmetry exists, the g-factor must be expressed in terms of $g_{xx} \neq g_{yy} \neq g_{zz}$, corresponding to three mutually perpendicular directions of the external field. This means that the terms $(H_1)_{op}$, $(H_2)_{op}$, $(H_3)_{op}$, and $(H_4)_{op}$ can be replaced by a single term $\beta_e \bar{H} \cdot \bar{g} \cdot \bar{S}$, where for an arbitrary set (x,y,z) of orthogonal axes,

$$\beta_e \bar{H} \cdot \bar{g} \cdot \bar{S} = \beta_e [S_x S_y S_z] \begin{bmatrix} g_{xx} & g_{xy} & g_{xz} \\ g_{yx} & g_{yy} & g_{yz} \\ g_{zx} & g_{zy} & g_{zz} \end{bmatrix} \begin{bmatrix} H_x \\ H_y \\ H_z \end{bmatrix} \tag{24}$$

S_x, S_y, and S_z are components of the effective spin along the x, y, and z axes. In Eq. (24) $\bar{g}$ is strictly a 3 x 3 matrix and is often referred to as a symmetrical tensor of the second order. It should be noted, however, that although from an operational point of view $\bar{g}$ is commonly referred to as a "tensor," it is not strictly a tensor mathematically. $\bar{g}^2$, however, is true tensor. Equation (24) expresses the fact that the complete interaction of $\bar{S}$ and $\bar{H}$ must take into account the effect of each component of $\bar{S}$ on each component of $\bar{H}$. The double subscripts on the g-tensor may be interpreted as follows. For example, the g-component, g_{xy}, may be considered as the contribution to g along the x-axis when the magnetic field is applied along the y-axis. In general, the off-diagonal elements of the g-tensor are very small and may be neglected. Thus, another way of looking at this form of representation is to say that the field of the orbital angular momentum is replaced by an anisotropic coupling between the spin and the magnetic field. This implies that it is easier to make the spin reverse its direction when the field is applied in some directions rather than in others. The great convenience of this way of expressing the combined interactions is that the magnetic properties of the system can now be related to this "effective" spin by means of Eq. (24), which is a spin Hamiltonian.

The most general form of the spin Hamiltonian contains a large number of terms, representing the Zeeman interaction of the magnetic electrons with the external field, level splittings due to indirect effects of the crystal field, hyperfine structure due to the presence of nuclear magnetic dipole and electric quadrupole moments, and the Zeeman interaction of the nuclear moment with the external field. Thus, in terms of the notation of Eq. (24), a general spin Hamiltonian can be written as in Eq. (25),

$$(H_{spin})_{op} = \beta_e \bar{H} \cdot \bar{g} \cdot \bar{S} + \bar{S} \cdot \bar{D} \cdot \bar{S} + \bar{S} \cdot \bar{A} \cdot \bar{I} + \bar{I} \cdot Q \cdot \bar{I} - \beta_N \bar{H} \cdot g_N \cdot \bar{I} \qquad (25)$$

Here $\tilde{g}$ is the g-tensor, $\tilde{D}$ is the fine structure tensor associated with spin-spin interactions, $\tilde{A}$ is the nuclear hyperfine tensor, $\tilde{Q}$ is the quadrupole tensor, and g_N is the nuclear g-tensor.

Axial Symmetry Case

For the case of axial symmetry, Eq (25) reduces to

$$\begin{aligned}(H_{spin})_{op} = {} & g_{||}\beta_e H_z S_z + g_{\perp}\beta_e(H_x S_x + H_y S_y) \\ & + A_{||} I_z S_z + A_{\perp}(I_x S_x + I_y S_y) \\ & + D[S_z^2 - (1/3)S(S + 1)] \\ & + Q'[I_z^2 - (1/3)I(I + 1)] - g_N \beta_N \bar{H} \cdot \bar{I} \ , \qquad (26)\end{aligned}$$

where the z-axis is to be identified with the symmetry axis. Equation (26) is thus the form of the spin Hamiltonian applicable to the case of the axially symmetric NbO molecule. Considering nuclear electric quadrupole and nuclear Zeeman interactions to be negligible for the present time, Eq. (26) may be rewritten as

$$\begin{aligned}(H_{spin})_{op} = {} & g_{||}\beta_e H_z S_z + g_{\perp}\beta_e(H_x S_x + H_y S_y) \\ & + A_{||} I_z S_z + A_{\perp}(I_x S_x + I_y S_y) \\ & + D[S_z^2 - (1/3)I(I + 1)] \qquad (27)\end{aligned}$$

Angular Variation of the ESR Spectrum

In general then the g factor of an axially symmetric linear molecule will have two extreme values, $g_{||}$ and $g_{\perp}$, depending upon whether the applied magnetic field is parallel or perpendicular to the axis of the molecule. For angles θ between the parallel ($\theta = 0°$) and perpendicular

($\theta = 90°$) orientation g is given by

$$g^2 = g_{||}^2\cos^2\theta + g_{\perp}^2\sin^2\theta \; . \qquad (28)$$

If all the molecules were lined up, as for example in a single crystal, resonance would be observed (ignoring any hyperfine interactions) first at a magnetic field $H_{||} = h\nu/g_{||}\beta_e$ and then finally at $H_{\perp} = h\nu/g_{\perp}\beta_e$ as θ varied from 0° to 90° for a fixed spectrometer operating frequency ν. On the other hand, if the molecule is rapidly and freely rotating, the anisotropy in the g-factor is averaged out and one line will be observed at a magnetic field $H_{iso} = h\nu/g_{iso}\beta_e$, where

$$g_{iso} = (g_{||} + 2g_{\perp})/3 \qquad (29)$$

What sort of spectrum will be observed if the molecules are randomly oriented but rigidly held, as in a solid matrix? The spectrum is expected to be independent of the angle that the magnetic field makes with the solid sample. The problem was first treated by Bleaney [81,82] and Sands [83] and later by many others [27,84-95].

For N' molecules randomly oriented with respect to the direction of the applied magnetic field, the number of molecules dN within the angle increment dθ is

$$dN = (N'/2)\sin\theta d\theta \; , \qquad (30)$$

where θ is the angle measured from the magnetic field direction. In the ESR spectrum the absorption intensity as a function of θ is proportional to the number of molecules dN lying between θ and θ + dθ (assuming the transition probability is orientation independent). The g-factor varies with θ as in Eq. (28) and so, for a fixed spectrometer frequency ν, the resonant magnetic field is given by

$$H = (h\nu/\beta_e)(g_{||}^2\cos^2\theta + g_{\perp}^2\sin^2\theta)^{-1/2} \qquad (31)$$

From Eq. (31) it is seen that

$$\sin^2\theta = (g_{iso}^2H_{iso}^2/H^2 - g_{||}^2)/(g_{\perp}^2 - g_{||}^2) \; . \qquad (32)$$

From Eq. (32) it is found that

$$\sin\theta d\theta = -(g_{iso}^2H_{iso}^2/H^3)\{(g_{||}^2 - g_{\perp}^2)(g_{iso}H_{iso}/H)^2 - g_{\perp}^2\}^{-1/2}dH \; . \qquad (33)$$

The intensity of absorption in a range of magnetic field dH is proportional to

$$|dN/dH| = |dN/d\theta||d\theta/dH| \; . \qquad (34)$$

Equation (30) defines $dN/d\theta$ and $d\theta/dH$ is obtained from Eq (33). According to Eq. (31) and the fact that $H_{iso} = h\nu/g_{iso}\beta_e$,

$$H_{||} = h\nu/g_{||}\beta_e = g_{iso}H_{iso}/g_{||} \; , \qquad (35a)$$

$$H_{\perp} = h\nu/g_{\perp}\beta_e = g_{iso}H_{iso}/g_{\perp} \qquad (35b)$$

At these two extremes the intensity of absorption varies as follows

$$|dN/dH| = H'g_{||}^3/2g_{iso}H_{iso}(g_{||}^2 - g_{\perp}^2) \quad \text{for } \theta=0° \qquad (36a)$$

$$|dN/dH| = \infty \quad \text{for } \theta=90° \; . \qquad (36b)$$

When plotted versus increasing magnetic field, this absorption has the shape shown in Figure 6a for the case of $g_{||} > g_{\perp}$ and taking into consideration the inherent linewidths of the individual molecules contributing to the absorption curve. In ESR studies the first derivative of the absorption curve is usually observed and the experimental spectrum would

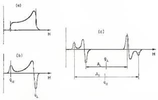

Figure 6. The ESR spectrum of a linear molecule (S = 1/2) randomly oriented in a solid matrix. (a) Absorption spectrum, where the magnetic field H is the abscissa. (b) Spectrum actually measured, the first derivative of (a). (c) Derivative spectrum obtained if the molecule also contains a magnetic nucleus with spin I = 1/2, illustrating hyperfine splittings

then appear as in Figure 6b. If the g-tensor is not too anisotropic, $g_{||}$ and $g_{\perp}$ can be readily determined as indicated in the figure. Generally, the perpendicular component can be easily distinguished in such a "powder pattern," whereas the weaker parallel line is often more difficult to detect. If nuclear hyperfine interaction is present, the pattern in Figure 6b will be split into 2I + 1 patterns if one nucleus of spin I is involved. Such a spectrum for I = 1/2 is shown in Figure 6c where, because $g_{||} \cong g_{\perp}$ and $A_{||} > A_{\perp}$, the lines for $M_I = +1/2$ and $M_I = -1/2$ are of opposite phase. If instead, $g_{\perp}$ were shifted to higher field relative to $g_{||}$ and $A_{\perp} \cong A_{||}$, the spectrum would exhibit two patterns similar to that in Figure 6b but separated by the hyperfine splitting.

When nuclear hyperfine interaction is considered, the intensity of the absorption can again be derived and is given by Eq. (37),

$$|dN/dH| = (N'/2)\{\frac{2\cos\theta}{g^2}[\frac{(g_{||}^2 - g_{\perp}^2)g_{iso}H_{iso}}{2g}$$

$$+ (M_I/\beta_e)(\frac{g_{||}^2A_{||}^2 - g_{\perp}^2A_{\perp}^2}{2A} - \frac{A(g_{||}^2 - g_{\perp}^2)}{g^2})]\}^{-1} , \quad (37)$$

where g is defined by Eq. (28) and $A^2g^2 = A_{||}^2g_{||}^2\cos^2\theta + A_{\perp}^2g_{\perp}^2\sin^2\theta$. Equation (37) cannot be solved explicitly for sinθ as in Eq. (33). This means that dN/dH cannot be written as a function of only the magnetic parameters. It is thus necessary to solve Eq. (37) and the equation for the resonant field position, Eq. (38),

$$H = (h\nu/g\beta_e) - (A/g\beta_e)M_I , \quad (38)$$

for a series of values of θ to obtain the resonant fields and intensities as a function of orientation. However, it is true that

$$H_{||} = (g_{iso}H_{iso}/g_{||}) - (M_IA_{||}/g_{||}\beta_e) , \quad (39a)$$
$$H_{\perp} = (g_{iso}H_{iso}/g_{\perp}) - (M_IA_{\perp}/g_{\perp}\beta_e) . \quad (39b)$$

and again $|d\theta/dH| = \infty$ for $\theta = 90°$

The absorption pattern for a randomly oriented molecule in which there is also nuclear hyperfine interaction is then a superposition of $2I + 1$ patterns of the type in Figures 6a and 6b. In Figure 6c where $I = 1/2$ the two patterns did not overlap and the spectrum is relatively simple. If overlap does occur, the total absorption curve and its first derivative will be more complicated and the observed spectrum may be difficult to interpret in terms of Eqs. (37) and (38). Then the best approach is to solve these equations by computer techniques for a trial set of magnetic parameters g and A at the experimental frequency ν for $\theta = 0°$ to $90°$ and have the absorption and its first derivative plotted as a function of H. It is then possible to compare the plotted spectrum with the observed spectrum and alter the parameters until a perfect fit is obtained. Several such computer programs can be found in the literature [27,31,92-95].

The Observed NbO Spectrum

Since the ^{93}Nb nucleus (100 percent natural abundance, $\mu = +6.167$ n.m.) has a spin $I = 9/2$, it is expected that the ESR spectrum of randomly oriented linear NbO molecules will exhibit in the general case a hyperfine splitting into ten perpendicular and ten parallel lines in accord with the usual axial spin Hamiltonian as given in Eq. (27). The ESR spectra observed when a mixture of Nb metal powder and Nb_2O_5 was vaporized from a resistance-heated tungsten coil and deposited in Ne and Ar matrices at 4°K are shown in Figure 7 and Figure 8, respectively. Although the expected hyperfine pattern is not observed, analysis of the spectrum reveals that this is essentially a result of the large magnitude of the magnetic parameters of NbO and that the principal features of the spectrum

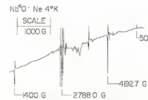

Figure 7 ESR spectrum of NbO isolated in a Ne matrix at 4°K Line positions in gauss.

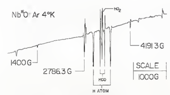

Figure 8 ESR spectrum of NbO isolated in an Ar matrix at 4°K. Line positions in gauss

are consistent with the spin Hamiltonian of Eq. (27). The zero-field splitting parameter, D, is expected to be even larger in NbO than in VO because of increased spin-orbit coupling in the heavier metal atom.

Consideration of the Expected g-Tensor for NbO

Kasai [3] has discussed the effect that the ground electronic configuration of VO, and hence the isoelectronic NbO, has upon the g-tensor of the molecule. In particular, the g-tensor expected for a $^2\Delta$ ground state, an alternative possibility [9], is quite distinct from that of a $^4\Sigma$ molecule with a large zero-field splitting parameter. In considering a simple molecular orbital (MO) scheme for the valence electrons of NbO, it is found that six of the nine valence electrons fill the lowest σ and π bonding orbitals. The remaining three valence electrons would fill the nonbonding σ and/or δ orbitals in one of three ways, depending upon the relative positions of these orbitals: (a) $\sigma^2\delta$, (b) δ^3, and (c) $\sigma\delta^2$. Cases (a) and (b) correspond to a $^2\Delta$ state while case (c) would ordinarily lead to a $^4\Sigma$ state. What are the g-tensors expected in each of these cases?

g-Tensor for a $^2\Delta$ Ground State

The δ orbital is essentially a nonbonding 4dδ orbital of the Nb atom. The spin-orbit interaction ($\lambda\bar{L}\cdot\bar{S}$) removes the twofold orbital degeneracy of this level and produces two Kramer's doublets separated by 2λ. Kramer's theorem deals with restrictions to the amount of degeneracy which can be removed by a purely electrostatic field. If the system contains an odd number of electrons, as it does here, such a field cannot reduce the degeneracy of any level below two. Each pair forms what is known as a Kramer's doublet, which can only be separated by a magnetic field. For case (a) the $\sigma\delta$ configuration gives rise to a ${}^2\Delta_r$ ground state so that the lowest level of the multiplet is ${}^2\Delta_{3/2}$, characterized by one Kramer's doublet with eigenfunctions $|M_L,M_S>$ of $|2,-1/2>$ and $|-2,+1/2>$. For case (b), the δ^3 configuration gives rise to a ${}^2\Delta_i$ ground state so that the lowest level of the multiplet is ${}^2\Delta_{5/2}$, characterized by one Kramer's doublet with eigenfunctions $|2,+1/2>$ and $|-2,-1/2>$. For these two cases the principal g-values are given by the matrix elements [41,72,96],

$$g_{||} = 2<\mu|L_z + 2S_z|\mu> = -2<\nu|L_z + 2S_z|\nu> , \qquad (40a)$$

$$g_{\perp} = 2<\mu|L_x + 2S_x|\nu> , \qquad (40b)$$

where $\bar{L}$ and $\bar{S}$ are the total orbital and spin angular momentum vectors, respectively, of the molecule and $|\mu>$ and $|\nu>$ are the two basic states of one Kramer's doublet. Thus for case (a) $g_{||}$ and $g_{\perp}$ are given by Eqs. (41).

$$g_{||} = 2<2,-1/2|L_z + 2S_z|2,-1/2> = 2.0 \qquad (41a)$$

$$g_{\perp} = 2<2,-1/2|L_x + 2S_x|-2,+1/2> = 0.0 \qquad (41b)$$

For case (b) $g_{||}$ and $g_{\perp}$ are given by Eqs. (42).

$$g_{||} = 2<2,+1/2|L_z + 2S_z|2,+1/2> = 6.0 \qquad (42a)$$

$$g_{\perp} = 2<2,+1/2|L_x + 2S_x|-2,-1/2> = 0.0 \qquad (42b)$$

Since $g_{\perp} \cong 0.0$ for a ${}^2\Delta$ molecule, the ESR spectrum of randomly oriented molecules in that case would be very broad and probably unobservable. It should also be noted that the last term containing D in the spin Hamiltonian of Eq. (27) does not contribute in either case (a) or (b).

g-Tensor for a $^4\Sigma$ Ground State

Since in case (c) the σ orbital is half filled (σ^1), the g-tensor is expected to be nearly isotropic and close to that of a free electron. However, the "apparent" g-tensor could be quite different from that of a free electron if the contribution of the term $D[S_z^2 - (1/3)S(S + 1)]$ in Eq. (27) dominates the effects of the other terms. This term represents the spin-spin interaction of the type $\bar{s}\cdot\bar{s}$ in an axially symmetric environment. It can be expected to be rather large for a system with $S = 3/2$ that is confined within the small volume of a diatomic molecule.

If the y-axis is arbitrarily chosen to be perpendicular to the applied field $\bar{H}$, then $H_y = 0$. Neglecting nuclear hyperfine interaction, the spin Hamiltonian in Eq. (27) can be written then as

$$(\mathcal{H}_{spin})_{op} = g_{||}\beta_e H_z S_z + g_{\perp}\beta_e H_x S_x$$
$$+ D[S_z^2 - (1/3)S(S + 1)] \qquad (43)$$

Taking the spin basis functions $|M_S\rangle$ as $|+3/2\rangle$, $|+1/2\rangle$, $|-1/2\rangle$, and $|-3/2\rangle$, it is possible to derive the appropriate spin energy eigenmatrix, where the only nonvanishing matrix elements for the operator in Eq. (43) are

$$\langle M_S|S_z|M_S\rangle = M_S \ , \qquad (44a)$$

$$\langle M_S|S_z^2|M_S\rangle = M_S^2 \ , \qquad (44b)$$

$$\langle M_S + 1|S^+|M_S\rangle = [S(S+1) - M_S(M_S+1)]^{1/2} \qquad (44c)$$

with $S_x = (S^+ + S^-)/2$. The following matrix is then derived, wherein $C_z = g_{||}\beta_e H_z$ and $C_x = g_{\perp}\beta_e H_x$.

$$\begin{array}{c|cccc}
 & |+3/2\rangle & |+1/2\rangle & |-1/2\rangle & |-3/2\rangle \\
\hline
|+3/2\rangle & D + 3G_z/2 & \sqrt{3}\, G_x/2 & 0 & 0 \\
|+1/2\rangle & \sqrt{3}\, G_x/2 & -D + G_z/2 & G_x & 0 \\
|-1/2\rangle & 0 & G_x & -D - G_z/2 & \sqrt{3}\, G_x/2 \\
|-3/2\rangle & 0 & 0 & \sqrt{3}\, G_x/2 & D - 3G_z/2
\end{array} \qquad (45)$$

For the condition $D >> g\beta_e\bar{H}\cdot\bar{S}$, all matrix elements of the type $<\pm 3/2|(H_{spin})_{op}|\pm 1/2> = <\pm 1/2|(H_{spin})_{op}|\pm 3/2>$ vanish. Then the matrix in Eq. (45) reduces to the following:

$$\begin{array}{c|cccc}
 & |+3/2\rangle & |+1/2\rangle & |-1/2\rangle & |-3/2\rangle \\
\hline
|+3/2\rangle & D + 3G_z/2 & 0 & 0 & 0 \\
|+1/2\rangle & 0 & -D + G_z/2 & G_x & 0 \\
|-1/2\rangle & 0 & G_x & -D - G_z/2 & 0 \\
|-3/2\rangle & 0 & 0 & 0 & D - 3G_z/2
\end{array} \qquad (46)$$

Since $H_z = H\cos\theta$ and $H_x = H\sin\theta$, the eigenvalues of Eq. (46) may be written as

$$E(M_S = \pm 3/2) = D \pm (3/2)g_{||}\beta_e H\cos\theta \ , \qquad (47a)$$

$$E(M_S = \pm 1/2) = -D \pm (\beta_e H/2)(g_{||}^2\cos^2\theta + 4g_{\perp}^2\sin^2\theta)^{1/2} \qquad (47b)$$

Here θ is the angle between the molecular axis and the externally applied magnetic field. Thus the 'apparent' g-tensors for the observable transitions $E(M_S = +3/2) \leftrightarrow E(M_S = -3/2)$ and $E(M_S = +1/2) \leftrightarrow E(M_S = -1/2)$ are

$$M_S = \pm 3/2{:}\quad g'_{||} = 3g_{||} \cong 6.0, \quad g'_{\perp} = 0.0 \qquad (48a)$$

$$M_S = \pm 1/2{:}\quad g'_{||} = g_{||} \cong 2.0, \quad g'_{\perp} = 2g_{\perp} \cong 4.0\ , \qquad (48b)$$

where the primes indicate the "apparent" g-values [30]. If D >> 0, only the transitions between $M_S = \pm 1/2$ are observable at 4°K.

It is seen that the ESR spectrum of a $^4\Sigma$ molecule is determined by the magnitude of the parameter D. The expected transitions for S = 3/2 can be obtained for any value of D by solving the 4 x 4 matrix from the Hamiltonian given in Eq. (43), where nuclear hyperfine interactions are neglected. The results, in the form of "apparent" g-values at which allowed transitions can occur, plotted versus the parameter $D/g_e\beta_e H_n$ are shown in Figure 9. As can be seen from the figure, only the $g_{||}$ transitions $M_S = +1/2 \leftrightarrow M_S = -1/2$ appear near g = 2.0 over most of the range of D, and at low D values, a triplet structure would be observed.

The Effective Spin Hamiltonian for the NbO Molecule

If it is assumed that the ground state of NbO is $^4\Sigma$ (S = 3/2) given by the configuration $\sigma\delta^2$ and that the zero-field fine structure splitting represented by the last term in Eq. (27) is much larger than either the Zeeman term, $g\beta_e\bar{H}\cdot\bar{S}$, or the hyperfine term, $A\bar{I}\cdot\bar{S}$, then the spin Hamiltonian of Eq. (27) may be rewritten to give an effective spin Hamiltonian, Eq. (49), for the transition $M_S = +1/2 \leftrightarrow M_S = -1/2$.

$$(\mathcal{H}_{spin})_{op} = g_{||}\beta_e H_z S_z + 2g_{\perp}\beta_e(H_x S_x + H_y S_y) + A_{||} I_z S_z$$
$$+ 2A_{\perp}(I_x S_x + I_y S_y) . \qquad (49)$$

In Eq. (49) $g_{||}$, $g_{\perp}$, $A_{||}$, and $A_{\perp}$ are the same as those in Eq. (27) but S is now taken to be 1/2. Following a procedure first described by Bleaney [82], the spin Hamiltonian in Eq. (49) can be rearranged to give

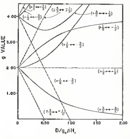

Figure 5. The "apparent" g values for ESR transitions of a $^4\Sigma$ molecule as a function of the spin spin coupling parameter $D/g_e\beta_e H_o$. Solid lines indicate transitions with the magnetic field perpendicular to the internuclear axis, dotted lines with the field parallel to the axis. Parallel transitions for $M_S = \pm 3/2$ are not shown since they occur at an effective $g = 6$.

Eq. (50), which is diagonal in the Zeeman term (see Appendix A for an outline of the method).

$$(H_{spin})_{op} = g\beta_e HS_z + AI_zS_z + [(4A_\perp^2 - A_{||}^2)/A]$$
$$\times (2g_{||}g_\perp/g^2)\sin\theta\cos\theta I_zS_x$$
$$+ (A_\perp/2)[(A_{||} + A)/A](I^+S^- + I^-S^+)$$
$$+ (A_\perp/2)[(A_{||} - A)/A]\ (I^+S^+ + I^-S^-)\ . \quad (50)$$

In Eq. (50),

$$g_\perp^2 = g_{||}^2\cos^2\theta + 4g_\perp^2\sin^2\theta,$$
$$A^2 = (A_{||}^2g_{||}^2/g^2)\cos^2\theta + (16A_\perp^2g_\perp^2/g^2)\sin^2\theta,$$

and θ is again the angle between the molecular axis and the applied magnetic field.

Fitting the NbO ESR Spectrum

It is evident from Figures 7 and 8 that a regular hyperfine splitting pattern is indeed not observed for NbO. Therefore, it is necessary to analyze the NbO spectrum by choosing appropriate initial magnetic parameters and then iterating these parameters in the 20 x 20 energy eigenmatrix resulting from Eq. (50) until a fit is obtained. Most of the discussion of the derived g- and A-tensors presented here will be for NbO isolated in an Ne matrix since the molecule is expected to be more gas-like in that environment. However, the Ar matrix spectra will be used for comparison in the assignment of lines and in making decisions about possible matrix effects. The initial parameters were chosen by reference to those for VO [3] by use of the gas-phase data for NbO, where a value of $b \cong 3A_{iso} \cong 0.19$ cm^{-1} was given [1], and by an estimate of the hyperfine anisotropy. Nuclear electric quadrupole and nuclear Zeeman effects were neglected. The initial values chosen were $g_{||} = g_{\perp} = 2.0$, $A_{||}(^{93}\mathrm{Nb}) = 1800$ MHz, and $A_{\perp}(^{93}\mathrm{Nb}) = 1550$ MHz. Only the parallel ($\theta = 0°$) and perpendicular ($\theta = 90°$) energy levels and transitions at X-band frequency ($\nu \cong 9.4$ GHz) were initially considered.

Analytical Considerations

Consideration of the spin operators in Eq. (50) shows that the only nonvanishing matrix elements are of the type

$$\langle M_S, M_I | S_z | M_S, M_I \rangle = M_S \;, \tag{51a}$$

$$\langle M_S, M_I | I_z S_z | M_S, M_I \rangle = M_S M_I \;, \tag{51b}$$

$$\langle M_S \pm 1,\ M_I | I_z S_x | M_S, M_I \rangle = \langle M_S \pm 1,\ M_I | I_z S^{\pm} | M_S, M_I \rangle$$

$$= M_I [S(S + 1) - M_S(M_S \pm 1)]^{1/2} \;, \tag{51c}$$

$$\langle M_S \pm 1,\ M_I \mp 1 | I^{\mp} S^{\pm} | M_S, M_I \rangle = [S(S + 1)$$

$$- M_S(M_S \pm 1)]^{1/2} [I(I + 1) - M_I(M_I \mp 1)]^{1/2}, \tag{51d}$$

$$\langle M_S \pm 1,\ M_I \pm 1 | I^{\pm} S^{\pm} | M_S, M_I \rangle = [S(S + 1)$$

$$- M_S(M_S \pm 1)]^{1/2} [I(I + 1) - M_I(M_I \pm 1)]^{1/2}, \tag{51e}$$

where the matrix elements of the type in Eq. (51c) vanish for $\theta = 0°$ and 90° due to the $\sin\theta\cos\theta$ term in Eq. (50).

At $\theta = 0°$ the eigenvalue matrix from Eq. (50) can be solved analytically and the magnetic fields at which resonances ($\Delta M_S = \pm 1$, $\Delta M_I = 0$) occur for each value of M_I are given by [3],

$$H(M_I) = H_{||}\{1 + \text{[illegible]}(1 + X)X + 4M_I^2X^2\}^{1/2}$$

$$- M_IA_{||}(1 + X)/g_{||}\beta_e \, . \qquad (52)$$

where $H = h\nu/g_{||}\beta_e$, $X = 4(A_{\perp}/g_{||}\beta_e)^2/[4H_{||}^2 - (A_{||}/g_{||}\beta_e)^2]$, and M_I is the component of I along its axis of quantization.

For $\theta = 90°$ the 20 x 20 spin Hamiltonian matrix can be generated in tridiagonal form and a continued fraction method may be used to obtain a reasonably accurate expression for its eigenvalues [3,97]. Use of Eq. (52) and a continued fraction expression, together with a careful consideration of the observed spectrum, initially indicated that the 4192.7 and 5049.5 G lines in the ESR spectrum of NbO isolated in an Ne matrix could be assigned as the $M_I = -9/2$ perpendicular and parallel transitions, respectively, where both $A_{||}$ and $A_{\perp}$ are assumed to be positive; moreover, the observed lineshapes are in agreement with those expected for these transitions in a sample containing randomly oriented molecules (see Figure 6). These initial considerations also indicated that the 2788.0 G line could probably be assigned as the $M_I = -7/2$ perpendicular line. Unfortunately, the continued fraction method did not allow a suitably accurate fit and, as a result, further attempts to fit the spectrum with Eq. (50) involved solving the 20 x 20 spin Hamiltonian matrix exactly.

Exact Calculations

The initial estimates of the g- and A-values were used to generate the 20 x 20 spin Hamiltonian matrix for the observed magnetic field positions at resonance and for parallel and perpendicular orientations of the field with respect to the molecular axis. The eigenmatrix was then diagonalized by computer methods and the eigenvalues and eigenvectors obtained. A detailed explanation of the computer program written to treat the specific case of the NbO molecule is given in Appendix B. The procedure used to refine the magnetic parameters involved a series of calculations diagonalizing the spin Hamiltonian matrix and using an iterative method to arrive at $A_{||}$ and $A_{\perp}$ values which were consistent with the two observed $M_I = -9/2$ lines for assumed values of $g_{||}$ and $g_{\perp}$. The final value of $g_{\perp}$ was then determined by requiring the exact calculations to produce a resonance for the $M_I = -7/2$ perpendicular line at 2788.0 G. The value of $g_{||}$ was kept fixed at an assumed value of 2.0023 for these calculations. The final values of the magnetic parameters for NbO were found to be:

$$\begin{aligned}
\text{Neon matrix:}\quad g_{||} &= 2.0023 \pm 0.0010, \\
g_{\perp} &= 1.9577 \pm 0.0010\ , \\
A_{||} &= 1586.5 \pm 0.5\ \text{MHz}\ , \\
A_{\perp} &= 1646.6 \pm 0.5\ \text{MHz}\ , \qquad (53a) \\
\text{Argon matrix:}\quad g_{||} &= 2.0023 \pm 0.0010\ , \\
g_{\perp} &= 1.9573 \pm 0.0010\ , \\
A_{||} &= 1591.7 \pm 0.5\ \text{MHz}\ , \\
A_{\perp} &= 1645.4 \pm 0.5\ \text{MHz}\ . \qquad (53b)
\end{aligned}$$

The uncertainties in the measured magnetic field positions of the observed lines are ±0.5 G except for the 1400 G line and other lines downfield from this position, all of which were measured by extrapolation and have estimated uncertainties of ±10 G.

All of the lines observed in Ne and Ar matrices, excluding obvious impurities such as HCO [98], CH_3 [99], NO_2 [100], and H atoms [32,33], are listed in Table I. Each of the prominent lines in the spectrum is accompanied by a number of weaker components. This is shown more clearly in an expanded scale for the 2788 G and 4192.7 G lines in the Ne spectrum in Figure 10 and for the corresponding lines in the Ar spectrum in Figure 11. Also shown in these figures are the effects observed when the sapphire rod is turned to different orientations, α, in the applied magnetic field, where α is the angle between the sapphire rod surface and the magnetic field direction. Variations of lineshape with α indicate nonrandom orientations of molecules in the matrices and also help to differentiate between multiple sites. An example of linear molecules oriented in a matrix with their axes parallel to the flat surface of the sapphire rod is shown in Figure 12. The extra line appearing in each region in Figure 10 when $\alpha = 90°$ is attributed to oriented molecules in an Ne matrix site different from the sites giving rise to the other lines. In the following discussion an account will be given of the shape of the strong central lines in the 2788 G region and for many of the weaker lines throughout the spectrum.

θ Versus H Curve

Angular Dependence of the Spectrum

It is evident from Eqs. (28) through (35) that the resonant field positions are strongly dependent on θ, the angle between the applied field and the symmetry axis of the molecule. This implies that the energy levels between which transitions are taking place are also dependent on θ. From Eq. (34) it is seen that not only does the intensity of the absorption depend on $dH/d\theta$ but also on $d\theta/dH$ and the latter quantity

TABLE 1

ESR Lines Assigned to NbO in Ne and Ar Matrices

Ne Matrix Observed (G)	Calculated (G)[a]	Ar Matrix Observed (G)
774	753.0 $\perp$, $\Delta M_I = \pm 1$ 776.0 $\perp$, $\Delta M_I = \pm 2$	780
1490	site	—
1400	1411.5 $\perp$	1400
2748.2	?	2758.0
2758.3	site, $\alpha = 90°$	2726.9
2775.9	site	—
2788.0*	2788.0 $\perp$	2788.3
2801.6	2802.5 $\theta = 70°$	2803.5
2832.4	2847.0 $\perp$, $\Delta M_I = \pm 2$	2834.1
3614.1	site	—
3826.7	3638.0 $\theta = 50°$	3632.7
4182.1	site	—
4192.7*	4192.7 $\perp$	4191.3
4234.5	site, $\alpha = 90°$	—
4243.2	site	—
4352.8	4364.0 $\theta = 27.5°$, $\Delta M_I = \pm 1$	—
—	site	4438.9
—	site	4454.3
5049.5*	5049.5 $\parallel$	5059.3
—	site	5148.8
—	site	5167.5

---

[a] Using magnetic parameters derived from the starred (*) lines observed in an Ne matrix as discussed in text. The nuclear electric quadrupole and Zeeman effects have been neglected. "Site" designation refers to lines attributed to molecules in minor sites in the matrices. ΔM_I indication is only approximate, all lines not otherwise indicated are essentially $\Delta M_I = 0$ transitions.

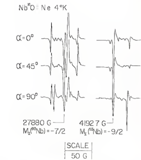

FIGURE [illegible] ESR spectra of NbO isolated in a Ne matrix at 4°K. The sapphire rod surface is oriented at the angle α to the magnetic field direction. The lines shown are the -7/2 perpendicular line at 2788.0 G and the -9/2 perpendicular line at 4192.7 G.

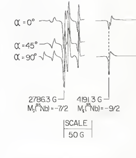

Figure 11 ESR spectrum of NbO isolated in an Ar matrix at 4°K. The sapphire rod surface is oriented at the angle α to the magnetic field direction. The lines shown are the −7/2 perpendicular line at 2786.3 G and the −9/2 perpendicular line at 4191.3 G.

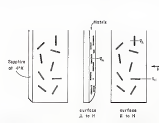

Figure 12. Linear molecules oriented in a matrix with their axes parallel to the flat surface of the sapphire rod. The two views on the right illustrate the positions of the sapphire surface perpendicular and parallel to the magnetic field H

often is a major contributor to the absorption intensity. Plots of θ versus H are thus extremely useful in interpreting an observed ESR spectrum since lines are expected to appear at fields corresponding to large values of dθ/dH. The classic paper treating the angular dependence of the resonance field for an oriented molecule with axial symmetry is that of Bleaney [82]. Similar results were obtained by Neiman and Kivelson [89] and their results were extended to include Lorentzian or Gaussian lineshapes [101] and rhombic distortions [88]. Rollman and Chan [95] generalized the results of Bleaney [82] to include quadrupole effects and effects second-order in the nuclear hyperfine interaction.

Strong and Weak Field Quantum Numbers

In addition to the important effects of the angular dependency, the hyperfine interaction depends on the strength of the external field. In zero field or in the presence of a very weak external field corresponding to a weak-field Zeeman effect, $\bar{I}$ and $\bar{S}$ are tightly coupled and the direction of quantization is that of $\bar{F}$, their resultant ($\bar{F} = \bar{I} + \bar{S}$). F takes all values from F to -F, indicated by the quantum number M_F. There are then 2F + 1 levels. As the strength of the external magnetic field H is increased, the coupling between $\bar{I}$ and $\bar{S}$ is progressively broken down until both are independently quantized along the direction of H. F is then no longer a "good" quantum number and is replaced by M_I and M_S. Vector diagrams illustrating the two cases are shown in Figure 13. It is thus possible to characterize the hyperfine levels by spin basis functions either in terms of M_F, that is, the eigenfunctions $|M_F\rangle$, or in terms of M_S and M_I, using the eigenfunctions $|M_S, M_I\rangle$. A particular hyperfine level can be completely characterized by the quantum numbers M_S and M_I (or M_F) as long as the spin basis function describing the

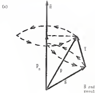

$\bar{S}$ and $\bar{I}$ precess about their resultant, $\bar{F}$ which in turn precesses about $\bar{H}$

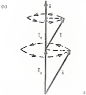

$\bar{S}$ and $\bar{I}$ both process about $\bar{H}$

Figure 1[illegible] Coupling of nuclear spin angular momentum $\bar{I}$ and electronic spin angular momentum $\bar{S}$ in (a) a weak magnetic field $\bar{H}$ and (b) a strong magnetic field $\bar{H}$

hyperfine level is "pure," that is, contains no admixtures from other spin states.

Transition Probabilities

It is also necessary to consider the probability of magnetic dipole transitions between hyperfine levels. The probability of a dipolar transition from a state M to a state M' as the result of a perturbation $(H')_{op}$—where $(H')_{op} = (\gamma h/2\pi)(2H_1\cos\omega t)J_x$ and is the effect of an oscillatory magnetic field applied in the plane normal to the applied field H—is given by [38,71]

$$P(M,M') = \gamma^2 H_1^2 |\langle M'|J_x|M\rangle|^2 f(\nu) \ , \qquad (54)$$

where $f(\nu)$ is a normalized lineshape function. In order to evaluate $P(M,M')$ it is convenient to express the operator J_x in terms of raising and lowering operators, J^+ and J^-, defined as

$$J^+ = J_x + iJ_y \quad \text{and} \quad J^- = J_x - iJ_y \ , \qquad (55a)$$

$$J_x = (J^+ + J^-)/2 \quad \text{and} \quad J_y = i(J^+ - J^-)/2 \qquad (55b)$$

These raising and lowering operators, widely used in theoretical studies of magnetic resonance, have the property that when they operate on a wavefunction $|J,M\rangle$ they generate new wavefunctions $|J,M+1\rangle$ and $|J,M-1\rangle$ in which the magnetic quantum number is raised or lowered by one unit. Then it is true that

$$J^{\pm}|J,M\rangle = [J(J+1) - M(M \pm 1)]^{1/2}|J,M \pm 1\rangle \ . \qquad (56)$$

It follows that the matrix element of J_x connecting the states M and M', that is, $\langle M'|J_x|M\rangle$ can be written in the form $(1/2)\langle M'|J^+ + J^-|M\rangle$

From the foregoing it is evident that this matrix element is nonzero only if $M' = M \pm 1$, yielding the selection rule for magnetic dipolar transitions, $\Delta M = \pm 1$, where M can be M_S, M_I, or M_p according to the states defined by $|M\rangle$. In considering transitions between hyperfine levels, it is only necessary to note that the transition probability is proportional to $|\langle M'|J_x|M\rangle|^2$, moreover, calculation of this quantity suffices for a comparison with a fully allowed ESR transition

Mixing of the Spin Basis Functions

Having determined the g- and A-tensors for NbO, it remains to prove that the other lines in the spectrum are attributable to NbO

A careful analysis of the observed spectrum indicated that the $M_I = -9/2$ parallel line at 5049.5 G (see Figure 7) is the only line observed that is clearly attributable to a parallel transition. This is not surprising since use of Eq. (52) for the parallel resonant field positions indicates that for the g- and A-values derived above, it is only for the $M_I = -9/2$ parallel transition that a real solution to Eq. (52) occurs at X-band frequencies. In other words, the hyperfine splitting is so large that only one of the expected ten parallel transitions is observable at the experimental spectrometer frequency. It is thus expected that only one parallel transition be observed and indeed only one such transition is seen experimentally.

The low field line near 1400 G (see Figure 7) has an orientation dependence similar to that of the 2788 G ($M_I = -7/2$) and 4152.7 G ($M_I = -9/2$) perpendicular lines. Therefore, it was initially thought that this line might be the $M_I = -5/2$ perpendicular line. Although an exact calculation does predict a perpendicular resonance at 1411.5 G, an examination of the eigenvectors shows that the transition cannot really be labeled as an $M_I = -5/2$ line because extensive mixing of the strong-field spin basis functions occurs.

In the event of such mixing, the ith hyperfine level is associated with a spin function ψ_i which can be approximated as a linear combination of "pure" spin basis functions, $\phi_j(M_S,M_I)$, characterized by M_S and M_I values appropriate to the jth "pure" spin basis function:

$$\psi_i = \sum_j c_j\phi_j(M_S,M_I) \tag{57}$$

In Eq. (57) the c_j are the eigenvectors associated with the eigenvalue corresponding to ψ_i. From the considerations in the preceding section, then the transition probability between two such states is proportional to

$$\begin{aligned} |\langle\sum_i c_i\phi_i|S_x|\sum_j c_j\phi_j\rangle|^2 &= 0 \text{ for } \phi_i(M_S,M_I) \\ &\neq \phi_j(M_S+1,M_I), = (\sum_{ij} c_ic_j)^2 \text{ for} \\ &\phi_i(M_S,M_I) = \phi_j(M_S+1,M_I) \end{aligned} \tag{58}$$

A calculation of the matrix elements of Eq. (58) for the 1411.5 G line indicates that this perpendicular transition has a transition probability that is 70 percent relative to a fully allowed ESR transition. The mixing of spin states is accomplished by the effects of the operators in Eqs. (51c), (51d), and (51e), all of which mix states connected by $M_S = \pm 1$. These operators, that is, I_zS_x, $I^{\mp}S^{\pm}$, and $I^{\pm}S^{\pm}$, are all seen in Eq. (50) to be preceded by factors dependent on the A-tensor values. Clearly, the larger the A-tensor, the more significant these off-diagonal matrix elements become. In the case of the NbO molecule, the large values of $A_{||}$ and $A_{\perp}$ would be expected to contribute considerably to mixing of the spin basis functions, as is observed in the calculations

A thorough examination of the eigenvectors obtained in the calculations showed that mixing of the spin basis functions is not limited to the 1400 G line. Indeed, mixing occurs even for the $M_I = -9/2$ parallel and perpendicular lines and for the $M_I = -7/2$ perpendicular line, although to a lesser extent than for other lines in the spectrum. As an example of this, the wavefunctions for the upper, ψ_u, and lower, ψ_l, states for the transitions thus far considered are listed below. In writing the expanded form of ψ_u and ψ_l only those spin basis functions $|M_S,M_I>$ are retained whose eigenvectors are of the same order of magnitude as the largest eigenvector in each case

For $\theta = 90°$ and $H = 4192.7$ G ($M_I = -9/2$) the upper and lower states are

$$\psi_u = -0.1195|1/2,-5/2> - 0.2875|-1/2,-7/2>$$

$$- 0.9461|1/2,-9/2> , \qquad (59a)$$

$$\psi_l = 0.1077|-1/2,-5/2> + 0.9912|-1/2,-9/2> \qquad (59b)$$

Since in this case $\psi_u \cong |1/2,-9/2>$ and $\psi_l \cong |-1/2,-9/2>$, the 4192.7 G line is indeed correctly considered to be the $M_I = -9/2$ perpendicular ESR transition. For $\theta = 0°$ and $H = 5048.5$ G ($M_I = -9/2$) the upper and lower states are

$$\psi_u = -0.4360|-1/2,-7/2> - 0.8999|1/2,-9/2>, \qquad (60a)$$

$$\psi_l = 1.0000|1/2,-9/2> \qquad (60b)$$

For Eqs. (60) all eigenvectors are zero other than those listed. This comes closest to being a fully allowed, "pure" $|M_S,M_I> \leftrightarrow$ "pure" $|M_S + 1, M_I>$ ESR transition between any two hyperfine levels of any considered in the present study. For $\theta = 90°$ and $H = 2788.0$ G ($M_I = -7/2$) the upper and lower states are

$$\psi_u = -0.1226|-1/2,-1/2\rangle - 0.2523|1/2,-3/2\rangle$$

$$- 0.4304|-1/2,-5/2\rangle - 0.8296|1/2,-7/2\rangle$$

$$+ 0.2138|-1/2,-9/2\rangle \ , \qquad (61a)$$

$$\psi_l = -0.2016|-1/2,-3/2\rangle - 0.7837|-1/2,-7/2\rangle$$

$$+ 0.5857|1/2,-9/2\rangle \ . \qquad (61b)$$

For $\theta = 90°$ and $H = 1411.5$ G the upper and lower states are

$$\psi_u = 0.1552|1/2,1/2\rangle + 0.2674|-1/2,-1/2\rangle$$

$$+ 0.3793|1/2,-3/2\rangle + 0.2746|-1/2,-5/2\rangle$$

$$+ 0.3742|1/2,-7/2\rangle - 0.7331|-1/2,-9/2\rangle \ , \qquad (62a)$$

$$\psi_l = 0.1111|-1/2,1/2\rangle - 0.3012|-1/2,-3/2\rangle$$

$$+ 0.2076|1/2,-5/2\rangle \ . \qquad (62b)$$

The mixing of the spin basis functions becomes more severe as lower fields are attained. Because of the extensive mixing of eigenfunctions, many so-called "forbidden" transitions ($\Delta M_I \neq 0$ or $\Delta M_S \neq \pm 1$) can be expected to contribute weaker lines to the spectrum.

In order to test the assumption that the magnitude of the fine structure term D is so large that the effect of the levels $M_S = \pm 3/2$ can be completely neglected in considering ESR transitions between the levels $M_S = \pm 1/2$, the spin Hamiltonian in Eq. (50) was diagonalized for a series of values of θ and the magnetic field H using the derived g and A-values for an Ne matrix. From the sets of eigenvalues and eigenvectors thus obtained it is possible to generate a typical θ versus resonance field plot, which is extremely useful in clearly showing the origin of the matrix spectrum as a consequence of increased intensity at large values of dθ/dH. The parallel and perpendicular transitions are usually quite evident on such a plot, but the plot may also show that "extra lines" in the spectrum result from angular anomaly effects. The existence of such "extra lines" was first pointed out by Neiman and Kivelson [89] and Coremann and Swalen [91]. On the θ versus H plot this simply means that for certain values of the magnetic parameters and quantum numbers there may be a place where dθ/dH approaches infinity other than at θ = 0° and 90°. Two such angular anomalies were found in the case of VO [3].

Generating the θ Versus H Curves

Generation of θ versus resonance field curves for the present work was straightforward only for the curve that could be identified with $M_I = -9/2$, that is, the curve connecting H = 4192.7 G at θ = 90° with H = 5049.5 G at θ = 0°. The major difficulty arose because of the way the eigenvalues and eigenvectors were designated by the computer program. The spin Hamiltonian matrix was generated by the program and the form of the matrix had already been determined by the earlier continued-fraction expansion considerations. The 20 x 20 eigenmatrix had the form

$$\begin{array}{c|cccccccccc}
 & \phi_1 & \phi_2 & \cdots & \phi_9 & \phi_{10} & \phi_{11} & \phi_{12} & \cdots & \phi_{19} & \phi_{20} \\
\hline
\phi_1 & & & & & & & & & & \\
\phi_2 & & & & & & & & & & \\
\vdots & & & & & & & & & & \\
\phi_9 & & & & & & & & & & \\
\phi_{10} & & & & & & & & & & \\
\phi_{11} & & & & & & & & & & \\
\phi_{12} & & & & & & & & & & \\
\vdots & & & & & & & & & & \\
\phi_{19} & & & & & & & & & & \\
\phi_{20} & & & & & & & & & &
\end{array} \qquad (63)$$

where ϕ_i are the spin basis functions and are given by

$$\begin{aligned}
\phi_1 &= |1/2,9/2> , \\
\phi_2 &= |-1/2,7/2> , \\
&\vdots \\
\phi_9 &= |1/2,-7/2> , \\
\phi_{10} &= |-1/2,-9/2> , \\
\phi_{11} &= |-1/2,9/2> , \\
\phi_{12} &= |1/2,7/2> , \\
&\vdots \\
\phi_{19} &= |-1/2,-7/2> , \\
\phi_{20} &= |-1/2,\ 9/2>
\end{aligned} \qquad (64)$$

In order to determine a point on the θ versus H curve the following procedure was followed, using the curve identified with the $M_I = -5/2$ transition as an example. For the derived g- and A-values and a particular value of θ, the spin Hamiltonian matrix was diagonalized for several values of H within the field range ΔH in which the curve was expected to lie. For the $M_I = -5/2$ transition, the absorption occurs between the levels characterized as $\phi_{10} = |-1/2,-5/2>$ and $\phi_{20} = |1/2,-5/2>$ so that $\Delta M_S = +1$ and $\Delta M_I = 0$ in accord with the selection rules for an allowed ESR transition. Then for a given value of θ, resonance occurs at a field H where the difference between the eigenvalues representing ϕ_{10} and ϕ_{20}, that is, E_{10} and E_{20}, equals the observed value of hν, that is, $(h\nu)_{obs}$. This approach worked very well for the $M_I = -5/2$ transition since ϕ_{10} and ϕ_{20} were essentially "pure" spin states for all values of θ and the difference $E_{20} - E_{10}$ always corresponded to $(h\nu)_{obs}$ at the proper value of H. However, due to the severe mixing of the spin basis functions in most cases, the labeling of the eigenvalues by the computer program in terms of M_S and M_I (or even M_P) becomes essentially meaningless. Consider the 1400 G perpendicular line. If this were the $M_I = -5/2$ perpendicular line then the lower and upper states would be characterized by $\phi_8 = |-1/2,-5/2>$ and $\phi_{18} = |1/2,-5/2>$. It is thus expected that the calculations would show that resonance occurs at θ = 90° when $E_{18} - E_8 = (h\nu)_{obs}$. However, the calculated perpendicular resonance at 1411.5 G occurs for $E_{20} - E_8 = (h\nu)_{obs}$ and no correlation can be made between this line and $E_{18} - E_8$. As can be seen from Eq. (62) the two levels between which this transition occurs are rather severely mixed. Thus, while a number of resonances, that is, $\Delta E = E_u - E_l = (h\nu)_{obs}$, could be predicted for various values of θ and H, it became extremely difficult to distinguish any meaningful θ versus H curves. The validity of a particular point depended very strongly on the eigenvectors, since it is evident that the transition probability is extremely important, that is, random differences between eigenvalues for a given θ and H can just as well produce an equality to $(h\nu)_{obs}$ between levels for which an ESR transition would be impossible altogether.

In an attempt to mitigate the effects of the severe mixing of the spin basis functions the computer program was modified. Considering the absolute value of the difference between two particular eigenvalues there are 190 unique numerical values for the NbO 20 x 20 spin matrix (excluding the 20 values $E_i - E_i = 0$). Thus, after diagonalization of the matrix, the program would calculate and print these 190 unique differences such that $E_i - E_j$ would be given but not $E_j - E_i$, since $|E_i - E_j| = |E_j - E_i|$. In this way possible resonance positions for various values of θ would not be overlooked due to "incorrect labeling" or eigenvalues with M_S and M_I values no longer meaningful. Even so, this added computational facility did not alleviate the necessity of examining the eigenvectors.

To circumvent this complexity, the following procedure was adopted. Plots of the 20 hyperfine energy levels versus magnetic field were prepared by plotting the 20 energy eigenvalues in 250 G intervals from 0 to 7000 G for θ = 0°, 22.5°, 35°, 40°, 45°, 50°, 55°, 67.5°, 77.5°, and 90°. The scale of the plots was 250 G/inch on the abscissa and 1×10^{-17} erg/inch on the ordinate. Since $(h\nu)_{obs} = 6.232 \times 10^{-17}$ erg, the length representing a separation corresponding to resonance on the plots was 6.232 inches, which was a quite sufficient scale. Using a pair of dividers, it was possible to estimate the field position of a spin resonance between two hyperfine levels to approximately ±20 G. The exact field position of a particular resonance for a particular value of θ could then be determined exactly by the computer methods previously described. Figure 14 gives the Zeeman plots of the derived energy levels at $\theta = 90°$, $45°$, and $0°$, and shows clearly the strong variation with θ and the mixing of levels at these intermediate fields. The solid arrows in the three parts of Figure 14 indicate the "allowed" $\Delta M_I = 0$ transitions, that is, those with the largest transition probabilities. The most intense of the "forbidden" transitions ($\Delta M_I \neq 0$ or $\Delta M_F \neq \pm 1$) are indicated by the dashed arrows in Figure 14. Use of this graphical technique immediately allowed generation of a complete θ versus resonance field plot, as shown in Figure 15. The "allowed" transitions are there indicated by solid lines and "forbidden" transitions by dashed lines. Transition probabilities relative to a fully allowed ESR transition are given in Tables II and III for the $\Delta M_I = 0$ curves of Figure 15. The θ versus H curves were readily generated by following a transition between the same two energy levels from 0° to 90° on the energy level versus magnetic field plots. This graphical technique, although tedious and time-consuming, eliminated the problems caused by "incorrect labeling" of the eigenvalues and was without doubt the most expedient means of solving this aspect of the NbO problem.

Interpretation of θ Versus H Curves

Examination of Figure 15 clearly shows the $M_I = -9/2$ perpendicular and parallel resonances at 4192.7 and 5049.5 G, respectively, as a consequence of increased intensity at large values of $d\theta/dH$. No angular anomalies result from the curve joining these two points. Also clearly indicated in Figure 15 is the $M_I = -7/2$ perpendicular line at 2788.0 G. The line calculated at 1411.5 G for $\theta = 90°$ is clearly seen in Figures 14 and 15 to result from a transition between the same two hyperfine levels as the $M_I = -7/2$ perpendicular line at 2788.0 G. As θ approaches

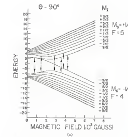

(a)

Figure 14. Energy levels and X-band transitions for $S = 1/2$, $I = 9/2$ for the spin Hamiltonian discussed in the text. The strong $\Delta M_S = \pm 1$, $\Delta M_I = 0$ ($\Delta F = \pm 1$, 0 and $\Delta M_F = \pm 1$) transitions are indicated by solid vertical lines, the weak $\Delta M_S = \pm 1$, $\Delta M_I = +1$ ($\Delta F = +1$, 0 and $\Delta M_F = \pm 2$, 0) transitions are indicated by dashed vertical lines. The diagram is for constant frequency and variable external magnetic field. θ is the angle between the applied magnetic field and the NbO molecular axis; (a) θ = 90°, (b) θ = 45°; (c) θ = 0°.

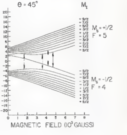

(b)

Figure 1-- continued

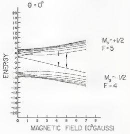

(c)

Figure 14 continued

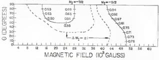

Figure 15. Θ versus resonance field. Solid curves correspond to "allowed" $\Delta M_S = \pm 1$, $\Delta M_I = 0$ ($\Delta F = \pm 1$, 0 and $\Delta M_F = \pm 1$) transitions, dashed curves to "forbidden" $\Delta M_S = \pm 1$, $\Delta M_I = \pm 1$ ($\Delta F = \pm 1$, 0 and $\Delta M_F = \pm 2$, 0) transitions. Transition probabilities relative to a fully allowed ESR transition are indicated at various points on the solid curves

TABLE II

Transition Probabilities Relative to a Fully Allowed ESR Transition for M_I = -9/2 θ Versus H Curve

θ(degrees)	H(gauss)	Transition Probability
90	4192.7	0.9481
85	4200.0	0.9460
80	4222.5	0.9395
75	4259.9	0.9305
70	4320.0	0.9145
65	4374.0	0.8955
60	4450.5	0.8721
55	4536.0	0.8444
50	4626.0	0.8140
45	4721.0	0.7820
40	4809.5	0.7498
35	4887.5	0.7276
30	4949.0	0.7144
25	4992.5	0.7150
20	5020.0	0.7263
15	5036.0	0.7534
10	5044.5	0.7799
5	5048.5	0.8010
0	5049.5	0.8100

TABLE III

Transition Probabilities Relative to a Fully Allowed ESR Transition for $M_I = -7/2$ θ Versus H Curve

θ(degrees)	H(gauss)	Transition Probability
90	1411.5	0.6961
85	1415.0	0.6911
80	1425.0	0.6916
77.5	1432.4	0.6709
75	1442.0	0.6569
70	1460.0	0.6230
67.5	1485.0	0.5900
60	1563.0	0.5014
55	1678.0	0.3432
50	2048.0	0.2439
50	2451.0	0.3504
55	2700.0	0.4825
60	2772.0	0.5574
67.5	2800.0	0.6301
70	2802.5	0.6480
75	2799.0	0.6754
77.5	2796.6	0.6856
80	2794.0	0.6936
85	2790.0	0.7039
90	2788.0	0.7076

0° these two resonances approach one another until only a single transition is possible at $\theta \simeq 49°$; hence the looped curve joining the points $H = 2786.0$ G ($\theta = 90°$) and $H = 1411.5$ G ($\theta = 90°$) in Figure 15. Examination of this curve in an expanded scale shows an inflection point at approximately 70° at a field position of 2802.5 G. An "extra line" thus results whose position is in good agreement with the strong experimental line observed at 2801.6 G (the central line pointing upward in Figure 10).

Forbidden Transitions

$\Delta M_I = \pm 1$ transitions which could possibly be observed at X-band frequencies are indicated in Figure 14 by dashed lines, however, in some cases their transition probabilities may be too small for observation. The resonance fields for these transitions were calculated as a function of θ and are shown as dashed lines in Figure 15. In considering such forbidden transitions a more exact calculation including the ^{93}Nb nuclear quadrupole moment in the spin Hamiltonian is required to answer the question of the correct transition probabilities for such resonances. These effects are not uncommon [95].

In considering forbidden transitions which gain intensity from nuclear quadrupole effects, it is instructive to consider the terms in the spin Hamiltonian arising from such effects. To include quadrupole effects in the Hamiltonian it is necessary to consider the term $Q'[I_z^2 - (1/3)I(I + 1)]$ in Eq. (26), which should then be included in Eq. (49) for the NbO case. In terms of the Hamiltonian in Eq. (50), this term in Q', the nuclear electric quadrupole coupling constant, transforms to the following:

$$(Q'/2)(3A_{\parallel}^2 g_{\parallel}^2 \cos^2\theta/A^2g^2) - 1[I_z^2 - (1/3)I(I + 1)]$$

$$- (2Q'A_{\parallel}A_{\perp}g_{\parallel}g_{\perp}\cos\theta\sin\theta/A^2g^2)[(I_zI^+ + I_zI^- + I^+I_z + I^-I_z)$$

$$+ (4Q'A_{\perp}^2g_{\perp}^2\sin^2\theta/A^2g^2)[(I^+)^2 + (I^-)^2] . \qquad (65)$$

The only nonvanishing matrix elements arising from the terms in Eq. (65) are

$$\langle M_I|I_z^2|M_I\rangle = M_I^2 , \qquad (66a)$$

$$\langle M_I \pm 1|I_zI^{\pm}|M_I\rangle = (M_I \pm 1[I(I + 1) - M_I(M_I \pm 1)]^{1/2} , \qquad (66b)$$

$$\langle M_I \pm 1|I^{\pm}I_z|M_I\rangle = M_I[I(I + 1) - M_I(M_I \pm 1)]^{1/2}, \qquad (66c)$$

$$\langle M_I \pm 2|(I^{\pm})^2|M_I\rangle = [I(I + 1) - M_I(M_I \pm 1)]^{1/2} \times [I(I + 1) - (M_I \pm 1)(M_I \pm 2)]^{1/2} \qquad (66d)$$

The states which are connected by $\Delta M_I = \pm 1$, Eqs. (66b) and (66c), have no matrix elements at $\theta = 0°$ and 90° and have a maximum value near 45° where the $\cos\theta\sin\theta$ term in Eq. (65) is a maximum. It is also true that the severe mixing of spin basis functions discussed earlier contributes considerably to the origin of the "forbidden" transitions.

The medium intensity line at 3626.7 G in the Ne matrix spectrum (see Figure 7) is attributed to a $\Delta M_I = +1$ transition with its intensity derived largely from molecules at θ near 50°, where, as seen from Figure 15, an inflection point occurs in the θ versus H curve. As Rollman and Chan [95] point out, it is expected that such a transition will be peaked in intensity near $\theta = 45°$ when the nuclear hyperfine interaction is isotropic, so is approximately the case for NbO. The inflection point in the θ versus H curve actually occurs at about 3638.0 G ($\theta = 50°$) whereas the observed line at 3626.7G is calculated to appear at $\theta = 47.3°$ with a calculated transition probability of 4 percent relative to a fully "allowed" ESR transition. The discrepancy between the measured and calculated field positions of this line will be attributed to the neglect of nuclear electric quadrupole and Zeeman effects and will be discussed later. The relatively high intensity of this "forbidden" line is accounted for by the large value of $d\theta/dH$, and thereby dN/dH, at $\theta \doteq 50°$. An examination of the eigenvectors yields the following wavefunctions for the upper and lower states between which the 3626.7 G transition occurs, where once again only the eigenvectors of the same order of magnitude as the largest one are retained:

$$\begin{aligned}\psi_u = {} & 0.2018|1/2,-7/2> - 0.4035|-1/2,-9/2> \\ & + 0.1037|-1/2,-3/2> + 0.1951|1/2,-5/2> \\ & + 0.3379|-1/2,-7/2> + 0.7892|1/2,-9/2> \ , \qquad (67a)\end{aligned}$$

$$\begin{aligned}\psi_1 = {} & 0.2633|-1/2,-5/2> - 0.3060|-1/2,-9/2> \\ & + 0.2169|-1/2,-3/2> + 0.7162|-1/2,-7/2> \\ & - 0.5180|1/2,-9/2> \qquad (67b)\end{aligned}$$

Although excessive mixing of the spin basis functions occurs, if only the dominant eigenvector is retained in each case,

$$\psi_u \cong 0.7892|1/2,-9/2> \ , \qquad (68a)$$

$$\psi_1 = 0.7162|-1/2,-7/2> \ , \qquad (68b)$$

and it is seen that the transition is essentially of the type $\Delta M_S = +1$ and $\Delta M_I = -1$. In examining the Zeeman plots of Figure 14 it is seen that the 3626.7 G transition occurs between two levels which at high field are identified with the states $|1/2,-9/2\rangle$ and $|-1/2,-7/2\rangle$. The reasoning concerning the nature of the transition is thus consistent in all respects. Also, the 3626.7 G line has an intensity about half that of the allowed perpendicular lines and resembles them in shape, as expected [3].

There is also observed in Ne matrices a weak feature at 4352.8 G which resembles a perpendicular line and is assigned to the $\Delta M_I = \pm 1$ transition expected in this region (see Figures 14 and 15). There is a very weak line at about 774 G in Ne and a corresponding although much stronger feature at about 779 G in Ar matrices (see Figure 8) which correspond to a calculated field position of 776.0 G for a forbidden $\Delta M_I = \pm 2$ transition. Such transitions should have their intensities peaked near $\theta = 90°$ [95]. Calculations also predict a $\Delta M_I = +1$ perpendicular resonance (see Figures 14 and 15) at 753.0 G, although as mentioned previously the intensity factor for such transitions is peaked near $\theta = 45°$ rather than $\theta = 90°$, however, $d\theta/dH$ is largest at $\theta = 90°$ as shown in Figure 15.

Site Effects

In Figures 10 and 11 the regions of the ESR spectrum near 2800 G and 4200 G are shown in an expanded scale for Ne and Ar matrices, respectively. Also shown are the effects observed at different orientations of the sapphire rod with respect to the external magnetic field, as mentioned previously. The 2788.0 and 4192.7 G lines in Ne and the corresponding lines at 2786.3 and 4191.3 G in Ar are considered to arise from dominant sites in the rare gas matrices. The variation of lineshape with α for these lines (see Figures 10 and 11) indicates a nonrandom orientation of the NbO molecules with respect to the sapphire rod surface [20,27]. The parallel line at 5049.5 G as well as the 1400 G and 3600 G features in Ne and Ar display variations with α also, as does the strong angular anomaly line in the 2800 G region. The 1400, 2788.0, 3626.7, and 4192.7 G lines in Ne are all accompanied by a very weak feature about 10 G downfield that exhibits the same dependency on α as the major lines. Its absence in Ar matrix spectra indicates that it probably arises from a minor site in the Ne matrix, as indicated in Table I.

In Ne the perpendicular lines display an intensity dependence on α in the order 45° > 0° > 90°, whereas the parallel line shows the order 45° > 90° > 0°. The following model is proposed to account for these observations. It is proposed that in the dominant site in the Ne matrix the NbO molecules are aligned such that the internuclear axis makes an angle of 45° with respect to the plane of the sapphire rod but are otherwise randomly oriented. The situation is shown schematically in Figure 16.

That such a model is reasonable can be seen as follows. Calculation of the angle θ between the applied magnetic field direction and the NbO molecular axis (when the angle of the field with respect to the plane of the sapphire rod is α and the angle of NbO molecular axis with respect to the plane of the sapphire rod is 45°) amounts to calculating the dihedral angle between the two planes containing the NbO molecules and the magnetic field, where the plane of the rod defines two of the three directions in a Cartesian coordinate system. The dihedral angle is zero if the planes are parallel. If the direction cosines of perpendiculars to two planes are d_x, d_y, d_z and d'_x, d'_y, d_z, then the dihedral angle θ

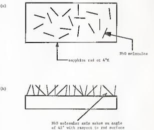
(a)
NbO molecules
sapphire rod at 4°K
(b)
NbO molecular axis makes an angle of 45° with respect to rod surface

Figure 16: Orientation of NbO molecules with respect to the plane of the sapphire rod when viewed from (a) a line normal to the rod surface and (b) along the plane of the rod

between the planes is given by [102]

$$\cos\theta = d_x d'_x + d_y d'_y + d_z d'_z \qquad (69)$$

Direction cosines are the cosines of the direction angles of a line, the direction angles are the three angles a line makes with the positive directions of the coordinate axes. Using Eq. (69) it can be shown that

$$\text{for } \alpha = 90°\text{, all } \theta = 45°, \qquad (70a)$$

$$\text{for } \alpha = 45°\text{, } \theta \text{ varies from } 0° \text{ to } 45°, \qquad (70b)$$

$$\text{for } \alpha = 0°\text{, } \theta \text{ varies from } 45° \text{ to } 90°. \qquad (70c)$$

For any value of θ between 0° and 90° there will always be a component of H oriented at 0° and 90° to the NbO molecular axis. Using Eq. (69) it can be shown that the component of H perpendicular to the NbO molecular axis is greatest overall for $\alpha = 45°$, followed by $\alpha = 0°$ and 90°, respectively. Thus, for the NbO orientation just described, it is expected that the intensities of the perpendicular and parallel lines vary with α as observed experimentally.

There are additional components of medium intensity at 2746.2, 2832.4, and 4243.2 G in the Ne matrix spectra (see Figure 9). The 2832.4 G line resembles the perpendicular lines in shape and displays the same variation with α but it is unlikely that this line arises from a site effect since it has a counterpart at 2834.1 G in Ar matrix spectra, although there it displays a different variation with the rod angle. It was consistently present in the ESR spectrum regardless of the method used to prepare NbO molecules, whereas many lines due to impurity species would appear in one experiment but not in another. This is particularly true of the g = 2 region near 3300 G (compare Figures 7 and 8). Calculations predict a $\Delta M_I = \pm 2$ perpendicular resonance at 2847.0 G, and as mentioned earlier, such transitions are peaked in intensity at the perpendicular orientation. Taking into account the quadrupole shift effect to be discussed below, it is likely that the 2832.4 G line does correspond to this $\Delta M_I = \pm 2$ transition of NbO. The 4243.2 G feature is absent in Ar matrix spectra and is then attributed to a site effect. The 2748.2 G line has a weaker counterpart at 2758.0 G in Ar and on this basis would not be expected to be a site effect; it remains unexplained. Broad weak features at 4438.9, 4454.3, 5148.8, and 5167.5 G are observed in Ar matrix spectra that have no counterparts in Ne and are thus assigned to site effects in Ar matrices, as are the weak lines observed at $\theta = 0°$ in the 2800 G region (see Figure 11).

Nuclear Electric Quadrupole and Zeeman Effects

In the preceding sections nuclear electric quadrupole and nuclear Zeeman effects have been neglected. Inclusion of quadrupole effects requires adding the term $Q'[I_z^2 - (1/3)I(I + 1)]$ to the spin Hamiltonian in Eq. (49), where Q' is given by [82],

$$Q' = 3eqQ/4I(2I - 1) . \qquad (71)$$

Here q is the electric field gradient [103-105] at the ^{93}Nb nucleus, Q $(= -0.16 \times 10^{-24}\ cm^2)$ is the quadrupole moment of the ^{93}Nb nucleus, e is the electronic charge and I = 9/2 is the nuclear spin of ^{93}Nb. It is difficult to estimate q since it involves contributions from all of the electrons outside of closed shells and also from distortions of the shells. Crude estimates for Nb^+ and Nb^{++} ions yield an order of magnitude of about +50 MHz for eqQ, but because of the high nuclear spin of ^{93}Nb the numerical factor in Eq. (71) diminishes this by 1/48, yielding $Q' \simeq +2$ MHz. The value of q is estimated from [105]

$$q = -(2J - 1)(2J + 2)^{-1}\langle r^{-3}\rangle \,, \qquad (72)$$

where $J = L + S$ is the total electronic angular momentum of the atom and is the vector sum of the total electronic orbital and spin angular momenta, taken to be 3/2 for Nb^{++} ($^4F_{3/2}$ ground state); $\langle r^{-3}\rangle$ is the expectation (average) value of the radial part of the field-gradient operator and has a value of 3.6142 au for Nb^{++} [66].

The general spin Hamiltonian of Eq. (25) contains the term $\sum_i \bar{I}_i \cdot \bar{Q}_i \cdot \bar{I}_i$ which represents the effect of nuclear quadrupole moments on the energy levels determined by interaction of electron and nuclear spins in an applied magnetic field $\bar{H}$. For a single nucleus the electric quadrupole moment Q is defined by Eq. (73),

$$Q = (1/e)\int \rho r^2(3\cos^2\theta - 1)dv = Z\langle 3z^2 - r^2\rangle \,, \qquad (73)$$

where ρ is the nuclear charge density, r is the distance from the center of gravity of the nuclear charge to the volume element dv, and θ is the angle between r and the spin axis z, Z is the atomic number and the averaging in the last expression is taken over the nuclear state with $M_I = I$. Thus Q represents the deviation of nuclear charge from spherical symmetry and is positive if the charge distribution is greater along the spin axis and negative if it is less. Q is nonzero only for nuclei with $I \geq 1$, so the complications arising from this interaction are fortunately absent for many nuclei.

Qualitatively the effect of the nuclear quadrupole moment can be interpreted as follows. The quadrupole moment, effectively a separation of charge within the nucleus, is acted upon by the crystalline electric field which, because of the nuclear magnetic coupling, determines the axis of quantization of the nuclear spins in the absence of a magnetic field. When the axis of the applied field is parallel to the symmetry axis of the crystal field, the nuclear hyperfine energy levels are shifted by an amount which depends on M_I but is independent of M_S so that the frequencies of nuclear hyperfine transitions are unaffected.

The quantitative treatment of nuclear quadrupole effects requires the addition of the term $Q'[I_z^2 - (1/3)I(I + 1)]$ to the axial spin Hamiltonian, where Q' is the interaction of Q with the gradient of the crystalline field at the nucleus, $(\partial^2V/\partial z^2)$. Q' is therefore defined by the equation

$$Q' = [3eQ/4I(I + 1)](\partial^2V/\partial z^2) \,, \qquad (74)$$

and $i_z = M_I$ to the first approximation. However, when the magnetic field is applied at an angle θ to the axis of the crystal field, second-order shifts must be taken into account and Bleaney [82,106] has shown that the equations representing the shift in the nuclear hyperfine levels contain terms in Q', θ, M_I, and M_S. This means that the shift is different for each level and the nuclear hyperfine lines are unequally spaced. It is found that the separation of the outer lines is greater or less than that of the inner lines, depending on the sign of Q. Furthermore, transitions which are forbidden by the normal selection rule $\Delta M_I = 0$ become progressively more probable as θ increases to 90° and under these conditions transitions with $\Delta M_I = \pm 1$ or ± 2 may be predominant.

If the above estimated value for Q' for NbO (41 MHz) is used in the second-order expressions of Rollmann and Chan [95] for the quadrupole contributions to $\Delta M_I = 0$ transitions, the field positions for the perpendicular transitions of NbO are shifted by less than 0.1 G. The parallel resonance is unaffected by quadrupole effects. Hence, if this order of magnitude for Q' is reasonable, the allowed transitions are essentially unchanged by inclusion of nuclear quadrupole terms. The magnetic parameters given above, calculated neglecting quadrupole effects, are then accurate.

Rollmann and Chan [95] give the following expression [Eq. (75)] for the resonance field for $\Delta M_I = 0$ transitions, including quadrupole effects and second-order hyperfine interaction. Their results are based on the earlier work of Sleeney.

$$
\begin{aligned}
H = {} & H_0 - AM_I - (A_\perp^2 g_\perp^2/4H_0 g^2)[(A_{\parallel}^2 g_{\parallel}^2 + A^2 g^2)/A^2 g^2] \\
& \times [I(I+1) - M_I^2] - (1/2H_0)[(A_{\parallel}^2 g_{\parallel}^2 - A_\perp^2 g_\perp^2)/A g^2)] \\
& \times (g_{\parallel} g_\perp^2/g^2)^2 \sin^2\theta \cos^2\theta M_I^2 + (2Q'^2 g_\perp^2 \cos^2\theta \sin^2\theta/A g^2) \\
& \times (A_{\parallel} A_\perp g_{\parallel}^2 g_\perp^2/A^2 g^4)^2 M_I [4I(I+1) - 8M_I^2 - 1] \\
& - (Q'^2 g_\perp^2 \sin^4\theta/2A g^2)(A_\perp g_\perp^2/A g^2)^4 M_I [2I(I+1) \\
& - 2M_I^2 - 1] \qquad (75)
\end{aligned}
$$

Here g^2 and $A^2 g^2$ are defined as in Eq. (50), $H_0 = h\nu/g\beta_e$, $A^2 g^4 = A_{\parallel}^2 g_{\parallel}^4 \cos^2\theta + A_\perp^2 g_\perp^4 \sin^2\theta$, and all coupling constants are expressed in gauss $A_{\parallel}(G) = A_{\parallel}(\mathrm{erg})/g_{\parallel}\beta_e$, $A_\perp(G) = A_\perp(\mathrm{erg})/g_\perp\beta_e$, $A(G) = A(\mathrm{erg})/g\beta_e$, and $Q'(G) = Q'(\mathrm{erg})/g_\perp\beta_e$. Clearly at $\theta = 0°$ the two terms in Eq. (75) involving Q' vanish and the quadrupole terms do not contribute to the positions of the resonance fields in the parallel orientation. When $\theta = 90°$ the last term in Eq. (75) must be included and this quadrupole contribution to the resonance field simplifies to $(Q'^2/2A_\perp)M_I[2I(I+1) - 2M_I^2 - 1]$. Thus the importance of the quadrupole contribution at $\theta = 90°$ depends upon the ratio $Q'/A_\perp$. As discussed by Bleaney [82] the $\Delta M_I = \pm 1, \pm 2$ transitions may have considerable intensity. Rollman and Chan [95] give an expression for the resonance fields of the $\Delta M_I = \pm 1$ transitions. By substituting k for M_I in Eq. (75), where $k = (I - 1/2), (I - 3/2), \ldots, -(I - 1/2)$, the resonance field for the transitions $|M_S, k \pm 1/2\rangle \rightarrow |M_S - 1, k \mp 1/2\rangle$ can be found by adding to Eq. (75) the quantity

$$\pm\{(kQ'g_\perp/g)[(3A^2g_{||}^4/A^2g^4)\cos^2\theta - 1)] - (g_N\beta_N H_o/g\beta_e)$$
$$\times (A_{||}g_{||}^2\cos^2\theta + A_\perp g_\perp^2\sin^2\theta)/Ag^2\} \quad . \qquad (76)$$

Because the intensity factor of these transitions has a $\cos^2\theta\sin^2\theta$ term [95], these transitions have zero intensity at both $\theta = 0°$ and $\theta = 90°$. At intermediate angles the absorption intensity also depends on the angular dependencies of g and A. In practice, the angular variations of A are greater than the corresponding variations in g and hence influence the absorption intensities to a greater extent. If the hyperfine interaction is isotropic, the intensity factor is peaked near $\theta = 45°$. When $A_{||} >> A_\perp$, the region of maximum absorption intensity, however, will generally be found at $\theta < 70°$. The intensity factor vanishes for $k = 0$ so that the $|M_S, \pm 1/2\rangle \rightarrow |M_S - 1, \mp 1/2\rangle$ transitions can be ignored.

For the case of NbO better estimates of Q' should be possible from the $\Delta M_I = \pm 1$ lines [95]. As seen above the calculated value of the prominent "forbidden" line at 3626.7 G is 11 G too high. Inclusion of the nuclear Zeeman term using Rollman and Chan's expression [95] as given in Eq. (76) increases this amount by about 2 G at $\theta = 45°$. It can be shown that a Q' value of about +20 MHz will, when used with the Q' terms from Eqs. (75) and (76), account for this discrepancy. However, a Q' of that magnitude will still have a very small effect (<1 G) upon the calculated positions of the $\Delta M_I = 0$ transitions so that the magnetic parameters above are still valid. In using Rollman and Chan's formulas for NbO, the values of $g_\perp$ and $A_\perp$ in the equations were replaced by $2g_\perp$ and $2A_\perp$. Although the use of Rollman and Chan's perturbation expressions [95] is certainly justified by the smallness of the nuclear quadrupole and Zeeman effects, the strong mixing of levels often makes M_I not a "good" quantum number here. The eigenvectors indicate contributions from many M_I levels in all of the $\Delta M_I = \pm 1, \pm 2$ transitions. The 3626.7 G transition is, however, as mentioned previously, largely a $|1/2, -9/2\rangle \leftrightarrow |-1/2, -7/2\rangle$ transition so that straightforward use of the Q' terms in Eqs. (75) and (76) with k = −4 and θ = 45° to find Q' = +22 MHz can be used. This procedure can also be applied to the 2847.0 G line, which is also in this category but is a perpendicular $\Delta M_I = \pm 2$ transition. Taking it as a $|1/2, -9/2\rangle \leftrightarrow |-1/2, -5/2\rangle$ transition, it is found that Q' = +14 MHz, in essential agreement with the previously given value of +22 MHz.

Rollman and Chan [95] give an expression also for the $\Delta M_I = \pm 2$ transitions. For the transitions $|M_S, M_I \pm 1\rangle \leftrightarrow |M_S - 1, M_I \mp 1\rangle$ where M_I can have the values $(I - 1), (I - 2), \ldots, -(I - 1)$, the resonance field is given by Eq. (75) plus the following additional term:

$$\pm \{(2M_I Q' g_\perp/g)[(3A_{\|}^3 g_{\|}^4/A^2 g^4)\cos^2\theta - 1] - (2g_N\beta_N H_0/g\beta_0)$$
$$\times (A_{\|} g_{\|}^2 \cos^2\theta + A_\perp g_\perp^2 \sin^2\theta)/Ag^2\} \qquad (77)$$

In contrast to the intensities of the $\Delta M_I = \pm 1$ transitions which go to zero at θ = 90°, the $\Delta M_I = \pm 2$ transitions reach their maximum intensity at this angle. It is also to be noted that the $\Delta M_I > 0$ transitions have zero intensity in the absence of quadrupole interaction. For a given Q' the intensity factor varies as $(Q'/A_\perp)^2(A_{\|}/A_\perp)$ for $\Delta M_I = \pm 1$ and $(Q'/A_\perp)^2$

for $\Delta M_I = \pm 2$ near the perpendicular limit where the contribution of these transitions is generally found to be most important in polycrystalline spectra [95]. Although the ratio $Q'/A_{\perp}$ may be small for a small quadrupole interaction, the intensity factors may not be completely negligible when $A_{||} >> A_{\perp}$. Furthermore, the absorption intensity of the $\Delta M_I > 0$ transitions may assume surprisingly large values as a result of unusually large values of $d\theta/dH$ [95]. This is all very consistent for the NbO ESR spectrum.

Discussion: A-Tensor

The nuclear g-factors for ^{51}V and ^{93}Nb are +1.47 and +1.37, respectively, and are therefore quite similar [107]. The observed nuclear hyperfine parameters for VO and NbO given in Table IV should thus reflect rather well the spin densities in the two cases. For a paramagnetic entity whose g-tensor deviates little from that of a free electron, the nuclear hyperfine tensor for a nucleus at an axially symmetric position can be given as [108],

$$A_{||} = A_{iso} + 2A_{dip} , \qquad (78a)$$

$$A_{\perp} = A_{iso} - A_{dip} , \qquad (78b)$$

The isotropic part of the hyperfine coupling constant, A_{iso}, can be written as [compare Eqs (20)],

$$A_{iso} = (8\pi/3) g_e g_N \beta_e \beta_N |\psi_N(0)|^2 \qquad (79)$$

This is also called the "contact" or Fermi interaction and depends upon the unpaired electron density at the nucleus, $|\psi_N(0)|^2$, to which only s electrons contribute. The term was introduced by Fermi [109] in an early

TABLE IV

Comparison of the Magnetic Parameters of VO and NbO

Parameter	VO[a,b]	NbO[a,c]
$g_{\parallel}$	2.0023	2.0023
$g_{\perp}$	1.9804	1.9577
$A_{\parallel}$ (MHz)	714.7	1586.5
$A_{\perp}$ (MHz)	837.1	1646.6
A_{iso} (MHz)	796.3	1627.0
A_{dip} (MHz)	-40.8	-20.0
$\lvert\psi(0)\rvert^2$ (au)	0.541	1.489
$\langle(3\cos^2\theta - 1)/r^3\rangle$ (au)	-0.582	-0.368

[a] All hyperfine splitting parameters are for interaction with the metal atom nucleus.

[b] g- and A-values from [3].

[c] The parameters given are derived from Ne matrix spectra.

treatment of atomic hyperfine interaction. The Fermi contact term is often stated to be a purely quantum mechanical interaction, having no classical analog, but this is not so [73]. The contact interaction can be readily understood within the framework of classical electromagnetism.

The anisotropic or dipolar part of the hyperfine coupling is given by A_{dip},

$$A_{dip} = g_e g_N \beta_0 \beta_N \langle (3\cos^2\theta - 1)/2r^3 \rangle \qquad (80)$$

This interaction arises because the nucleus and electron are each magnetic dipoles which can interact with each other at any distance r. The energy of this interaction decreases rapidly with increasing r, specifically as $1/r^3$. The interaction occurs only for electrons possessing orbital angular momentum.

The observed $A_{||}$ and $A_{\perp}$ of NbO give $A_{iso}(NbO) = 1627$ MHz and $A_{dip}(NbO) = -20$ MHz. For the ground state configuration of $\sigma\delta^2$ of NbO, since the σ and δ orbitals are essentially the nonbonding 5s and 4dδ atomic orbitals of niobium, respectively, the dominant contribution to A_{iso} comes from the σ orbital, while the dominant contribution to A_{dip} is made by the δ orbital. Thus, to a first approximation, it may be assumed that

$$A_{iso}(NbO) \doteq (1/3)A_{iso}(Nb\ 5s) \ , \qquad (81a)$$

$$A_{dip}(NbO) \doteq (2/3)A_{dip}(Nb\ 4d\delta)$$

$$= -(4/21) g_e \beta_e g_N \beta_N \langle r^{-3} \rangle (Nb\ 4d\delta) \qquad (81b)$$

Here the factor of −4/7 is included in the expression for A_{dip} to account for the angular variation of the 4dδ electrons of Nb [66]. The isotropic contribution behaves about as expected, essentially doubling in the heavier metal oxide. The anisotropic part of the hyperfine interaction with the metal nucleus changes from -41 to -20 MHz from VO to NbO and is more difficult to interpret because of negative and positive contributions to these interactions.

Crude estimates of the hyperfine interactions of 4s and 5s electrons with V and Nb, respectively, can be obtained from ScO (as Kasai [3] has done) and YO [28], or by use of Hartree-Fock calculations of $|\psi(0)|^2$ values [110]. The results of the previous ESR study of YO [28] have shown that the ground state of YO is $^2\Sigma$ and the hyperfine interaction of the unpaired electron in the σ orbital with the ^{89}Y nucleus is 0.803 GHz. Then it is possible to use Goudsmit's relation [111], in which the isotropic hyperfine constant is proportional to the quantity

$$g_N Z_i Z_o^2 \kappa(Z_i)/n_o^3 , \qquad (82)$$

where g_N is the nuclear g-factor, Z_i is taken as the real nuclear charge, $Z_o = 1$ for neutral atoms, $Z_o = 2$ for singly ionized atoms, and so forth, n_o is the principal quantum number, and $\kappa(Z_i)$ is a relativity correction. The results from use of Goudsmit's relation and Hartree-Fock values [110] agree rather well, yielding $A_{iso}(\text{Nb } 5s) \cong 3.9$ GHz, from which $A_{iso}(\text{NbO}) \cong 1300$ MHz. From the expressions $A_{iso}(\text{VO})/A_{iso}(\text{V})$ and $A_{iso}(\text{NbO})/A_{iso}(\text{Nb})$ it can be shown that the s-spin density at the metal atoms is about 30 percent in VO and about 40 percent in NbO. It is gratifying that these spin distributions are consistent with $s\delta^2$ configurations, which as stated earlier, imply 1/3 s-character to the first approximation.

The value of $\langle r^{-3}\rangle_{(\text{Nb } 4d\delta)}$, necessary for interpretation of A_{dip}, is more difficult to estimate, particularly since the anisotropic contributions can arise from $d\sigma$, $d\delta$, or even $p\sigma$ electrons. However, $A_{dip}(\text{Nb})$ contributions from these electrons will always be at least an order of magnitude smaller than A_{iso}(Nb). A rough estimate of $<r^{-3}>_{(Nb\ 4d\delta)}$ can be made from a spectroscopically determined spin-orbit coupling constant of the Nb atom in a manner described by Barnes and Smith [112]. In their expression $<r^{-3}>$ is given by the following expression:

$$<r^{-3}> = hc\lambda/2(\ell + 1/2)\mu_e^2 Z_i \ . \tag{83}$$

Here h is Planck's constant, c the speed of light, λ the spin-orbit coupling constant, ℓ the orbital angular momentum quantum number, μ_e the electron magnetic moment, and Z_i an effective atomic number given by (Z − n), where Z is the true atomic number and n the principal quantum number. The d-electron spin-orbit coupling constant of Nb can be taken as about 520 cm^{-1} from Hartree-Fock calculations [110] or, alternatively, as about 646 cm^{-1} from the observed multiplet levels of the Nb^{++} ion in the $^4F(4d^3)$ state [113]. Using the Hartree-Fock value of 520 cm^{-1}, a value of $<r^{-3}>_{(Nb\ 4d\delta)} \cong$ − 96 au is obtained, this yields A_{dip}(Nb 4dδ) $\cong$ −36 MHz. Thus A_{dip}(NbO) is about −24 MHz, in reasonable agreement with the observed value of −20 MHz.

Figure 17 depicts an approximate molecular orbital diagram for NbO where the 5sσ and 4dδ nonbonded levels may be quite close together and may even be interchanged in energy. TaO, the next heavier member of Group VB, has a $^2\Delta_r$ ground state derived from a $\sigma^2\delta$ configuration [4-6]. The 5sσ level is probably partially hybridized with the 4dσ so that each of these orbitals should be depicted as mixtures, but with the latter strongly bonding. This same scheme applies to VO [3], but with the principal quantum numbers of the metal reduced by one and with the 4p orbital higher in energy relative to the 4s. The fact that A_{dip} for both molecules is negative (the sign of $A_{\parallel}$ and $A_{\perp}$ seems clearly positive here) establishes that the principal dipolar hyperfine interaction comes

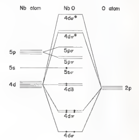

Figure 17 Schematic molecular orbital diagram for the valence electrons of NbO Molecular orbitals are indicated here relative to the Nb atom since that designation is most relevant to the ESR and optical transitions of NbO The vertical energy scale is strictly qualitative

from dδ electrons, but some spin density could also be in the dσ and perhaps even the pσ orbitals. The latter two contributions to A_{dip} are positive [66]. Then the change in the negative A_{dip} from VO to NbO (see Table IV) indicates a shift of spin density from dδ to s, dσ, or perhaps pσ, or a shift of s-contribution into dσ or pσ. The very approximate calculation of the s-contributions in VO and NbO is against a large shift there, but in any case it seems likely that there is a larger spin occupation of 4dσ or 5pσ in NbO than in the corresponding orbitals in VO.

If it is assumed that NbO is more ionic than VO, then the 4dσ level would lie higher in NbO and participate more in the nonbonding levels. This conclusion is based on a crystal-field theory model [6,7,114-116]. In zero approximation the molecule is considered as completely ionic, that is, $Nb^{++}O^{--}$, so that the three d electrons on the Nb atom lie in the strong cylindrically symmetrical field produced by the O^{--} ion. The degenerate 4d levels are then split into three increasingly energetic levels, δ, π, and σ, in the $C_{\infty v}$ field. Thus, in the simplest case, the three electrons would be placed in the δ level resulting in a δ^3 configuration (other than closed shells). This would lead to a $^2\Delta_i$ inverted ground state, which is of course not observed. In the case of TaO [6], the stability of the molecule indicates that the dπ electrons, d_{xz} and d_{yz}, should be allowed to form π-bonds with the oxygen, thereby altering the simple ionic model by covalent bonding and the formation of appropriate molecular orbitals. However, although these π-bonds may lower the dπ orbitals below the dδ, they only replace the filled unbonded p orbitals of the oxygen so that the same configuration results, that is $^2\Delta_i$. For TaO the experimental evidence [6] strongly suggested that the ground state is $^2\Delta_r$. Multiplets formed from equivalent electrons are regular when less than half the shell is filled, as in a δ configuration, for example, but inverted when more than half the shell is occupied, as in a δ^3 configuration [117-119]. In order to obtain a $^2\Delta_r$ ground state as in TaO, it is necessary to also lower the $d\pi$ level below the $d\delta$. This could perhaps be done by allowing some sd hybridization to occur since the 6s and 5d orbitals of Ta can mix [6,120,121]. Calculations [122] on TiO indicated, however, that there the 3dσ orbitals are largely bonding and not the 4s. Extending the scheme to TaO, Weltner and McLeod [6] derived a final configuration of $\sigma^2\delta$ for TaO, yielding a $^2\Delta_r$ state. Clearly, the same arguments can be applied to VO and NbO, except there the final configurations are $\sigma\delta^2$, giving a $^4\Sigma$ ground state. As mentioned earlier, then, the 4dσ level in NbO lies higher than the 3dσ level in VO if NbO is more ionic. Hence, increased dσ or pσ spin occupation in NbO is a reasonable conclusion from the observations.

The value of the hyperfine constant b determined in the gas phase [37,123] is approximately 0.19 cm^{-1}. For the NbO case, $b = 3(A_{iso} - A_{dip})$ and the neon matrix spectrum data yield a value of 0.165 cm^{-1}. This is another indication of the validity of the present results, particularly since the gas-phase value of b is only an approximate one [37].

Discussion. g-Tensor

It has been shown that for an orbitally degenerate ground state, the deviation of the g-value along a particular principal axis, i, from that of a free electron can be given by [3,32,33,35,36,61,124]

$$\Delta g_i = -2\lambda \sum_{n \neq 0} \langle 0|L_i|n\rangle\langle n|L_i|0\rangle/(E_n - E_0) \qquad (84)$$

Here λ is the spin-orbit coupling constant of the relevant atom, and $E_n - E_0$ gives the energy separation between the ground state, $|0\rangle$, and the other state, $|n\rangle$, into which the unpaired electron may be promoted via a spin-orbit interaction. In particular, for axial symmetry, the following equations are applicable

$$\Delta g_{\parallel} = -(\lambda/2)\Big[\sum_{n\neq 0} \langle n|L_z|0\rangle/(E_n - E_0)\Big]^2 , \qquad (85a)$$

$$\Delta g_{\perp} \approx -2\lambda \sum_{n\neq 0} \langle n|L_x|0\rangle\langle 0|L_x|n\rangle/(E_n - E_0) . \qquad (85b)$$

When the ground state $|0\rangle$ is a Σ state the only states which can be mixed in by the operators in Eq. (85b) are excited states $|n\rangle$ which must be Π states. Evidently terms involving Π states are coupled via $\lambda\vec{L}\cdot\vec{S}$ interaction with the ground state to mix in some orbital angular momentum and thereby alter g_e. The lower-lying the Π state and the larger the value of λ the more effective the coupling.

$g_{\parallel}$ should always be less than g_e and, since the term in brackets in Eq. (85a) is small and squared, it is usually true that $g_{\parallel} \cong g_e$ or $\Delta g_{\parallel} \cong 0$. However, $\Delta g_{\perp}$ is more affected by the coupling and it can be positive or negative, depending upon the character of the Π states involved. In general, the lowest-lying Π state will dominate the summation so that the higher states can be neglected and the sign of $\Delta g_{\perp}$ will depend upon whether that excited state has the properties of an electron in a π orbital or of a "hole" in a π orbital. Another way of stating this is to say that the spin-orbit coupling constant, λ, is positive in the first case and negative in the second. For example, in MO notation, the excited state could be obtained by excitation of a ground $^2\Sigma$ state with a configuration $\pi_1^4\sigma^1$ to $\pi_1^4\pi_2^1$ ($^2\Pi_r$ state) or to $\pi_1^3\sigma^2$ ($^2\Pi_i$ state). Mixing a $^2\Pi_r$ state with the ground state would cause $\Delta g_{\perp}$ to be negative, whereas a $^2\Pi_i$ state would cause $\Delta g_{\perp}$ to be positive. If several excited states must be considered, then their individual effects on $\Delta g_{\perp}$ must be considered. However, in the simplest case, if the experimental value of $\Delta g_{\perp} < 0$, usually a $^2\Pi_r$ excited state would lie lowest and if $\Delta g_\perp > 0$, a $^2\Pi_i$ state lowest.

Since for the NbO molecule $\Delta g_\perp < 0$, it is implied that regular Π states are coupled to the $X^4\Sigma^-$ state via spin-orbit interaction. The lowest-lying excited states which could significantly couple to the $(4d\delta)^2(5s\sigma)^1\ X^4\Sigma^-$ state of NbO are the $^4\Pi$ states produced by excitation to the following configurations

$$(4d\delta)^2(4d\pi^*)^1\ ,$$

$$(4d\delta)^1(5s\sigma)^1(4d\pi^*)^1\ .$$

Note that $5p\pi^*$ will couple to the ground state only if $5p\sigma$ character is mixed with the σ nonbonding orbital. Such $^4\Pi$ states have not yet been unequivocally identified from optical spectroscopic studies. However, a negative $\Delta g_\perp$ shift was also observed for VO (see Table IV), but was not as large as in NbO, in qualitative agreement with its smaller spin-orbit coupling constant.

As discussed later in Chapter IV on the optical spectrum of NbO, at least one of the $^4\Pi$ states may lie about 14,000 cm^{-1} above the ground state. A corresponding level in VO occurs at 795.6 nm, which is 12,566 cm^{-1} above the ground state [123]. If the d-electron spin-orbit coupling constants, λ, of VO and NbO are taken as about 180 and 520 cm^{-1}, respectively, from Hartree-Fock calculations [110] and the experimental $\Delta g_\perp$ (see Table IV) is used in the expression

$$\Delta g_\perp = -(4/3)(\lambda/\Delta E)c^2\ , \qquad (86)$$

then the value of c^2 can be obtained. Equation (86) is derived from Eq. (85b) where $\Delta E = E_n - E_0$ and c is the coefficient of the $3d\delta$ or $4d\delta$

atomic orbital is a linear combination of atomic orbitals (LCAO) wavefunction for the ground state of VO or NbO. The numerical factor of 4/3 in Eq. (86) comes from an evaluation of the matrix elements of the L_x operator of the form $<4d\pi^*|L_x|4d\delta>$, where the only nonvanishing matrix elements are of the type

$$<M_L \pm 1|L_x|M_L> = [(L \mp M_L)(L \pm M_L + 1)]^{1/2}/2 \ , \qquad (87)$$

and from the fact that for orbitally nondegenerate states of multiplicity higher than two, the expression in Eq. (85b) must include the factor 1/S [61]. Equation (86) assumes that in the excited $^4\Pi_r$ state the excited electron is entirely in a $4d\pi^*$ orbital on the metal atom and that the $4d\sigma$ hybridization with the $5s\sigma$ atomic orbital is small in the ground state. It is found that $c^2(NbO) = 0.90$ and $c^2(VO) = 1.15$. Although these are very approximate calculations, the results are reasonable, particularly when compared with the hyperfine analysis of the preceding section. Both sets of data are consistent with the $\sigma\delta^2\ {}^4\Sigma^-$ assignment for the ground electronic state of the NbO molecule.

CHAPTER IV

THE OPTICAL ABSORPTION SPECTRUM OF THE NbO MOLECULE

The Blue System ($^4\Sigma^- - {}^4\Sigma^-$)

This system occurs in the gas phase [1,8,9] and in a Ne matrix in the region 460 nm to about 400 nm, as shown in Figure 19. The observed bands and the derived band separations for $Nb^{16}O$ and $Nb^{18}O$ are given in Table V along with a comparison of the gas-phase data.

The excited states of both $Nb^{16}O$ and $Nb^{18}O$ in this system are perturbed in a Ne matrix by interaction with nearby excited states of a system designated as system X. The band positions and derived band separations of this perturbing system are given in Table VI. The interaction of the $^4\Sigma^-$ system and the X system is shown schematically in Figure 19, where the double-headed arrows indicate that the unperturbed levels have interacted to yield the observed levels listed there. Reference to Figures 18 and 19 shows that in $Nb^{16}O$ the (1,0), (2,0), and (3,0) levels of the $^4\Sigma^-$ system interact most strongly with system X, whereas in $Nb^{18}O$ the (2,0), (3,0), and (4,0) levels of the $^4\Sigma^-$ system are perturbed most strongly. The longest wavelength observed band of the X system shows an isotope shift and can be shown to be the (1,0) band of that system by use of Eq. (88) [118],

$$\Delta\nu = (1 - \rho)v\Delta G_{v+1/2} \qquad (88)$$

Here $\Delta\nu$ is the isotope shift in cm^{-1} of the band characterized by a

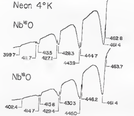

Figure 18. The observed $^4\Sigma^-$ and perturbing X systems of NbO in an Ne matrix at 4°K Lower spectrum $Nb^{18}O$, upper spectrum $Nb^{16}O$ Band wavelengths given in nm.

TABLE V

Comparison of Observed NbO Absorption Bands for the $^4\Sigma^-$ System in Gas and in a Ne Matrix at 4°K

(v',v")	λ(nm)	ν(cm^{-1})	$\Delta G_{v'+1/2}$ (cm^{-1})
Nb^{16}O Gas Spectrum^a			
(0,0)	469.00	21316	
(1,0)	451.17	22160	844
(2,0)	434.71	22997	837
(3,0)	419.57	23827	830
(4,0)	405.56	24650	823
(5,0)	392.55	25467	817
Nb^{16}O Ne Matrix Spectrum:^{b}			
(0,0)	461.44(5)	21665	
(1,0)	443.91(3)	22521	856
(2,0)	428.33(3)	23337	816
(3,0)	413.53(4)	24175	838
(4,0)	399.65(10)	25015	840
Nb^{18}O Ne Matrix Spectrum^b			
(0,0)	461.41(5)	21667	
(1,0)	445.00(10)	22466	799
(2,0)	429.28(3)	23283	817
(3,0)	415.79(4)	24044	761
(4,0)	402.36(5)	24846	802
(5,0)	390.26(10)	25617	771

[a] Band origins from [9]

[b] Matrix spectra corrected by Hg lines in this region

TABLE [illegible]

Observed NbO Absorption Bands for X System in a Ne Matrix at 4°K

(v',v")	λ(nm)[a]	ν(cm^{-1})	$\Delta G_{v'+1/2}$ (cm^{-1})
Nb^{16}O X System			
(1,0)	462.75(2)	21604	
			879
(2,0)	444.66(3)	22483	
			924
(3,0)	427.11(4)	23407	
			877
(4,0)	411.68(3)	24284	
			840
(5,0)	397.92(10)	25124	
Nb^{18}O X System			
(1,0)	463.74(2)	21558	
			846
(2,0)	446.22(2)	22404	
			829
(3,0)	430.31(2)	23233	
			876
(4,0)	414.66(2)	24109	
			827
(5,0)	400.91(5)	24936	

[a] Matrix spectra corrected by Hg lines in this region.

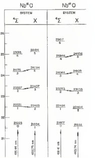

Figure 19- Vibrational levels in the excited electronic states of NbO $^4\Sigma^-$ and perturbing X systems and their interactions. A double-headed arrow indicates interaction between levels. Distance from the v″ = 0 level of the ground state is given in cm^{-1}; the number below each level indicates v′

vibrational quantum number v and an average band separation $\Delta G_{v + 1/2}$ for the progression to which the band belongs. ρ is the value of the isotopic frequency ratio calculated as

$$\rho_{calc} = \nu(Nb^{18}O)/\nu(Nb^{16}O) = [\mu(Nb^{16}O)/\mu(Nb^{18}O)]^{1/2} \qquad (89)$$

or obtained from the observed data as

$$\rho_{obs} = \nu_{obs}(Nb^{18}O)/\nu_{obs}(Nb^{16}O) \; , \qquad (90)$$

where the ν are the observed or calculated vibrational frequencies (in cm^{-1}) of the $Nb^{16}O$ or $Nb^{18}O$ molecule and μ is the appropriate reduced mass. For NbO, ρ_{calc} is 0.9513. Assuming perturbations in the $v' = 1$ and $v' = 5$ levels of system X and in the $v' = 0$ and $v' = 4$ levels of the $^4\Sigma^-$ system are negligible in the $Nb^{16}O$ systems, it is possible to determine the unperturbed levels of both systems from the usual relation [118] for the wavenumbers of a line in an electronic vibrational progression,

$$\nu = \nu_e + \omega_e'(v' + 1/2) - \omega_e'x_e'(v' + 1/2)^2$$
$$- \omega_e''(v'' + 1/2) + \omega_e''x_e''(v'' + 1/2)^2 \; , \qquad (91)$$

where ω_e', $\omega_e'x_e'$, etc., have their usual meanings and the gas-phase values [9] were used. Similar considerations allow calculation of the unperturbed levels of the $Nb^{18}O$ $^4\Sigma^-$ and X systems. These results and the derived vibrational frequencies in the excited states are given in Table VII. The ratios ρ of the vibrational frequencies for the two isotopic molecules listed in Table VII for both the $^4\Sigma^-$ and X systems of the NbO molecule are in satisfactory agreement with the theoretical value of 0.9513. From these considerations the numbers are derived for the first four columns of Table VIII and, with the use of Eq. (92), the matrix

TABLE VII

Unperturbed Band Positions and Vibrational Frequencies in Excited Electronic States of NbO $^4\Sigma^-$ and X Systems

(v',v'')	ν (cm^{-1})	$\Delta G_{v'+1/2}$ (cm^{-1})	ν (cm^{-1})	$\Delta G_{v'+1/2}$ (cm^{-1})	ρ[a]
	$Nb^{16}O$ $^4\Sigma^-$ System		$Nb^{18}O$ $^4\Sigma^-$ System		
(0,0)	21665		21667		
		848		805	0.949
(1,0)	22513		22472		
		842		798	0.948
(2,0)	23355		23270		
		834		793	0.951
(3,0)	24189		24063		
		828		786	0.949
(4,0)	25017		24849		
	$Nb^{16}O$ X System		$Nb^{18}O$ X System		
(1,0)	21604		21562		
		892		849	0.952
(2,0)	22496		22411		
		884		842	0.952
(3,0)	23380		23253		
		877		834	0.951
(4,0)	24257		24087		
		869		827	0.952
(5,0)	25126		24914		

[a] Theoretical value for isotopic ratio $\rho = 0.9513$

TABLE VIII

Interaction Between Vibrational Levels of Upper Electronic States in $^4\Sigma^-$ and X Systems of NbO.

v' $^4\Sigma^-$	X	Distance Apart of Unperturbed Levels = δ(cm^{-1})	Separation of Observed Bands (cm^{-1})	Matrix Element W_{ij}(cm^{-1})
		$Nb^{16}O$ Systems		
0	1	61	61	0
1	2	17	36	17
2	3	25	70	33
3	4	66	109	43
4	5	109	109	0
		$Nb^{16}O$ Systems		
0	1	105	109	15
1	2	61	62	6
2	3	17	50	47
3	4	24	65	30
4	5	65	90	31

elements W_{ij} for the interaction between the vibrational levels of the excited states of the two systems are calculated [118,125] and listed in the last column of Table VIII.

$$E = (1/2)(E_i + E_j) \pm (1/2)(4|W_{ij}|^2 + \delta^2)^{1/2} . \qquad (92)$$

Here E represents the perturbed energy and $\delta = E_i - E_j$ is the separation of the unperturbed levels.

Thus the interaction between the vibrational levels of the excited states of the $^4\Sigma^-$ and X systems causes the unperturbed levels to move apart, and the separation is largest for the (2,0) and (3,0) levels of the $^4\Sigma^-$ system. The nature of the observed matrix spectra indicate that the transition to the X excited state is intrinsically weak and that it only appears by "stealing" intensity from the intense $^4\Sigma^- \leftarrow X^4\Sigma^-$ systems. Perturbations are also observed in the gas phase [126] and matrix [20] in the green system of VO at 573.9 nm, which is presumably the counterpart of this blue system in NbO.

The conditions for nonvanishing W_{ij}, that is, the selection rules for perturbations as they are determined by the quantum numbers and symmetry properties of the states i and j are [118]: (a) both states must have the same total angular momentum $J (\Delta J = 0)$; (b) both states must have the same multiplicity ($\Delta S = 0$); (c) the two states must differ in Λ value such that $\Delta\Lambda = 0, \pm 1$, (d) both states must be positive or both must be negative ($+ \nleftrightarrow -$), and (e) for identical nuclei, both states must have the same symmetry in the nuclei ($g \nleftrightarrow u$). Rules (a), (d), and (e) are perfectly rigorous. The second rule ($\Delta S = 0$) holds only approximately and rule (c) ($\Delta\Lambda = 0, \pm 1$) holds only as long as Λ is defined, that is, in Hund's cases (a) and (b), in Hund's case (c) it must be replaced by $\Delta\Omega = 0, \pm 1$. There is no strict selection rule for the vibrational quantum number v, but as a rule, to the Franck-Condon principle holds is that two vibrational states belonging to two different electronic states and lying at approximately the same level will influence each other strongly only if classically the system could go over from one state to the other without a large alteration of momentum and position.

Although the data are insufficient to allow precise determination of the nature of the X system, excitation to such configurations as $\delta^2\sigma^*$, $\delta^2\pi^*$, or $\delta\sigma\pi^*$ gives rise to $^2\Sigma^-$ and $^2\Pi$ states which could be low-lying. The $\sigma\delta^2$ ground-state configuration also gives rise to a $^2\Sigma^-$ state which would be expected to be low-lying. Transitions such as $^2\Sigma^- \leftarrow X^4\Sigma^-$ and $^2\Pi \leftarrow X^4\Sigma^-$ would be expected to be weak within the framework of the selection rules for perturbations, but internal spin-orbit coupling effects from the heavy Nb atom could be expected to relax the selection rule forbidding doublet-quartet transitions and Hund's case (c) coupling in the perturbing state would tend to relax the rule for Λ. Thus, low-lying $^2\Pi$ or $^2\Sigma^-$ states are likely candidates for the X system.

In Ar matrices the blue system of the NbO molecule consists of a series of very broad bands. It is difficult to even assign band positions confidently for the Ar spectra and to detect any perturbations similar to those observed in the Ne matrix spectra. Observation of the blue system in both Ne and Ar matrices provided accurate verification of the presence of NbO molecules in these matrices and as such was a very valuable diagnostic tool in the experimental work.

The Red Systems

Several strong and moderately intense systems have been observed in the region 740 nm to about 530 nm for Nb^{16}O and Nb^{18}O isolated in Ne and Ar matrices at 4°K. These red systems for Nb^{16}O in Ne are shown in Figure 30

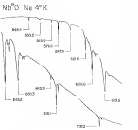

Figure 20 The observed Nb^{16}O absorption bands in the region 540-740 nm in a Ne matrix at 4°K. Band wavelengths are given in nm. Gaps in the solid lines indicate changes in slit-width so that the relative intensities of bands are not depicted accurately

and in Ar in Figure 21. From the gas-phase studies [8,127] at least two systems of NbO are expected to be observed in this region.

In Ne there are five distinct progressions in which the isotopic shifts establish the (0,0) bands. The progressions are listed in Table IX and are designated as A, A', B, C and D. As seen from Figure 20 the (0,0) bands of the A and A' systems look very much alike, that being the reason for their similar designations. There are consistently observed weaker bands at slightly longer wavelengths than the more intense bands and analysis of these, where measurable, yields the same vibrational progressions as their stronger counterparts. Two of these systems, persisting even after annealing of the matrices, are listed in Table IX where they are assigned to molecules in other matrix sites.

The spectra observed in Ar are similar to those in Ne and again there are site effects. The Ar bands are listed in Table X. Several broad absorption features in Ar (at 709.8 nm, for example; see Figure 21) do not form progressions and have no counterparts in the Ne spectra. Presumably they are not due to NbO. There is also a weak system of sharp bands with (0,0) at 657.7 nm (designated as system E in Table X), not observed in Ne matrices, which has a unique vibrational spacing, indicating that it does not arise from a site effect. However, the remaining five systems correlate well with those observed in Ne matrices. The positions of the (0,0) bands and the vibrational frequencies in the five systems in Ne and Ar matrices are compared in Table XI. Also included in Table XI are the strongest lines observed in the gas phase, as listed by Rosen [128]. These are presumably the rotational branch heads which fall in the groups indicated, approximately centered about the matrix bands. As is often the case, the solid-state perturbations in Ne and Ar matrices are such that the matrix bands bracket the gas phase

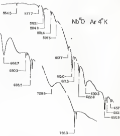

Figure 21 The observed Nb^{16}O absorption bands in the region 540-740 nm in an Ar matrix at 4°K Band wavelengths are given in nm Gaps in the solid lines indicate changes in slit-width so that the relative intensities of bands are not depicted accurately

TABLE IX

Observed Absorption Bands of NbO in a Ne Matrix at 4°K in the Region 540 to 740 nm

Band System	v'	λ(cm^{-1})	ν(cm^{-1})	$\Delta G_{v'+1/2}$ (cm^{-1})
		Nb^{16}O Systems		
A	0	731.0	13676	899
	1	685.9	14575	
A'	0	691.1	14467	
B site	0	660.9	15127	884
	1	624.4	16011	
B	0	655.3	15256	883
	1	619.5	16139	875
	2	587.6	17014	865
	3	559.2	17879	861
	4	533.5	18739	
C site	0	646.9	15454	900
	1	611.3	16354	906
	2	579.2	17260	894
	3	550.7	18154	
C	0	643.2	15544	900
	1	608.0	16444	896
	2	576.6	17340	891
	3	548.4	18231	
D	0	601.6	16618	932
	1	569.6	17550	

TABLE IX (continued)

Band System	v'	λ(nm)	ν(cm^{-1})	$\Delta G_{v' + 1/2}$ (cm^{-1})
		Nb^{18}O Systems		
A	0	730.9	13678	861 (0.958)^a
	1	687.6	14539	
A'	0	691.0	14468	
B site	0	660.9	15127	840 (0.950)^a
	1	626.1	15967	
B	0	655.3	15256	839 (0.950)^a
	1	621.2	16095	831 (0.950)^a
	2	590.7	16926	826 (0.950)^a
	3	563.2	17752	
C site	0	647.3	15444	857 (0.952)^a
	1	613.3	16301	857 (0.946)^a
	2	582.7	17158	849 (0.950)^a
	3	555.2	18007	
C	0	643.3	15542	851 (0.946)^a
	1	609.9	16393	853 (0.952)^a
	2	579.7	17246	850 (0.954)^a
	3	552.5	18096	
D	0	601.7	16615	886 (0.951)^a
	1	571.2	17501	

[a] Numbers in parentheses are observed values for isotopic ratio ρ, the theoretical value is 0.9513.

TABLE X

Observed Absorption Bands of Nb^{16}O in an Ar Matrix at 4°K in the Region 540 to 740 nm

Band System	v'	λ(nm)	ν(cm^{-1})	$\Delta G_{v'+1/2}$ (cm^{-1})
A	0	735.3	13596	886
	1	690.3	14482	
A'	0	695.5	14374	
B	0	666.7	14995	866
	1	630.3	15861	876
	2	597.3	16737	
E	0	657.6	15206	846
	1	622.8	16052	848
	2	591.6	16900	
C site	0	653.5	15299	891
	1	617.5	16190	905
	2	584.8	17095	
C	0	650.9	15360	895
	1	615.0	16255	896
	2	583.1	17151	878
	3	554.5	18029	
D	0	610.7	16370	935
	1	577.7	17305	

TABLE XI

Comparison of $Nb^{16}O$ Spectra in Ne and Ar Matrices in the 540 to 740 nm Region with the Strong Bands Observed in the Gas Phase

System (v',v") or Band (v',v")	Neon Matrix Band (nm)	Neon Matrix $\Delta G_{v'+1/2}$ (cm^{-1})	Gas Phase[a] Lines (nm)	Argon Matrix Band (nm)	Argon Matrix $\Delta G_{v'+1/2}$ (cm^{-1})
A(0,0)	731.0	899	---	735.3	886
A'(0,0)	691.1	---	702.73 696.94 695.09	695.5	---
B(0,0)	655.3	883	673.73 663.33 659.10 657.60	666.7	866
C(0,0)	643.2	900	649.96 649.59 648.44 647.39	650.9	895
B(1,0)	619.5	---	622.83	630.3	---
C(1,0)	608.0	---	615.49 612.45 612.00	615.0	---
D(0,0)	601.6	932	---	610.7	935

[a] Most intense lines in gas-phase spectrum as listed by Rosen [128].

date. The ESR spectra demonstrate that the molecules are not rotating in these matrices (see Chapter III). What is designated as system C in the present work has also been observed recently in Ar matrices [2].

The low-lying states to which transitions are allowed are likely derived from excitation to either the $5p\pi^*$ or $4d\pi^*$ levels. Thus excitation to either $\delta^2\pi^*$ or $d\sigma\pi^*$ configurations will provide excited $^4\Pi$ upper states to which transitions from the ground state are fully allowed in Hund's case (a) coupling (see the discussion of the g-tensor in Chapter III). A counterpart here is the $^4\Pi - X^4\Sigma^-$ system of VO at 795.6 nm [37]. Spin-orbit coupling in $^4\Pi$ states gives rise to $\Omega = 5/2$, $3/2$, and two $1/2$ substates with expected multiplet splittings on the order of 500 cm^{-1} for NbO (see Chapter III). If the selection rule $\Delta\Omega = 0, \pm 1$ is considered, then there are three possible allowed transitions to a $^4\Pi$ state from the ground $^4\Sigma_{1/2}$ state. If Hund's case (a) coupling, the components of these multiplets would be equally spaced so that three equally spaced (0,0) bands should be observed in the matrix spectra for each excited $^4\Pi$ state. States A, A', and B in Ne (see Table X) are 791 and 789 cm^{-1} apart but these values are 778 and 621 cm^{-1} in Ar (see Table XI). A similar but more widely spaced triplet is the A', C, and D states, which are split in Ne by 1077 and 1074 cm^{-1} and by 986 and 1010 cm^{-1} in Ar.

However, usually in matrices, subbands of multiplets can be expected to have the same general appearance since matrix influences will be the same on each substate. As noted above, the A and A' systems are remarkably similar and thus expected to belong to the same multiplet. Although the site effects are somewhat different, the C and D bands are also sharp and not unlike the A and A' bands. The B bands, however, are noticeably broader (about 50 cm^{-1} at half-height) than the others and

This argues against their being derived from the same excited state(s) as the other four systems.

Combining these observations, it is difficult to unambiguously assign three subsystems as belonging to the expected $^4\Pi - {}^4\Sigma$ transition with Hund's case (a) coupling in the $^4\Pi$ state. What is clear is that more systems are observed in the red region of the spectrum than can be explained by a single $^4\Pi - {}^4\Sigma$ transition. If there is a tendency towards Hund's case (c) coupling, as appears to be the case in the TaO spectrum [5,6], then additional transitions to $\Omega = 3/2$, and 1/2 substates of the $^2\Pi$ states (in the same configuration as the excited $^4\Pi$ states) become more allowed [124-132]. Additional transitions and loss of multiplet equal spacings are then expected. It is also possible that excitation into a $d\sigma^*$ or $p\sigma^*$ orbital could lead to another $^4\Sigma \leftarrow X^4\Sigma$ transition in this region; for example, the unique B system could be accounted for on this basis.

In Chapter III it was shown that the observed perpendicular component of the g-tensor of the NbO molecule could be satisfactorily accounted for by ascribing at least one of these transitions observed in the red systems to a $^4\Pi_r \leftarrow X^4\Sigma^-$ transition derived from excitation into a $4d\pi^*$ MO. Excitation into a $5p\pi$ level could not provide the coupling of angular momentum needed to account for $\Delta g_\perp$. Hence no direct evidence of the relative energy of the $5p\pi$ and $5p\sigma$ levels is obtained from this work, although in Figure 17 of Chapter III they are considered as low-lying. Since previous considerations of some transition-metal oxides, most specifically TiO [6,10], have placed the $p\pi$ level higher than the $d\pi^*$, there appears to be some doubt about how these levels are ordered throughout the series and to what particular electronic excitations the observed optical transitions should be assigned.

The Infrared Absorption Spectrum

Infrared spectra were recorded for Ne matrix samples only. For the purpose of presenting the IR results three types of experiments are to be distinguished: (1) vaporization of pure Nb_2O_5 from a tungsten cell, (2) vaporization of Nb/Nb_2O_5 mixtures from a tungsten cell, and (3) passing O_2 gas over hot Nb metal in a tungsten cell. For all three types of experiments a medium to strong intensity band was observed at 973 cm^{-1} which is assigned to $Nb^{16}O$. This band was strongest in the type (3) experiments and weakest in the type (1) experiments, as expected. The appearance of the band was actually that of a triplet, with bands at 965.5, 973.0, and 977.1 cm^{-1} for $Nb^{16}O$ and at 917.6, 925.5, and 929.8 cm^{-1} for $Nb^{18}O$, as shown in Figure 22. The observed isotope frequency ratios of 0.9504, 0.9512, and 0.9516 are in essential agreement with the theoretical value of 0.9513 for diatomic niobium oxide. Also, the values for $Nb^{16}O$ are slightly lower than the gas-phase value of 981.4 [9], as is usually the case in matrix spectra. Green and coworkers [2] have recently reported a similar IR spectrum of NbO in an Ar matrix. The triplet structure observed by these workers at 964, 968, and 971 cm^{-1} for $Nb^{16}O$ and at 918, 921, and 924 cm^{-1} for $Nb^{18}O$ is attributed by them to probable multiple stable matrix sites since the triplet structure persists even after the matrices are annealed. It is interesting to note that such a triplet structure for the IR band was not found for VO [20] or TaO [6] in Ne and Ar matrices. It is unusual to have identical site effects in Ne and Ar matrices. The triplet splittings are, however, slightly different in the two cases. Further experimentation is required to determine the nature of the IR triplet. Possibly use of Kr and Xe rare-gas matrices would shed some light on the origin of the triplet structure

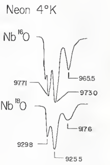

Figure 22. The observed Nb^{16}O and Nb^{18}O infrared absorption bands in a Ne matrix at 4°K. Lower spectrum Nb^{18}O upper spectrum Nb^{16}O Band positions given in cm^{-1}.

The remainder of the observed NbO IR spectrum in Ne is not easily interpreted. In almost every experimental spectrum several IR bands were observed that were due to various tungsten oxide species trapped in the matrix [125]. It is expected from mass spectrometric data [52] that besides NbO there should be present also NbO_2 in nearly equal concentration. However, no bands in the observed IR spectra could be clearly assigned to either a linear or bent NbO_2 molecule and the electronic spectra also exhibited no band systems attributable to a triatomic species. Both TaO_2 [6] and WO_2 [125] exhibit very characteristic spectra involving long progressions of the bending frequency in the upper state.

CHAPTER V

CONCLUSIONS: THE NbO MOLECULE

Results

The present matrix ESR and optical data establish that the ground electronic state of the NbO molecule is $^4\Sigma^-$, in accord with recent analyses of the gas-phase transitions [1,2]. Indeed, the hyperfine parameter $b = 0.165$ cm^{-1} determined here is very close to the approximate value of 0.19 cm^{-1} indicated by observed hyperfine splittings in the $^4\Sigma^-$ - $^4\Sigma^-$ system in the gas phase [1]. In view of the substantial agreement between the hyperfine parameters of NbO measured in Ne and Ar matrices, it is likely that the matrix value is accurate.

Comparison with Other Diatomic Oxides

Previous discussions [7,10] of the ground states of the Group IV and Group V transition-metal oxides has pointed out that similarities between second- and third-row diatomic oxide molecules might be expected. Thus NbO was predicted to have a $^2\Delta_r$ ground electronic state like TaO [6]. The present results show that this is not the case, but it is interesting to note that the Nb atom is also anomalous. Although V and Ta, the atoms above and below Nb in the Periodic Table, have $^4F_{3/2}(d^3s^2)$ ground states, that of Nb is $^6D_{1/2}(d^4s)$ [113]. In contrast, Ti, Zr, and Hf atoms are all $^3F(d^2s^2)$ while the ground states of the molecular oxides are $^3\Delta_r$ for TiO and $^1\Sigma^+$ for ZrO and HfO [7,10,113].

The ground states of the transition-metal diatomic oxides known and/or postulated at the present time are as follows [10,37].

Group IIIB: ScO, YO, LaO, all $^2\Sigma^+$,

Group IVB: TiO, $^3\Delta_r$, ZrO and HfO both $^1\Sigma^+$,

Group VB: VO and NbO both $^4\Sigma^-$, TaO, $^2\Delta_r$,

Group VIB: CrO, ?$^3\Sigma^-$ or ?$^5\Pi$, MoO and WO both ?$^3\Sigma^-$.

The remaining transition Groups are not well characterized although CuO($^2\Pi_1$) and ZnO($^1\Sigma^+$) are known. Clearly, matrix studies such as the present one contribute vital information in filling the existing gaps in knowledge about the ground electronic states of transition-metal diatomic oxides.

PART TWO

ELECTRON SPIN RESONANCE SPECTROSCOPY OF PHENOTHIAZINE RADICAL CATION COMPLEXES WITH DEOXYRIBONUCLEIC ACIDS

CHAPTER VI

INTRODUCTION: TRICYCLIC ANTIPSYCHOTIC DRUGS AND NUCLEIC ACIDS

Tricyclic Antipsychotic Drugs

The most emphatic influence on the fate of schizophrenic patients in the history of psychiatry has been the use of the phenothiazines and related drugs [133]. Observing that promethazine, a phenothiazine derivative possessing potent antihistaminic activity, showed pronounced

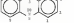

Phenothiazine

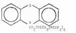

Promethazine

sedative effects and prolonged the action of barbiturates, French workers attempted structural modifications of this drug, hoping to find a compound with enhanced central nervous system (CNS) activity [134-136]. In the course of this study Charpentier [137] in 1950 synthesized chlorpromazine (CPZ) and Courvoisier and coworkers [138] reported on amazing

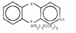

Chlorpromazine

diversity of pharmacological properties for this drug, including striking CNS-depressant effects. The demonstration in 1952 by Delay, Deniker, and Harl [139] that CPZ was effective in treatment of various psychiatric disorders revealed a most unique and useful antipsychotic action of this compound. Chlorpromazine was not only able to calm the hyperagitated psychotic but left the patient in a cooperative state, allowing him to participate in occupational, recreational and psychotherapies, whereas medications available prior to the use of CPZ caused such excessive sedation in patients that adequate therapy was thwarted [135]. The 1954 report of Lehmann and Hanrahan [140] was a significant confirmation of these clinical findings and described the use of CPZ in the treatment of psychomotor excitement and manic states [135,136]. Also in 1954, CPZ was marketed in the United States as an antiemetic and was rapidly recognized as a notably efficacious agent for the treatment of nausea and vomiting [135,136]. Since then the published literature on chlorpromazine in particular and substituted phenothiazine derivatives in general has experienced an explosive proliferation. Excellent reviews of the substituted phenothiazines treating the subject from different points of view have been given by Boelme, Hudson, and Zografi [135], Zirkle and Kaiser [136], Schenker and Herbst [141], Bradley [142], Gordon [143,144], and Bodea and Silberg [145]. A striking indication of the journalistic explosion is illustrated by the 1963 review of Schenker and Herbst [141] on phenothiazines and azaphenothiazines as medications. The review is 358 pages long and contains 102 tables (extending over 173 pages) listing phenothiazine derivatives (with literature references) known up to the time the review was written. These tables contain over 3000 separate entries and the review article lists 6800 references!

Since the introduction of CPZ as a neuroleptic (antipsychotic) drug, thousands of new phenothiazine derivatives have been synthesized and studied pharmacologically, as well as related tricyclic derivatives such as phenoxazines, phenoselenazines, acridans, acridines, thioxanthenes, xanthenes, anthracenes, and dihydroanthracenes, and tricyclic compounds with a central seven-membered ring [136]. Nearly 150 of these phenothiazine compounds have been investigated clinically for psychotropic activity [136] and about 50 phenothiazine derivatives are used in human therapy [135].

No biochemical or physiological disorder has been identified as a causative factor of the functional psychoses and their etiology is unknown; moreover, the mechanism of action of antipsychotic drugs is also obscure, the drugs being palliative rather than curative agents [136]. In particular, the mechanism of action of neuroleptics at the molecular level that are responsible for their pharmacological effects are not clearly understood, although numerous observations indicate that at least some of the pharmacological effects of reserpine, the phenothiazines, and other types of antipsychotic agents may be due to interference with the actions of norepinephrine and dopamine [136]. Although no single unifying concept has yet been developed to rationalize generally structural requirements for psychotropic activity, structure-activity relationships do provide a modicum of predictability among individual chemical classes of drugs. Stereochemical considerations as well as such physical properties as water solubility, lipid-water partitioning, acid-base properties, and surface activity are undoubtedly quite important in determining neuropharmacological activity [136]. Numerous authors have treated the subject and its different aspects [134-136,143,144,146-168].

It is well established [134-136] that the neuropharmacological activity of phenothiazine derivatives may be influenced both qualitatively and quantitatively by the aminoalkyl side chain in the 10-position, as well as by nuclear substitution of the phenothiazine ring. In general, a basic amine group separated by three carbon atoms from the phenothiazine nucleus is optimal for antipsychotic activity. Shortening the chain length to two carbons, as well as branching of the ethylene bridge, decreases CNS-depressant activity and enhances autonomic effects. The nature of the basic amino function in the side chain may influence antipsychotic potency of phenothiazine derivatives to a considerable extent, with a basic tertiary amine substituent exhibiting maximum potency. Introduction of a variety of substituents into the 2-position of a 10-aminoalkylated phenothiazine may significantly affect neuroleptic potency. Conditioned-response data in rats show that 2-substitution increases neuroleptic potency in approximately the following order [136] $OH < H \cong CONHNH_2 \cong OCH_3 < C(CH_3)_3 < CH_3 \cong CH(CH_3)_2 < COCH_3 \cong CO_2CH_3 \cong SO_2N(CH_3)_2 \cong SCH_3 \cong Br \cong Cl \cong SCF_3 < SO_2CF_3 \cong CF_3$. This order is only an approximation, however, since it is based on several different conditioned-response procedures and, in addition, the order may be influenced by the 10-aminoalkyl moiety [136]. The antipsychotic potency of phenothiazine derivatives may be enhanced by introduction of an appropriate substituent in the 3-position, but this effect is much less significant than that for the 2-position. Substitution of the 4-position apparently decreases CNS-depressant properties somewhat, while the effect of 1-substitution on psychopharmacological activity has not been studied extensively [136].

The great diversity of the structures of the various types of neuroleptic drugs raises a major obstacle to analysis of structural requirements for neuroleptic activity. In the case of the phenothiazines, the pharmacology is exceedingly complex and the drugs affect many different physiological sites [135]. For instance, the substituted phenothiazines act in the central nervous system, causing sedation (without anesthesia or hypnosis), blockade of conditioned-avoidance behavior, antiemetic effects, temperature regulation alteration, changes in skeletal muscle tone, an antipruritic effect, analgesic effects, facilitation of seizure discharge, and endocrine alterations. The phenothiazines also act on the autonomic nervous system, causing cholinergic blocking effects at nicotinic and muscarinic receptor sites, adrenergic blocking and potentiating effects, antihistaminic effects, antiserotonin effects, and prevention of the uptake of biological amines such as norepinephrine into tissues. The actions of various other drugs, such as alcohol, barbiturates, and morphine, are potentiated by the phenothiazines. The substituted phenothiazines also act as local anesthetics.

To complicate matters more, the phenothiazines differ both qualitatively and quantitatively in the extent to which each produces such pharmacological effects [135]. The phenothiazines also vary in degree of concomitant adverse side effects such as agranulocytosis, photosensitivity, extrapyramidal symptoms, jaundice, and pigmentary retinopathy. The use of phenothiazine itself in human therapy is precluded due to its toxicity in producing anemia, hepatitis, and undesirable dermatological reactions, although it is still used in veterinary practice as an anthelmintic [135]. Domino, Hudson, and Zografi [135] have stated eloquently that the substituted phenothiazines are "a true Pandora's box that when opened lets out some evil as well as much good."

Structural features that have been found to be necessary for potent neuroleptic activity in the series of phenothiazine derivatives and their analogs are (1) a tricyclic ring system with either a six- or seven-membered central ring, (2) a chain of three atoms joining a terminal amino group to the central ring, and (3) a substituent such as chloro or trifluoromethyl at a position *meta* to the atom of the central ring from which the side chain projects [136]. Variation in any one of these structural features appears to reduce neuroleptic potency to a considerable extent. Next to the phenothiazines one of the most important groups of neuroleptic agents is the butyrophenones, of which haloperidol

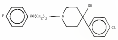

Haloperidol

in the prototype [136]. The butyrophenones are quite different from the phenothiazines in structure but very similar in many of their pharmacological properties. It is not known whether the butyrophenones act at and in the same way with the sites at which the phenothiazines interact, but if they do, structural requirements for neuroleptic activity would be rather nonspecific, as is true for local anesthetics [136]. Clearly there is much to learn about the molecular basis of drug action. The task is awesomely complex and extraordinarily intriguing. Intensive research will hopefully lead to a basic understanding of the molecular processes underlying physiological drug action in the future.

Nucleic Acids

Nucleic acids, discovered in 1869 by Miescher, who found them in pus corpuscles, fish sperm, and other biologic material, are, like proteins, large macromolecules [169-174]. They are among the largest molecules known and have molecular weights measured in billions of daltons. In some microorganisms it is believed that all the deoxyribonucleic acid (DNA) exists as a single molecule with molecular weights ranging from 10^6 to 10^8 or even in excess of 10^9 daltons. Nucleic acid molecules are strongly acidic and at physiological pH carry a high density of negative charge. As a result, they are found associated in the cell with various cationic species, frequently with basic proteins such as the histones, sometimes with oligoamines such as cadaverine, $H_2N(CH_2)_5NH_2$, putrescine, $H_2N(CH_2)_4NH_2$, spermidine, $H_2N(CH_2)_4NH(CH_2)_3NH_2$, or spermine, $H_2N(CH_2)_3NH(CH_2)_4NH(CH_2)_3NH_2$, and very commonly with the alkaline earth cations, particularly Mg^{2+}.

The two general types of nucleic acid are deoxyribonucleic acid (DNA), a constituent of cellular nuclei, and ribonucleic acid (RNA), located primarily in the cytoplasm outside the cellular nucleus. Pure nucleic acids contain approximately 15 percent nitrogen and 10 percent phosphorus. They contain heterocyclic nitrogenous bases, which are substituted purines or substituted pyrimidines, that cause a strong absorption in the UV with a peak near 260 nm. Per gram atom of phosphorus nucleic acids contain one molecule of a sugar, either D-ribose in RNA or 2-deoxy-D-ribose in DNA.

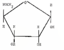

D-Ribose

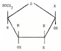

2-Deoxy-D-ribose

The true monomeric units of nucleic acids are the nucleotides, which are sugar-phosphate esters of the corresponding nucleosides, these being carbohydrate derivatives in which the purine or pyrimidine bases are linked to the sugar moiety through a β-N-glycosyl bond. The organic bases in nucleic acids are, as stated above, either pyrimidines or purines,

Pyrimidine

Purine

the common bases in DNA being the pyrimidines thymine (T) and cytosine (C) and the purines adenine (A) and guanine (G), whereas most RNA molecules contain the purines adenine and guanine and the pyrimidines cytosine and uracil (U). Careful enzymatic and chemical degradations compose an overwhelming amount of evidence indicating that naturally occurring polynucleotides, particularly the two types of nucleic acids proper, all have the same basic structure of a linear polymer in which successive monomeric nucleotide residues are linked to one another by phosphate groups *via* 3',5'-phosphodiester bridges between the pentoses of adjacent nucleoside units.

Thymine

Cytosine

Uracil

Adenine

Guanine

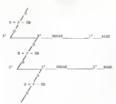

Most of the cellular DNA is concentrated in the cell nucleus in all organisms except viruses and bacteria, whereas RNA is found in almost all cell fractions. Chloroplasts, mitochondria, and other large organelles which are potentially self-reproducing have been found to contain extra-nuclear DNA. Deoxyribonucleic acid in bacteria appears to be present in one to three aggregates or nucleoids in the cellular interior (but connected to its membrane). In those viruses containing DNA it has been found to occupy the central region of their spherical or polyhedral head structure. For all these organisms it is believed that DNA is the genetic material, the genetic information being both stored and transmitted in these macromolecules, whereas RNA appears to be functionally involved in the various phases of protein biosynthesis.

Although the chemical constituency of nucleic acids was known for a long time, the structure remained elusive until 1953. The pioneering investigations of Chargaff and Lipshitz [175] on the base composition of a large variety of DNA molecules isolated from numerous sources lead to several generalizations which have been thoroughly confirmed. These may be summarized as follows [169].

(a) The nucleotide base composition of the DNA of an organism is characteristic of that organism (species).

(b) Different cells of tissues of a particular organism have identical or at least closely related nucleotide base composition, moreover, the base composition is unaltered by age, development, nutritional state, and all other environmental or physiological factors.

(c) From organism to organism the actual base composition varies widely from about 25 to 75 mole percent $(G + C)$, the variation being greater for bacteria than for higher organisms, the variation is usually expressed by the so-called dissymetry ratio, $(A + T)/(G + C)$.

(d) Closely related organisms have similar nucleotide base compositions.

(e) Certain chemical regularities defined by Chargaff's rules are exhibited by all "normal" DNA molecules: (1) $A = T$, (2) $G = C$, (3) $A + G = C + T$ (purines = pyrimidines), and (4) $A + C = G + T$.

(f) Since $A + G + C + T = 1$, a corollary to Chargaff's rules is that any nucleic acid not exhibiting the above regularities must possess certain unusual structural features.

The alkali metal salts of DNA can be spun into fibers or unidimentional crystallites exhibiting sharp and regular X-ray diffraction patterns. On the basis of the chemical data discussed above and fiber X-ray diffraction data, particularly that of Wilkins on the lithium salt of DNA, Watson and Crick [176,177] proposed a radically new concept for the structure of the DNA molecule in which the molecule consists of two polynucleotide strands which fit together to form a right-handed double-stranded helix. This model provided a means of expressing basic biological processes in precise structural chemical terms for the first time. It proved to be the catalyst for the revolution in biological thinking that has occurred since, and Watson, Crick, and Wilkins were awarded the Nobel Prize in 1962 for their contribution.

In aqueous solution DNA exists primarily in the B conformation, which is one of several double-helical geometries of DNA elucidated by fiber X-ray diffraction studies [178]. In the B conformation the DNA molecule consists of two right-handed helical polynucleotide chains of opposite polarity, that is, the internucleotide linkage in one strand is 3' → 5' and is 5' → 3' in the other. The two polynucleotide chains are plectonemically coiled around the same axis to form a double helix which cannot therefore be separated into its constituent coils without unwinding. The nucleotide bases lie on the inside of the helix in such a fashion that a purine on one chain always pairs with a pyrimidine of the other and vice versa. Only certain pairings of the bases can be accommodated spatially and these are A paired with T and C paired with G, the base pairs being hydrogen bonded. Since these pairing relations require that the two chains are complementary, the base pair sequence of one strand is completely determined by the sequence in the other. The B form is characterized by an overall diameter of about 2 nm with the base pairs stacked so that they lie perpendicular to the helical axis and are slightly twisted relative to one another. The interbase hydrogen bonding pattern is that first defined by Watson and Crick [176,177] and the helical axis passes approximately through the N-H···N imine hydrogen bond. The right-handed helix has 10 base pairs per turn and makes one complete turn every 3.4 nm, which is called the pitch. These features give the helix an exact tenfold screw axis with the sense of the screw being right-handed. There is thus a rise per base pair residue of 0.34 nm

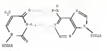

Thymine Adenine

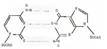

Cytosine Guanine

Because one complete turn of the helix amounts to 360° of rotation, the angle between successive base pairs is 36°. The distance between the C_1' carbon atoms in the deoxyribose rings of the antiparallel strands is about 1.1 nm and the hydrogen bonds range from 0.28 to 0.295 nm in length. As a result of the N-9 purine glycosidic bond and the N-1 pyrimidine glycosidic bond, the sugar-phosphate residues lie on the same side of each base pair, giving rise to two distances between the sugar-phosphate backbones in the helix. This establishes the so-called grooves in the double-helical structure as depressions between the negatively charged, hydrophilic sugar-phosphate backbones. In the B conformation the large (major) groove is about 2.2 nm across, measured between phosphates in the direction of the helical axis, and the small (minor) groove is about 1.2 nm across on the same basis, both grooves being about 0.7 nm in depth (measured from the surface of the enveloping cylinder).

In the fiber or gel state the B conformation of DNA readily converts to the A form, which is observed at decreased relative humidities and with counterions other than Li^+, or to the C form, observed in Li-DNA at relative humidities less than 66 percent. The base pairs in the A configuration are tilted about 20° from perpendicularity to the helical axis and are also displaced outward from the helical axis with 11 base pairs per turn and a rise per residue of 0.282 nm. The A conformation resembles the structure of double-stranded RNA at 100 percent relative humidity. The C conformation is similar to the B conformation but has only 9.3 base pair residues per turn with a rise per residue of 0.332 nm. At present it is thought that native DNA may well exist in solution in a variety of differing conformations resembling the B form established by fiber X-ray diffraction but which differ in topological detail depending on solvent environment or local base sequence variations.

As might be expected, the years since the work of Watson and Crick [176,177] have seen an ever expanding literature on nucleic acids appear. Today the study of nucleic acids and their functions and interactions with other molecular species comprises a broad field of scientific inquiry populated by researchers from an astoundingly large number of formal disciplines. The continued interest in nucleic acids is evidenced by such publications as the series Progress in Nucleic Acid Research and Molecular Biology (Academic Press) and the numerous review articles and research papers appearing weekly in scholarly journals. The enormous complexity of dealing with macromolecular nucleic acids necessitates approaches from many different attitudes. This is evident from the numerous review articles appearing within the past four years. Several examples are cited to illustrate the proliferation of the results of nucleic acid research throughout the literature. Reviews have appeared on the eukaryotic chromosome [179], the structure and synthesis of ribosomal RNA [180], the sequence analysis of transfer, ribosomal, and viral RNA [181], the physical chemistry of nucleic acids [182], the interactions of antibiotic drugs and nucleic acids [183], the biosynthesis of DNA [184], circular DNA [185], transfer RNA research [186], DNA-protein interactions [178], DNA replication [187], mitochondrial nucleic acids [188], the structure and function of bacterial ribosomes [189], in vitro transcription of various types of DNA [190], restriction or degradation in bacterium-infected cells and host-controlled modifications of DNA [191], the relevance of transfer-RNA-dependent translational control of protein synthesis to the aging process [192], the transcription of reiterated DNA sequence classes throughout the life span of the mouse as an approach to a working hypothesis of senescence [193], the structure and function of phage RNA [194], the metabolism of nuclear RNA [195], the structure of chromosomes and chromosome fibers [196], electronmicroscopy of genetic activity [197], regulation of transfer RNA [198], the electronmicroscopy of DNA [199], methods of gene isolation [200], the replication of circular DNA in eukaryotic cells [201], and DNA sequencing techniques [202]. Clearly nucleic acid research is one of the most exciting and dynamic areas of research at the present time.

The Interaction of DNA with Other Molecules

General Considerations

Since nucleic acids are polyanions, they must be accompanied by the appropriate number of cations in their vicinity to maintain electroneutrality

[189]. Numerous investigations have shown that DNA interacts with inorganic cations, certain dyes and antibiotics, polyamines, cationic polypeptides, certain synthetic polymers, and the natural "unstructured" basic chromosomal proteins, the histones and protamines [178].

The alkali metal cations, Li^+, Na^+, K^+, Rb^+, and Cs^+, and some of the alkaline earth cations, such as Mg^{2+} and Ca^{2+}, bind electrostatically to DNA primarily as counterions to the negatively charged phosphate backbone [189,178]. The monovalent cations are loosely bound and form a counterion atmosphere around the phosphates, but more tightly bound cations such as Mg^{2+} and Mn^{2+} form stoichiometric, site-bound complexes with the phosphate groups [189,178]. Certain metal ions, such as Ag^+, Hg^{2+}, Cu^{2+}, and Zn^{2+}, exhibit additional binding features besides the simple electrostatic interactions with phosphate groups. These ions appear to recognize additional functional groups of DNA, show base specificity, and in some cases, can be used as conformational probes. The binding mechanisms are often very complex and can differ in mono- and polynucleotides [178]. Research on the interaction between positively charged polyamines and polypeptides and DNA has been considerable since, biologically, the interactions are of some interest. Polyamines occur in association with DNA in viruses and prokaryotic organisms and basic polypeptides can be viewed as simplified models of at least some of the interactions with DNA of the histones and protamines, which are an integral part of the eukaryotic chromosomes [189,178]. These studies are of peripheral interest to the present work and detailed review is beyond the scope of the present study. The binding of certain dyes and antibiotics is, however, directly relevant to the present work.

The interaction of nucleic acids with certain polynuclear, aromatic planar cationic (basic) dyes, such as the acridines (proflavine, acridine orange, and so forth) is of great interest. Dyes of this type have long

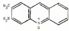

Acridine yellow

been used as biological stains capable of binding to and thereby rendering visible DNA or RNA by virtue of their absorption or fluorescence [163]. The subject continues to be of pressing interest, results [203] recently being reported on biophysical studies of the common technique of chromosomal staining with quinacrine. Such dyes are also recognized as highly selective and potent mutagens, being capable of apparently producing additions or deletions of single nucleotides in the course of DNA replication and of specific inhibition of this process. Several interactions are possible between such dyes and DNA. At low dye-DNA ratios complexes may form in which a single positive charge on the dye is lined up opposite to one on the phosphate, with the dye essentially parallel to the nucleotide bases, thereby increasing the diameter of the helix. A dipositively charged dye molecule may line up along the helix axis and crosslink two phosphate residues on either the same or on opposite chains and thereby enhance the stability of the helix. A third alternative at low dye-DNA ratios is that a dye molecule parallel to the nucleotide bases slips in between two adjacent base residues and in this manner increases the length of the helix, a process called intercalation by its discoverer, Lerman [204,205]. As will be made clear shortly, it is this process of intercalation which is of vital interest to the present study. As the dye-DNA ratio increases dimeric and polymeric dye aggregates stacked on the outside of the helix opposite to adjacent phosphate residues and perpendicular to the helical axis are found [169].

Intercalative Binding to DNA

It is well known [178] that planar dyes, such as the acridines or ethidium bromide, as well as the planar aromatic hydrocarbons, can bind to the intact DNA helix by intercalation between neighboring nucleotide base pairs. This is the strongest type of binding observed (about 8 to 10 kcal/mole for the aminoacridines) and is favored at low ratios of dye to DNA phosphates and at high salt concentrations. Intercalation as described by Lerman [204,205] refers to the ability of these molecules to bind to DNA by sliding between adjacent base pairs in the DNA helix. To accommodate an aminoacridine, for example, the DNA molecule must unwind slightly (18°), enabling the adjacent base pairs to separate just far enough (0.34 nm) to allow the aminoacridine molecule to fit in. The DNA molecule becomes longer and stiffer on binding an intercalating dye. As a result an increase in the viscosity of DNA solutions and a decrease in the rate at which DNA sediments in the ultracentrifuge are observed. These two effects on the hydrodynamic behavior of DNA are indicative of an intercalative process and have become important as diagnostic features of the intercalative process. A schematic representation of the Watson-Crick-Wilkins double helix of DNA with planar aromatic molecules intercalated between adjacent nucleotide base pairs is shown in Figure 23.

It is now clear that a large number of drugs and antibiotics utilize intercalation to bind to DNA [206]. Besides the aminoacridines, proflavine, and acridine yellow which act as potent frameshift mutagens, known

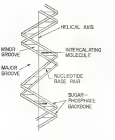

Figure 23. Schematic representation of the Watson Crick-Wilkins double helix of DNA with planar aromatic molecules intercalated between adjacent nucleotide base pairs. The outer helical strands represent the sugar-phosphate backbone, the horizontal lines represent the base pairs, and the vertical line is the helical axis. Representation is schematic only and extension and unwinding of the DNA helix due to intercalation is not indicated.

intercalating agents in this class include [206] the trypanocides, ethidium and propidium bromides, antitumor antibiotics such as daunomycin, nogalomycin, and actinomycin (a particularly well characterized case in which the phenoxazone ring system intercalates [207]), the antimalarial drug chloroquine (recent results demonstrate that in chloroquine analogs ring intercalation or some other form of ring interaction appears to be essential to significantly inhibit the RNA polymerase reaction and also that there is a correlation between the length of the side chain and RNA polymerase inhibition [208]), hycanthone (a possible hydroxylated metabolite of the antischistosomite Miracil D), and possibly the steroidal diamine, irehdiamine A. Ohnishi and McConnell [209] have demonstrated that the radical cation of the phenothiazine neuroleptic chlorpromazine binds to DNA *via* intercalation. This result forms the basis of the present study and will be discussed in more detail later.

Von Hippel and McGhee [178] report that no base specificity has been observed for the intercalation reaction, at least for ethidium bromide [210], proflavine [211], and acriflavine [212]. Reports that acridine orange and proflavine preferentially stabilize dA-T-rich DNA molecules against thermal denaturation [213] could conceivably be due to a decrease in the dye-DNA binding constant with increasing temperature [178]. However, the problem is by no means a simple one. In many cases the ability of dyes to interact with nucleic acids appears to depend primarily on the conformation of the specific polynucleotide structures involved rather than the chemical structures of the constituent nucleotides [214]. On this basis Aktipis and Martz [214] quote Wells [215] in saying that the preferential binding of actinomycin to DNA of high (G + C) content may be attributed to a specific conformation characteristic to this type of DNA rather than to any binding specificity of the dye toward either guanine or the G-C pair. The nature of the mode of binding of actinomycin, a cyclic-polypeptide-containing antibiotic, to DNA has now been very thoroughly characterized and the major features of the binding are as follows [207]: (a) the intercalation of the phenoxazone ring system on actinomycin between G-C sequences in DNA, (b) the hydrogen-bonding interaction between the peptide chain and the nucleic acid, the peptide portion of the actinomycin molecule lying in the minor groove of the DNA helix and being hydrogen bonded to deoxyguanosines on opposite DNA strands, and (c) the twofold axis of symmetry relating pentapeptide chains on the actinomycin molecule coinciding with the twofold axis of symmetry on DNA. The most dramatic and fundamental prediction of the three-dimensional model of actinomycin-DNA binding is that actinomycin should preferentially bind alternating G-C base sequences in DNA. Here is a case then where the binding mechanism depends intimately upon the structure of the intercalating molecule and the nucleotide base sequence. The necessity of the amino group in the purine 2-position is a clear indication of base specificity in this case.

Recent studies by Gabbay and coworkers [216,217] have also clearly shown that there is more than one type of intercalating site available in DNA and that specific base recognition can influence an intercalative mode of binding. As a result of the Watson-Crick-Wilkins double helical structure of DNA with A-T and G-C nucleotide base pairs, it can be shown [216] that there are ten distinctly different sites available on the DNA helix to intercalating molecules. There are three sites with A-T base pairs only, three sites with G-C base pairs only, and four sites with both A-T and G-C pairs. It is theoretically feasible then for a given intercalating agent to have different affinities for each of the ten possible binding sites. Gabbay, DeStefano, and Sanford [216] examined the interaction of four intercalating "reporter" molecules of the type

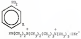
NO_2
R
$HN(CH_2)_2\overset{+}{N}(CH_3)_2(CH_2)_3\overset{+}{N}(CH_3)_3 \cdot 2Br^-$

with $-NO_2$, $-CN$, $-CH_3$, and $-CF_3$ as R-substituents with salmon sperm DNA using binding, optical absorption, and circular dichroism (CD) studies. The data [216] indicated that the trifluoromethyl substituent is more selective for specific intercalating sites than the other three substituents. The presence of nonequivalent intercalation sites in DNA may be of great importance in the recognition processes involved in protein interactions with nucleic acids [216]. Although simple electrostatic and hydrogen-bonding interactions with DNA cannot by themselves be very selective, in combination with selective binding such as the intercalation of protein aromatic residues, DNA sequence may well be recognized [216]. The "bookmark" hypothesis of Brown [218] is thus quite reasonable, especially if the "bookmarks" (protein aromatic residues) could also recognize the "book pages" or sites of intercalation [216]. Gabbay and coworkers [217] extended their work in an effort to define the three-dimensional size of the ten intercalation sites possible on the DNA molecule. The intercalation sites were probed with eight different reporter molecules, namely substituted N-methylphenanthrolinium cations of the following type where substitution of $-H$, $-CH_3$, and $-C_6H_5$ moieties in various combinations at the R-positions provided a variety of probe sizes. The interactions between nucleic acids of different base composition [*M. luteus* DNA (28

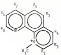

percent A-T), salmon sperm DNA (58 percent A-T), calf thymus DNA (56 percent A-T), and poly (dA-T)·poly (dA-T) with a 100 percent A-T content] and the aromatic N-methylphenanthrolinium cations were studied by melting temperature (T_m), nuclear magnetic resonance (NMR), UV absorption, induced CD, equilibrium dialysis, and viscometric techniques. Intercalation of the planar cations was indicated by total broadening of the proton NMR spectrum, increased viscosity, induced CD, and extensive stabilization of the DNA helix toward denaturation. Selective interactions with DNA were observed as a function of the number and position of R-substituents on the aromatic ring. The more highly substituted systems exhibited higher affinity, greater stabilization, higher viscosity, and enhanced binding to G-C and/or a combined G-C/A-T intercalation site. From these results Gabbay and coworkers [217] concluded that adjacent nucleotide base pairs may separate by distances greater than 0.68 nm in order to accommodate a bulkier intercalating cation. For example, with $R_3 = R_5 = R_6 = R_8 = -CH_3$, a separation distance of at least 0.76 nm is required for intercalation to occur. A novel model is proposed in explaining the viscometric data in that a nonuniform thickness of the substituted aromatic system will not only lead to a lengthening of the DNA helix upon intercalation but will also cause a slight bending of the helix at the point of intercalation [217].

The phenomenon of intercalation is evidently of major importance in the study of modes of binding of molecular species to the DNA helix. The examples cited above amply illustrate the nature of the binding and the work being done at present in elucidating the process. A thorough understanding of the intercalative process should lead to a more complete explanation of some of the most elegant of molecular biological processes underlying the fundamental mechanisms of living organisms.

Drug-Macromolecular Interactions

Considerable evidence now exists to suggest that drugs combine or interact with macromolecules throughout all phases of their action *in vivo* [218]. Neuroleptic agents which interact with biological macromolecules vary from those that bind weakly, such as meprobamate, to those which combine with a high affinity to a large number of macromolecules, such as the phenothiazines and imipramine [219]. Numerous studies [219] have shown that the phenothiazines interact with serum proteins, drug-binding protein of electric eel, nerve tissue components, casein, egg albumin, wool protein (a model for nerve receptors), a large number of enzymes, components of many membranes (particularly those present in nerves, muscles and junctions), polysaccharides, lipids, and melanin. Hole [220] found that various substituted phenothiazines form insoluble complexes with nucleic acids, particularly near pH 5, the interaction apparently involving the negatively charged phosphate groups of the nucleic acid and positively charged side chain of the phenothiazines. Magnesium is very efficient in suppressing complex formation, whereas Li^+, Na^+, and K^+ can either promote or depress complex formation.

The interaction of the radical cation of chlorpromazine with DNA is of interest because it has been proposed that the radical cation may be responsible for the psychotropic activity of the drug [221]. A number of *in vitro* experiments have indicated that interactions of the phenothiazine radical species occur not only with DNA [209] but also with NADH (reduced nicotinamide adenine dinucleotide), melanin, and enzymes [125]. On the other hand, it is known that numerous phenothiazine analogs that are very poor electron donors also exhibit potent neuroleptic activity. For instance, the dihydroanthracenes would require a highly energetic process in order to lose an electron and their radicals, if generated, would be much less stable than those derived from the phenothiazines [136].

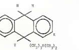

9,10-Dihydroanthracene derivative

The present study is an extension of the work of Ohnishi and McConnell [209]. The intercalative interaction of the CPZ radical cation with DNA (as studied by Ohnishi and McConnell [209]), as well as that for two other phenothiazines, triflupromazine (TFP) and methotrimeprazine (MMP), is examined in the present study in an effort to not only elucidate the interaction with DNA of these three phenothiazine drugs but also to develop a simple technique whereby electron spin resonance can be used to study the interaction of aromatic radicals with macromolecules.

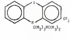

Triflupromazine

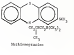

Methiomeprazine

CHAPTER VII

EXPERIMENTAL: INTERACTION OF PHENOTHIAZINE DRUGS WITH NUCLEIC ACIDS

Experimentally this work concerns the study of the interaction of radical cations of phenothiazine drugs with nucleic acids. A Sage Model 355 syringe pump is used to flow solutions of the drug-nucleic-acid complexes through the resonance cavity of a Varian E-3 ESR spectrometer (9.5-GHz microwave bridge, 100-kHz modulation). Analysis of the ESR spectra of the complexed drug radical cations permits conclusions to be made about the nature of the binding in the complex. For purposes of presentation it is convenient to divide discussion of the experimental aspects into two sections. The present discussion will be concerned with general experimental aspects, such as source of materials, procedures for sample preparation, and so forth, while a detailed discussion of the flow system will be presented in Chapter VIII.

Materials

Reagents

Chlorpromazine hydrochloride and triflupromazine hydrochloride were obtained from Smith Kline & French Research Laboratories. Methiomeprazine hydrochloride was obtained from Rhône-Poulenc. Salmon sperm DNA (SS-DNA) and calf thymus DNA (CT-DNA) were obtained from Worthington Biochemical Corporation. Potassium persulfate ($K_2S_2O_8$) analytical grade reagent was obtained from Mallinckrodt Chemical Works. Fremy's salt (potassium nitrosodisulfonate, $K_2[(SO_3)_2NO]$) was obtained from K & K Laboratories and anhydrous sodium carbonate (Na_2CO_3) was obtained from Fisher Scientific Company. The g-factor standard 2,2-diphenyl-1-picrylhydrazyl (DPPH) was obtained from Eastman Organic Chemicals. All reagents were used without further purification. DNA samples were kept frozen prior to use and the phenothiazine drugs were stored under refrigeration at 4°C.

ESR and Flow System Apparatus

ESR aqueous solution sample cells were obtained from James F. Scanlon Co. These cells have an all fused construction and are fabricated from high-purity Amersil quartz. The flat cell dimensions are: 60 mm long, 10 mm wide, 0.25 mm lateral depth. Overall length of the cell is 205 mm with a 7/25 outer joint at the top and a 5/20 joint at the bottom with a Teflon stopper.

Syringes used with the Sage Model 355 syringe pump were all ground glass and the following sizes were used: 0.25, 0.50, 1.0, 3,5,10,20,30, and 50 cc. Syringes were B-D Multifit, B-D Yale, Cyanamid Surgical Products Division VIM, or Surgical Supply Corporation Hypo Interchangeable. Hypodermic needles used in conjunction with these syringes were 20 and 21 gage, 1 1/2-inch 12's, reusable locking type hypodermic needles from Propper Mfg. Co. and 25 gage, 1/4-inch 12's from Hypo Surgical Supply Corporation. Also occasionally used were Perry blood collecting needles, 20 gage, 1 1/2-inch, manufactured by MPL, Inc. All needles were stainless steel.

ESR aqueous solution flow cell frames (see Chapter VIII for details) were made from Teflon supplied by the Machine-Instrument Shop, Department of Chemistry, University of Florida, Gainesville, Florida. Capillary tubing for the flow cells was obtained from Electronic Wholesalers, Inc.

(0.0250 inch I.D., 0.0500 inch O.D.), or with Hamilton Teflon needles. The Hamilton Teflon tubing comes equipped with Kel-F hubs, which can be used rather than a hypodermic needle to connect the tubing to a syringe. Unfortunately, the Kel-F hubs could not be used with the flow system because fluid pressure collapsed the tubing flange between hub and syringe, thereby retarding or completely blocking solution flow. Hamilton Teflon needles used were KF30TF (nominal I.D. 0.013 inch, wall thickness 0.009 inch, wall tolerance ±0.002 inch), KF22TF (nominal I.D. 0.027 inch, wall thickness 0.009 inch, wall tolerance ±0.002 inch), KF20TF (nominal I.D. 0.034 inch, wall thickness 0.012 inch, wall tolerance ±0.003 inch), and KF19TF (nominal I.D. 0.038 inch, wall thickness 0.012 inch, wall tolerance ±0.003 inch). Tubing used to construct a DPPH probe (see Chapter VIII for details) was polyethylene intravenous tubing (0.023 inch I.D., 0.038 inch O.D.) obtained from Aloe Medical. Samples were collected in Fisher 10-cc graduated test tubes after passage through the Varian E-3 microwave cavity.

Methods of Preparation

DNA Solutions

Stock solutions of SS-DNA or CT-DNA with a DNA concentration of approximately 2.5 mg/ml were prepared by adding an appropriate quantity of DNA to the desired volume (usually 25-50 ml) of distilled water. Gentle overnight stirring with a Teflon magnetic stirring bar was sufficient to bring the polymer into solution. Stock solutions were stored under refrigeration at 4°C except during use. DNA concentrations were determined spectrophotometrically using either a Cary-15 UV spectrometer or a Beckman Acta CIII spectrophotometer. Samples were prepared for this determination by diluting a 0.2 ml portion of DNA stock solution to 10 ml with 0.1 M 2-(N-morpholino)ethanesulfonic acid (MES) buffer (0.05 M Na^+, pH 6.2), a gift from Dr. E.J. Gabbay (Department of Chemistry, University of Florida, Gainesville, Florida). The absorbance was measured at 257 nm using matched quartz cells (1-cm path length), the blank being the MES buffer. Concentrations were readily determined from the Beer-Lambert relation using ε(P) = 6500 l/mol/cm for SS-DNA [222] and ε(P) = 6600 l/mol/cm for CT-DNA [169], where ε(P) is the molar extinction coefficient of DNA on a mononucleotide (phosphorous) basis. DNA stock solutions typically had a concentration of nucleotide base pairs of 0.003 to 0.004 M.

Phenothiazine Drug Radical Cations

The radical cations of chlorpromazine (CPZ), triflupromazine (TFP), and methiomeprazine (MMP) were prepared by oxidation with potassium persulfate following the procedure of Borg and Cotzias [223-225]. Persulfate quantitatively oxidizes the drugs to the radical cation form [223-225]. Details of the preparation of the CPZ radical cation are given as an illustrative example. A 0.02 M solution of CPZ was prepared by dissolving 0.03553 g of CPZ hydrochloride in 5 ml of distilled water. A 0.01 M solution of $K_2S_2O_8$ was prepared by dissolving 0.02703 g of $K_2S_2O_8$ in 10 ml of distilled water. Aliquots of these two stock solutions were mixed so that the resulting concentration of CPZ was 0.01 M and that of the persulfate anion, $S_2O_8^{=}$, was 0.005 M. As the two colorless solutions of reactants were mixed, there was an initial white clouding of the solution, followed within several seconds by deepening red coloration. Following several minutes of swirling the solution in the reaction flask, chromogenesis ceased and the red solution became transparent. The redox reaction occurring can be represented by the equation $2CPZ + S_2O_8^{=} \rightarrow 2CPZ\cdot^{+} + 2SO_4^{=}$. Use of the radical cation thus formed was prompt since the radical decays over a period of a few hours, as indicated by increasing decoloration of the solution with the passage of time. Similar observations are obtained when preparing TFP and MMP radical cations by persulfate oxidation except that the color of the resulting transparent solution is golden brown for TFP radical cations and blue for MMP.

Drug-DNA Complexes

Drug-DNA complexes were prepared by adding freshly formed solutions of radical cation to stock solutions of SS-DNA or CT-DNA such that the nucleotide base pair to radical cation ratio (BP/R) was approximately 5 after the procedure of Ohnishi and McConnell [209]. The solution pH in all cases was 5.0 - 5.4, as measured with a Beckman Zeromatic II pH meter. DNA stock solutions typically had a pH of about 6.8, CPZ hydrochloride stock solutions (0.02 M) of pH of 5.1, and $K_2S_2O_8$ stock solutions (0.01 M) a pH of 4.7. In all cases the radical cations of CPZ, TFP, and MMP were found to be markedly stabilized by the presence of DNA (see Chapter IX). This is in accord with the results of Ohnishi and McConnell [209]. The coloration characteristic of a given radical cation persisted in its DNA complex and several minutes of gentle swirling usually sufficed to thoroughly mix drug and DNA. Spin resonance experiments were performed immediately after preparation of the drug-DNA complexes. Solutions of complexes were usually stored under refrigeration at 4°C after initial use and could be used repeatedly thereafter for several weeks without appreciable differences appearing in the ESR spectra obtained.

The stability of the phenothiazine radical cations is strongly dependent on pH. It is well known that the radicals are stable in acid media and, indeed, can readily be generated by oxidation in concentrated hydrochloric or sulfuric acid [223-227]. Piette, Bulow, and Yamazaki [221] used ESR spectroscopy in studying the CPZ radical cation formed during enzymic oxidation by peroxidase-hydrogen peroxide. They noted the stability of the CPZ radical cation near pH 5 and found that as the pH increases the radical becomes more unstable. Close to neutral pH the decay of the CPZ radical is so fast that the steady-state free radical accumulation is observed in less than a few seconds after the reaction starts [221]. In the present experiments it was of interest to know if the drug-DNA complexes were also this sensitive to pH. Attempts to prepare the CPZ, TFP, and MMP radical cations in buffered media (0.1 M MES buffer, 0.05 M Na^+, pH 6.2, Brenk buffer, pH 6.8, a blended mixture of monobasic potassium phosphate and dibasic sodium phosphate, obtained from Aloe Scientific) were unsuccessful. Addition of unbuffered solutions of radical cations to buffered stock solutions of DNA was also attempted. The characteristic coloration of the drug-DNA complexes was evident upon initial addition of the radical solutions, however, the coloration faded rapidly and the solutions were completely colorless and transparent within an hour. Consequently, no buffers were used in preparing the drug-DNA complexes.

Fremy's Salt

Fremy's salt (potassium nitrosodisulfonate, $K_2[(SO_3)_2NO]$) dissolved in saturated Na_2CO_3 solution forms the radical dianion $(SO_3)_2NO^=$ with three hyperfine components separated by 13.00 ± 0.07 G and g = 2.0057 ± 0.0001; moreover, for field scan widths up to 100 G Fremy's salt is useful for calibrating the magnet scan [38,40,76,228-232].

A 0.01 M solution of Fremy's salt was prepared by dissolving 0.2683 g of Fremy's salt in 100 ml of saturated Na_2CO_3 solution. The clear solution immediately turned light purple and became transparent upon swirling. The solution may be stored under refrigeration for several months but decays if stored at room temperature. A portion of the freshly prepared solution was transferred to the quartz ESR aqueous sample cell for calibration of the Varian E-3 magnet scan. The solution was also used in some initial tests with the Teflon flow cells to determine their suitability for spin resonance measurements.

The three lines in the ESR spectrum of Fremy's salt (due to hyperfine splitting from the ^{14}N nucleus) are not equally spaced because of second-order effects. If the center line is taken as zero field, the field positions (at X-band) are -13.118 G, 0.000 G, and +13.064 G. The position of the center line relative to the two outer lines depends on the microwave frequency, however, the separation of the two outer lines is always 26.182 G. Results of scans of the Fremy's salt spectrum with the Varian E-3 ESR spectrometer showed that the error in gauss per chart paper division amounts to less than 2 percent.

CHAPTER VIII

THE EXPERIMENTAL FLOW SYSTEM FOR STUDY OF PHENOTHIAZINE DRUG RADICAL COMPLEXES WITH DEOXYRIBONUCLEIC ACID

In order to perform ESR experiments to study possible intercalation of phenothiazine drug derivative radical cations with helical nucleic acids in a fashion similar to that of Ohnishi and McConnell [209], it is necessary that the drug-DNA solution be flowed through a sample cell system in the resonance cavity. Two types of flow are required. First, the sample solution must be flowed in a direction perpendicular to the direction of the applied magnetic field, and, secondly, in a direction parallel to the applied field. Since the longitudinal axis of any type of sample cell inserted into the Varian E-3 ESR microwave cavity is perpendicular to the applied field, the problem of flowing a solution perpendicular to the applied field is of no consequence. Ohnishi and McConnell [209] flowed solutions of DNA and CPZ through capillary tubing in the resonance cavity of a Varian 35-GHZ spectrometer. Use of capillary tubing was thus indicated in the present work. However, the parallel flow situation presents some difficulties in design. Ideally parallel flow could be obtained by inserting capillary tubing through holes in the sides of the cavity positioned such that the section of capillary tubing within the cavity is parallel to the applied field. Access through the sides of the Varian E-3 cavity was considered impractical for several reasons. Location of the modulation coils within the sides of the cavity would mean careful construction of a new cavity so that the performance of the cavity would not be altered. Since the available Varian E-3 ESR spectrometer was in general use for anyone who required its capabilities, the inconvenience of either building a new cavity (or modifying the existing one) was not feasible. Furthermore, the gap between the magnet pole faces is sufficiently small that with the cavity positioned between them there is virtually no working space to accommodate attachments through the sides of the cavity. Thus some method of cell construction that allows parallel flow to be obtained within the confines of the E-3 microwave cavity, but which is itself inserted vertically in the normal fashion without disruption of the ESR instrument, was desirable. The design of such a cell system is limited by the fact that the dimensions must be made to conform as nearly as possible to those of the quartz aqueous sample cell. This crucial experimental aspect will be treated in more detail in the following discussion.

Cavity and Sample System Considerations

General Considerations

The essential requirements [38-40,44,71,76,77] for the cavity and sample system will be discussed briefly. The microwave cavity of an ESR spectrometer amplifies the intensity of microwaves in a fashion analogous to the way an organ pipe amplifies sound waves. When the microwave frequency is such that one of the dimensions of the cavity are multiples of half-wavelengths, the microwave intensity is magnified, the lowest frequency at which this occurs being termed the cavity resonant frequency. As discussed previously in Chapter I, electromagnetic radiation consists of two mutually orthogonal fields, an electric field ($\bar{E}_1$) and a magnetic field ($\bar{H}_1$). Optimum ESR absorption signals are provided by cavities which (1) yield a high microwave density, (2) have $\bar{H}_1$ perpendicular to the applied field $\bar{H}$, which is one of the conditions required for spin transitions to be "allowed," and (3) allow sample positioning at a maximum of $\bar{H}_1$ and a minimum of $\bar{E}_1$, a condition following from the resonance requirement of interaction with the magnetic field (see Chapter I) and because interaction with the electric field gives rise to nonresonant dielectric loss of power. Most commercial ESR spectrometers like the Varian E-3 use rectangular cavities such as the TE_{102} rectangular cavity represented schematically in Figure 24. The TE designation means "transverse electric," that is, the $\bar{E}_1$ field is always oscillating perpendicular to the longitudinal axis of the cavity (the z axis in Figure 24), while the subscripts refer to the number of half-wavelengths along the x, y, and z axes. Also indicated in Figure 24 are the spatial distributions of the $\bar{E}_1$ and $\bar{H}_1$ fields in the cavity. From Figure 24 it is seen that positioning of the sample along the x axis places it in a region of maximum $\bar{H}_1$ and minimum $\bar{E}_1$.

The "sharpness" of the response of any resonant system may be described by a factor of merit, Q, which for an ESR resonant cavity may be defined as

$$Q = \frac{2\pi(\text{maximum microwave energy stored in cavity})}{(\text{energy dissipated per cycle})} \qquad (93)$$

Energy storage and Q generally increase with cavity volume for a fixed frequency. Equation (93) also implies that an increase in Q arises from decreasing energy losses from currents flowing in the cavity walls or sample. The cavity Q will be lowered if a sample having a high dielectric constant (such as water) extends into regions of appreciable $\bar{E}_1$. When Q is lowered, the spectrometer sensitivity is also lowered. Since below saturation the amount of energy absorbed by the sample is proportional

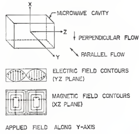

Figure 24 Schematic representation of a rectangular parallelpiped TE_{102} microwave cavity illustrating both electric and magnetic field contours within the cavity. The directions of parallel and perpendicular flow of sample solution through the cavity are indicated with respect to the fields within the cavity.

to E_1^2, placing the sample at a position of maximum $\overline{E}_1$ enhances the signal to noise ratio. Since dielectric power loss has a deleterious effect on the signal to noise ratio, placing the sample at a position of minimum $\overline{E}_1$ is also clearly desirable. Q's of the order 5000 to 10,000 are typically found for rectangular cavities used at X-band frequencies.

The value of Q under the condition that only losses within the cavity are considered, that is, resistive losses in the walls, is called the unloaded Q-factor, Q_U. However, a cavity must be coupled by a small hole (iris) to the waveguide (microwave plumbing) system carrying microwaves from the generating source (klystron tube). Because this coupling entails additional losses, there is a further lowering of Q, the loss being measured by

$$Q_R = \frac{2\pi(\text{maximum microwave energy stored in cavity})}{(\text{energy lost through coupling holes per cycle})} , \quad (94)$$

The ratio $\beta = Q_U/Q_R$ is called the coupling parameter and equals unity for optimal coupling, that is, maximal transmission of power into the cavity. The overall or loaded quality factor Q_L is then defined by

$$(Q_L)^{-1} = (Q_R)^{-1} + (Q_U)^{-1} \quad (95)$$

Thus, when $\beta = 1$, $Q_L = \frac{1}{2} Q_U$. If there are materials within the cavity having a nonvanishing imaginary part of the dielectric constant, additional losses can occur. To account for these losses, the dielectric Q-factor, Q_ε, is defined as

$$Q_\varepsilon = \frac{2\pi(\text{maximum microwave energy stored in cavity})}{(\text{energy lost per cycle in dielectric loss})} \quad (96)$$

A factor Q_U' is defined such that

$$(Q_U')^{-1} = (Q_\varepsilon)^{-1} + (Q_U)^{-1} \quad (97)$$

Q_U' is the factor which should be used in sensitivity calculations.

If a cavity has originally been designed and constructed for a high Q, then most of the dielectric losses usually occur within the sample or sample cell. The principal effect of the presence of the sample on Q is the extent to which the sample interacts with the $\bar{E}_1$ field. Such interaction forms the basis of operation of microwave cooking ovens, for example. Sample interaction with $\bar{E}_1$ increases with the dielectric constant of the sample, increasing geometrically to the extent that the sample extends into the region of nonzero electric field (see Figure 24). Thus, it is important to position the sample in a region of the cavity for which the microwave electric field is a minimum.

Positioning is extremely critical for aqueous samples, which exhibit a high dielectric loss. X-band microwaves are readily absorbed by polar substances such as liquid water, the interaction being between the $\bar{E}_1$ field and free polar groups such as the OH portion of the water molecule. This nonresonant absorption process is very efficient and significant amounts of water, even 0.1 ml or less, will effectively absorb all of the incident microwave radiation, thus reducing ESR sensitivity so severely that spin resonance measurements cannot be made. The most satisfactory container for aqueous samples is a flat, high-purity silica cell which can be accurately oriented by means of adjustment screws along the nodal plane of the $\bar{E}_1$ field. It is found that optimum sensitivity occurs when $Q_U = Q_{\varepsilon}$, that is, for a reduction of Q_L to one-half of its value in the absence of dielectric loss. For aqueous solutions this requires that the silica plates be separated by about 3 mm for X-band frequencies. Capillary tubes can also be used but these do have the disadvantage of small sample size and poor sample configuration if concurrent light irradiation is to be used.

The sample container (cell) can also affect ESR sensitivity, principally by its own interaction with $\bar{E}_1$. Most glass and silica materials give strong ESR signals and are not suitable as sample cell materials. Fused silica quartz of high purity avoids these difficulties. This material is also advantageous since it has a very low dielectric loss and hence is a desirable material for the fabrication of Dewar inserts. Quartz usually concentrates the magnetic field so that the result is an increase in effective microwave power at the sample. For nonsaturating samples, an appreciable increase in signal magnitude can result. Clearly it is important to compare samples in the same or equivalent cells

Design of Flow Cells

From the foregoing considerations it is evident that aqueous sample flow cells for use with the rectangular cavity of the Varian E-3 ESR spectrometer should be modeled after the flat quartz aqueous sample cell. Considerable reflection on the problem indicated that for ease of construction, utility of operation, and reasonable fabrication expense and effort Teflon capillary tubing would be a suitable material since, like quartz, it has a low dielectric loss and is a suitably inert material for use with aqueous samples. Since this tubing is very flexible, it can be readily molded into any desired configuration by constructing a suitable rigid framework, also made of Teflon. To maintain all experimental parameters as nearly identical as possible, it was decided that, even though a perpendicular flow arrangement could easily be achieved by use of a quartz capillary tube, the perpendicular flow arrangement would be constructed entirely of Teflon, as would necessarily be the parallel flow arrangement.

Schematic diagrams of the Teflon cell frames designed and constructed for use with the Varian E-3 instrument are shown in Figure 25 for perpendicular flow and Figure 26 for parallel flow. Detailed discussions of the flow cells will be presented in a later section, but the basic design features are as follows. The Teflon cell frames are modeled in both shape and dimension after the quartz aqueous sample cell. There is a central flat portion of the cell with cylindrical extensions on either side to fit into the aqueous sample cell holders used with the Varian E-3 cavity. The flat section of the frame is then constructed to accommodate the desired configuration of Teflon capillary tubing for either parallel or perpendicular flow in such a manner that the capillary tubing will be in a position of maximum $\bar{H}_1$ and minimum $\bar{E}_1$ within the resonant cavity. Clearly construction of a Teflon framework rigid enough to maintain its configuration and also accommodate capillary tubing will mean that the depth of the flat portion of the cell will be somewhat in excess of that of the quartz flat cell. This means that more of the cell, if not the sample, will extend into regions of strictly nonzero $\bar{E}_1$ field for the Teflon flow cells as compared to the quartz cell. However, in the final analysis it was found that this did not alter the sensitivity of the instrument appreciably, the tuning characteristics of the cavity and the quality of ESR spectra obtained being essentially equivalent for the flat quartz cell and the Teflon cells, particularly in the cases where the total volumes of sample within the cavity were reasonably comparable.

The Teflon perpendicular flow cell (Figure 25) consists essentially of two separate sections which, when fitted together, provide a narrow rectangular slot through the length of the flat portion which can accommodate one or several Teflon capillary tubes in a plane parallel to the applied field. This means that flow through this tube, or tubes,

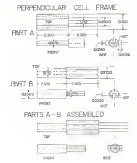

Figure 25 Schematic diagram of Teflon cell frame for perpendicular flow through the Varian E-3 microwave cavity. All dimensions are in inches. Types of capillary tubing used with this cell frame are discussed in the text.

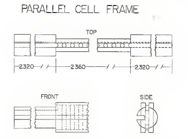

Figure 26 Schematic diagram of Teflon cell frame for parallel flow through the Varian E-3 microwave cavity. All dimensions are in inches. Dimensions other than those shown vary with the size of capillary tubing used, as discussed in the text.

will be in a direction perpendicular to the applied magnetic field while the tube, or tubes, will be in a nodal plane of the $\vec{E}_1$ field and in the plane of maximum $\vec{H}_1$. In other words, the perpendicular flow cell frame merely provides a rigid framework for a flexible Teflon capillary tube positioned vertically in the Varian E-3 resonant cavity.

The Teflon parallel flow cell (Figure 26) has a flat section containing evenly spaced cylindrical holes parallel to one another and the applied magnetic field direction and lying in a vertical plane parallel to the applied magnetic field. This means that the plane of the holes can be positioned in the nodal plane of the $\vec{E}_1$ field and at a position of maximum $\vec{H}_1$ field. Flexible Teflon capillary tubing is then threaded through the flat section of the cell in a coiled configuration which will be in the plane of the flat section of the cell. The configuration of the Teflon capillary tubing thus looks like

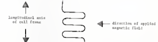
longitudinal axis of cell frame
direction of applied magnetic field

and it is clear that solution flowing through the coil will be in a direction parallel to the applied magnetic field (except for the loops of the coil). Thus, although such a coiled configuration does not permit total flow within the cavity in a direction parallel to the applied field, it does permit substantial parallel flow in a cell arrangement which is readily constructed, does not involve alterations in the Varian E-3 resonant cavity, and which can be inserted into the cavity and positioned in the same manner as the standard flat quartz aqueous solution sample cell. Since the loops of the coiled configuration give rise to flow that is not parallel to the applied field direction, the effects of parallel flow on the observed ESR spectra will be tainted by an amount of randomly oriented flow, the effect of which depends on the construction of the cell and the size of capillary tubing used.

The preceding discussion has focused on the general features of the Teflon flow cells. Detailed analysis of the results obtained and their dependence upon the geometry of the cell, as well as other parameters, will be presented in a later section.

g-Factor Measurement

The absolute measurement of a g-factor requires knowledge of the microwave frequency and the resonant magnetic field. A number of systematic errors can enter [233] and in practice absolute measurements are rarely attempted. The method of choice is to use standards for which the g-factors are well known. The unknown g-factor, g_x, is then calculated from the relation $g_x = g_s H_s/H_x = g_s H_s/(H_s - \Delta H) \cong g_s(1 + \Delta H/H_s)$, where g_s is the g-factor of the standard, H_s is the resonant magnetic field of the standard, H_x is the resonant magnetic field of the unknown, and $\Delta H = H_s - H_x$. If the g-factors of the standard and the sample do not appreciably differ from one another, then ΔH will be small compared with H_s and accurate results will depend only on an accurate measurement of ΔH. The above relations cannot be used when g-factors deviate considerably from that of the standard. In this case either a g-factor standard with a g-factor close to that of the unknown should be used or both the microwave frequency and magnetic field should be measured. For solid DPPH, a commonly used g factor standard, $g = 2.0037 \pm 0.0002$ [234,235]

In order to measure g-factors of the drug-DNA complexes the Teflon parallel and perpendicular flow cell frames were designed to accommodate a DPPH probe. The DPPH probe was constructed by enclosing a tiny crystal of solid DPPH in a length (about 4 inches) of polyethylene intravenous tubing. A schematic representation of the probe is shown in Figure 27. One end of the polyethylene tubing is sealed with a small Teflon plug (approximately 1/2 inch in length) made by extruding Teflon from a 20-gage hypodermic syringe needle forced through a suitably sized Teflon block. This forms the lower end of the probe and, in the vertical position within the resonant cavity, the DPPH crystal rests on the Teflon plug. The polyethylene tubing containing the DPPH sample is inserted into the flow cell by threading it through a length of Hamilton KF20YF Teflon needle attached to the cell frame. In the case of the perpendicular flow cell, the support tubing for the DPPH probe is simply included as one of the tubes through the rectangular slot in the flat portion of the cell. When in position the DPPH crystal lies approximately in the center of the flat section in the same plane as the sample tubes. Thus the DPPH crystal enjoys the same microwave environment as the aqueous sample. The size of the DPPH crystal is so small that its insertion into a cavity previously tuned to an aqueous sample does not require retuning the cavity. The corresponding modification to the parallel flow cell consists of milling a slot (see Figures 26 and 27) across the face of the flat cell surface to accommodate the Hamilton Teflon support tubing. The slot is milled as close as possible to the configuration of cylindrical holes without entering them or distorting material into them. When the probe is in position, the DPPH crystal is again approximately at the center of the flat section of the cell. Although the design of the flat section of the parallel cell necessitates this type of positioning of

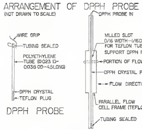

Figure 27. Details of DPPH probe used with parallel and perpendicular flow cells to allow g-factor determinations. All dimensions in inches. Diagram on the right illustrates the manner in which probe is used with parallel flow cells as discussed in text.

the DPPH probe in which the DPPH crystal is not exactly in the same plane as the sample tubes, use of the probe does not affect the tuning of the cavity, as evidenced by negligible drift in the frequency error meter of the Varian E-3 microwave bridge upon insertion of the probe.

The choice of this method of measurement of g-factors was decided upon because use of any form of internal g-factor standard in the present work is rather impractical. The experimental procedure used was to run the spectrum of the sample and then insert the DPPH probe and immediately record the DPPH spectrum (superimposed on the sample spectrum) under the same instrumental conditions (except for lower gain to maintain the DPPH resonance on scale). Experience with the system, as well as comparison of the present results to previously published work [209], indicates that use of the DPPH probe with the Teflon flow cells is a reliable way to measure g-factors in these experiments.

The g-factors for the DNA-bound drug radicals were then determined by comparison with the DPPH standard by using the relation $g_{drug} = g_{DPPH}H_{DPPH}/H_{drug}$. For $g_{\perp}$ the field position is measured from the perpendicular flow spectrum and is taken as the point where the derivative curve crosses the base line. In the case of $g_{||}$ the field is measured by taking the field position corresponding to the midpoint between the two outer lines of the parallel flow spectrum. These lines correspond to the outer lines of the parallel triplet. This is believed to be a more accurate representation than just measuring the field position of the central peak in the parallel flow spectrum because this peak lies on the perpendicular line and the perpendicular contribution is not judged to be negligible even in the case of parallel flow. It is also assumed that inequalities in the splitting of the parallel lines arising from second-order effects are negligible. The agreement of g-factors derived from the present work on CPZ complexes with CT-DNA with those of Ohnishi and McConnell [209] indicates that the present method is satisfactory. Since any errors inherent in the magnetic field positions cancel in the relation used to determine g_{drug}, the accuracy of the determination of $g_{||}$ and $g_{\perp}$ depends only on the accuracy of the value of g_{DPPH}. Therefore, the g-factors determined here are considered accurate to ±0.0002

The Flow System

The Pumping Arrangement

After careful consideration it was decided that a syringe pump would be the most feasible pumping system for flow of aqueous solutions through Teflon capillary tubing in the Varian E-3 resonant cavity. A syringe pump offers several advantages over other types of pumping systems. It is amenable to use of small sample volumes and pumping through very small orifices such as the Teflon capillary tubing of the flow cell. It provides pulse-free flow at a variety of rates and allows for convenient optimization of ESR instrumental parameters before scanning a flowing sample. In addition, such a system is light-weight and very convenient for portable use with the Varian E-3, requiring only a suitable support and relatively close proximity to the cavity. The syringe pump chosen was the Sage Model 355 syringe pump.

The Sage Model 355 syringe pump offers a continuously variable flow range with literally thousands of possible flow rates with any single size syringe [236]. The instrument is used in clinical, biological, and industrial laboratories to feed tissue cultures, infuse drugs at known rates, simulate reagent flow in pilot studies, and in a wide variety of other diverse applications. The syringe holder will hold any one syringe up to 100 cc size, any two syringes up to 50 cc, or any three up to 30 cc, with not more than two different syringe sizes being used at one time. Flow rates are set for only one syringe, the flow rates from other syringes then being proportional to their cross-sectional areas. There is a slip clutch to protect the drive carriage motor if the syringe jams or back pressure exceeds a set limit; however, when the back pressure falls to within the allowed limits, pumping action will resume.

To calculate the flow rate two instrumental controls must be considered. The range switch knob has four settings (X1, X1/10, X1/100, and X1/1000) and an "off" position. Switching from one flow setting to the next position will change the flow rate by a factor of 10. For instance, a flow rate of 20 cc/min at X1 will be 0.20 cc/min at X1/100. The percent-flow dial permits continuous variation of the flow rate in each range. The instrument dial is calibrated to have a minimum setting of 4 percent and a maximum setting of 104 percent although the 100 percent rate on the flow rate chart of the pump will read 0.00 on the flow dial.

To assure accurate flow rates with any brand syringe the following steps are taken, using an arbitrary flow rate of 2.0 cc/min for a time period of 15 minutes as an example.

(1) A syringe size is first selected. For the present example the total volume required is (2.0 cc/min)(15 min) = 30 cc. Thus a 30-cc (or any larger size) syringe is required.

(2) A flow range is selected from the chart provided on the instrument. For example, 100 percent flow at a range of X1 gives a rate of 57 cc/min for a 30-cc syringe and 4 percent at X1 gives 2.3 cc/min. Since a rate of 2.0 cc/min is required, the X1 range setting cannot be used. However, 100 percent at X1/10 gives 5.7 cc/min and 4 percent at X1/10 gives 0.23 cc/min and, therefore, the X1/10 range setting can be used

(3) The percent-flow reading is calculated as the desired rate divided by the 100 percent rate at the selected range. For the present example, then 2/5.7 = 35 percent. Thus, 35.0 is dialed on the percent-flow dial and the range switch set at X1/10 to infuse 2.0 cc/min for 15 minutes with a 30-cc syringe. For best reproducibility the manufacturer recommends not using percent-flow settings of less than 10 percent. By decreasing the range setting one position where possible, and multiplying the percent-flow by 10, good reproducibility at desired rates can be obtained.

The flow rates provided by the manufacturer are nominal because internal diameters vary in different syringes. However, as mentioned, any brand of syringe may be used. The calibration procedure consists of calculating the percent-flow and range settings as outlined in the above example and then, using these settings, accurately measuring the amount of infused fluid for a given unit of time with the desired syringe. The correct percent-flow reading is calculated from the following direct proportion:

$$\frac{\text{actual amount infused}}{\text{amount of expected fluid}} = \frac{\text{percent flow reading}}{\text{adjusted percent-flow}}$$

Experimental Procedure

A schematic representation of the flow system as used with the Varian E-3 ESR spectrometer is shown in Figure 28. The maximum flow rate possible for a given syringe size used with the Sage Model 355 syringe pump in conjunction with the Varian E-3 ESR spectrometer depends on the spectrometer scan time range: maximum flow rate (cc/min) = syringe volume (cc) divided by E-3 scan time (min). This relation can be used to estimate flow rates attainable for given syringe sizes and scan times. In practice

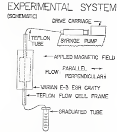

Figure 28. Schematic representation of flow system as used with the Varian E-3 ESR spectrometer, showing syringe pump, cell arrangement, microwave cavity, and collection tube.

accurate measurement of the volume flow rate is desirable for each scan. It is thus convenient to have some simple procedure for measuring the volume passed through the resonant cavity during the course of a spectral scan. The time required for passage of a certain volume of sample through the cavity was measured by utilizing the spectrometer recorder in the following way. The recorder is allowed to trace a path to just downfield from the field position at which absorption signals are expected or known to occur. The scan is stopped and a vertical line marked on the spectrum by moving the recorder zero-adjustment knob. Flow of the sample and continued scanning are then initiated simultaneously. This is done by moving the drive carriage back slightly from the syringe plunger before starting the syringe pump. As soon as the first drop of solution passes into the collection tube (indicating flow is established) the scan is started. Once the spectrum has been recorded, the syringe pump and spectrometer scan are shut off simultaneously and another vertical mark made on the chart paper. If the time it takes to scan over one recorder chart paper division is known for a given scan rate, then the time elapsed between the two vertical marks is readily calculated. Such data were determined for the Varian E-3 spectrometer and are given in Table XII. The data in Table XII represent the averages of no fewer than 10 determinations and reflect much less than 1 percent error. Thus having calculated the time elapsed to collect a certain volume of sample (as measured by collection in a graduated tube), the volume flow rate for any spectrum recorded can be determined.

Defining the average deviation, a_V, in terms of the average volume flow rate, $\langle V\rangle$, and individual volume flow rate measurements, V_i, as [237],

$$a_V = (1/N) \sum_i |V_i - \langle V\rangle| , \qquad (98)$$

TABLE XII

Varian E-3 ESR Spectrometer Scan Time Calibration Data for Use with Flow System

Scan Time Setting (min)	$\frac{\text{sec}}{\text{cm}}$
1	0.15
2	0.29
4	0.57
8	1.1

where N is the total number of measurements, and the percent-average deviation, A_V, as [237]

$$A_V = 100a_V/\langle V\rangle \ , \qquad (98)$$

data obtained from the present flow system for a variety of syringe sizes and percent-flow settings indicate that in no case is the percent-average deviation greater than 10 percent. Faster volume flow rates tended to have lower values of A_V than slower flow rates (3.6 percent for 100 percent flow versus 7.4 percent for 40 percent flow for a 1-cc syringe and a range setting of X1 in conjunction with the PA37B (abbreviation explained in a later section) flow cell, for example). Typical data are listed in Table XIII. In no instance were fewer than 10 measurements of the volume flow rate considered. It can also be shown from these data that within the limits of the average deviation as defined by Eq. (98) a linear relationship exists between volume flow rate and the percent-flow setting of the syringe pump.

In the absence of a fully automated and synchronized arrangement for measurement of volume flow rates, the method described is considered as satisfactory for the purposes of the present work since high precision in measurement of volume flow rates is not required. There are admittedly some disadvantages to the present method of volume flow rate measurement and the method itself readily gives rise to systematic errors, such as personal errors in reading the meniscus of the solution collected, and random errors, as in measuring the length between marks on the chart paper. Thorough minimization of random error, leading to high precision, and systematic errors, leading to high accuracy, would certainly require some type of automatic system to eliminate operator inconsistencies.

TABLE XIII

Variation in Measured Volume Flow Rates Using a 1-cc Syringe and PA373 Flow Cell for 90 Percent Flow and Range Setting X1

V_i(cc/sec)	$\lvert V_i - \langle V \rangle \rvert$
0.03714	0.00170
0.03897	0.00013
0.03718	0.00166
0.04178	0.00294
0.03938	0.00054
0.03647	0.00237
0.03747	0.00137
0.04307	0.00423
0.03829	0.00055
0.03860	0.00024

$\langle V \rangle = 0.03884$ cc/sec

$a_V = 0.00157$

$A_V = 4.0$ percent

Fluid Mechanical Considerations

Complete analysis of the flow system requires some treatment of fluid mechanical considerations [169, 238-243]. The fluid velocity for laminar flow in a capillary tube is maximal at the center and vanishes at the wall. At a distance r from the center of the capillary, the velocity v(r) in cm/sec is given by

$$v(r) = (P/4L\eta)(a^2 - r^2) , \qquad (100)$$

where P is the pressure differential between entrance and exit in dyne/cm^2, L is the capillary length in cm, η is the solution viscosity in poise, and a is the capillary radius in cm.

Laminar flow indicates a fluid flow which flows in laminae or layers, as opposed to turbulent flow in which the velocity components have random turbulent fluctuations imposed on their mean values. For instance, a stream of dye infused into a laminar flow will streak out a thin line and always be composed of the same fluid particles. However, in turbulent flow the dye line would rapidly become tangled up and mixed in with the fluid as it flows along, myriads of ever widening and dispersing threads and clouds being observed as the fluid flows along. A striking example of laminar flow is syrup being poured from a bottle. For a given fluid the velocity and channel configuration determine whether the flow is laminar or turbulent. Viscosity can be thought of as the internal friction of a fluid or as a measure of the fluid's resistance to shear when the fluid is in motion. Because of viscosity a force must be exerted to cause one layer of a fluid to slide past another, or to cause one surface to slide past another if a layer of fluid intervenes between the surfaces. Shear is defined as an internal force tangential to the section on which it acts or it may be thought of as an action or stress resulting from applied forces that causes two contiguous parts of a body to slide relatively to each other in a direction parallel to their plane of contact.

The volume flow rate, V in cc/sec, for laminar flow in a capillary is given by Poiseuille's Law as

$$V = P\pi a^4/8\eta L \tag{101}$$

The velocity $v(r)$ can be expressed as a function of the volume flow rate, that is,

$$v(r) = (2V/\pi a^2)(1 - r^2/a^2) \tag{102}$$

The velocity gradient or shear rate $G(r)$ is given by

$$G(r) = -dv(r)/dr = Pr/2L\eta = 4Vr/\pi a^4 \ , \tag{103}$$

where the velocity gradient is negative because $v(r)$ decreases with increasing r. The maximum shear rate, G_M, clearly occurs at $r = a$, and

$$G_M = Pa/2L\eta = 4V/\pi a^3 \tag{104}$$

Since the degree of orientation of the DNA molecule in a flowing solution (in the sense that the helical axis is aligned parallel to the flow streamlines) depends on the shear rate [205, 244-250], the quantity G_M in Eq. (104) is the one of interest to the present work. With knowledge of the capillary radius and volume flow rate as described earlier, maximum shear rates can be calculated from Eq. (104).

The maximum shear stress is given by

$$\eta G_M = Pa/2L = 4V\eta/\pi a^3 \tag{105}$$

The quantity is of importance because the breaking force on a polymer molecule is proportional to the shear stress. A constant shear stress can be applied in experiments at different viscosities by maintaining the same pressure gradient (P/L). The Reynolds number is the ratio of the inertial forces to viscous forces and for flow in a capillary is

$$R = P\rho a^3/4L\eta^2 = 2\rho V/\pi\eta a \ , \qquad (106)$$

where ρ is the density of the solution. Flow may become turbulent, rather than laminar, if $R \geq 2200$, although in practice higher Reynolds numbers may be achieved without turbulence if the entrance and exit of the capillary are smooth and tapered. Approximate calculations using Eq. (106) and the flow rates encountered in the present work indicate a Reynolds number well below the critical value and hence the flow in the present work is considered thoroughly laminar. It is known that flow through a curved pipe or coil gives rise to a secondary circulation of fluid, called the double-eddy or Dean effect, that takes place at right angles to the main flow. This circulation stabilizes laminar flow, thus increasing the critical Reynolds number. Consequently, the loops inherent in the coiled tubing of the parallel flow cell configuration are not considered to have a deleterious effect on maintenance of laminar flow with this cell system.

Analysis and Discussion of Results

Nomenclature

Two types of perpendicular flow cell and four different types of parallel flow cell were constructed and extensively tested to optimize the flow system. For convenience of reference and discussion, the following abbreviated nomenclature is adopted for these cells. Each cell is designated by two letters (PE for the perpendicular cells and PA for the parallel cells) followed by a number referring to the number of capillary tubes for flowing solution in the cell for perpendicular cells and the total number of parallel sections across the flat portion of the cell for parallel cells. In addition, a final letter is added designating the capillary radius, A signifying a radius of 0.0125 inch and B a radius of 0.0065 inch. Thus, for example, the notation PA28A refers to a parallel flow cell containing 28 parallel holes in its flat portion through which Teflon capillary tubing with a radius of 0.0125 inch is threaded. Table XIV gives the additional dimensions of the parallel cells not specified in Figure 26 and Table XV gives the volumes available for sample solution within the cavity for all cells used.

In the case of the parallel flow cells it is important to consider not only the total volume but also how this volume breaks down into flow regions of strictly parallel or strictly random orientation with respect to the applied magnetic field. These data are also given in Table XV, where V_T is the total volume, $V_{||}$ and $V_{\perp}$ are the parallel and perpendicular volumes, respectively, and V_R is the random volume. In the case of the perpendicular flow cells, $V_T = V_{\perp}$, and there is no equivalent to V_R. The volume of the loops, which have a random flow configuration with respect to the applied magnetic field, in the parallel flow cells is calculated from the usual formula for the volume of a cylinder,

$$V_R = N\pi r^2 a \, , \qquad (107)$$

where N is the total number of loops (always one less than the number of parallel sections), r is the capillary radius, and a is the cylindrical

TABLE XIV

Dimensions (in inches) of Parallel Flow Cells Used with the Varian E-3 ESR Spectrometer

Cell Designation			
PA14A	PA28A	PA25B	PA37B
Number of Holes			
14	28	25	37
Hole Diameter = Width and Depth of Narrow-Side Slot			
0.0520	0.0520	0.0320	0.0320
Center-to-Center Distance of Holes			
0.157	0.085	0.094	0.064
Center of First Hole to End of Flat Section Distance			
0.1595	0.0325	0.0520	0.0280
Width and Depth of Slots in Cylindrical Supports			
1/16	1/16	1/32	1/32

TABLE XV

Volumes of Flow Cells Used with the Varian E-3 ESR Spectrometer

Cell[a]	$V_T(in^3)$	$V_{\|\|}(in^3)$	$V_R(in^3)$	$V_R/V_{\|\|}$	V_R/V_T
PA14A	0.003608	0.002034	0.001574	0.7739	0.4363
PA28A	0.005837	0.004068	0.001769	0.4349	0.3031
PA25B	0.001586	0.001115	0.0004705	0.4220	0.2967
PA37B	0.002130	0.001650	0.0004802	0.2910	0.2255

[a] For the corresponding perpendicular flow cells, $V_T = V_{\perp}$, that is,

PE1A $V_T = 0.001159$ in^3

PE3B $V_T = 0.0006266$ in^3 .

The volume of the flat quartz ESR aqueous solution sample cell is

$V_T^{quartz} = 0.009153$ in^3

altitude taken to be the length of the line through the center of the cylindrical lamp.

Flow Parameter Relations

The observed effects on the ESR spectrum of a drug-DNA complex due to flowing the solution through a capillary in the resonant cavity depend not simply on the degree of orientation of the DNA helices or the cell geometry but rather on a larger set of interacting parameters. Changing one parameter can drastically alter the observed result and all possible parameters must be considered in optimizing a system such as this. A schematic representation of the relationships among the various parameters of the flow system used with the Varian E-3 ESR spectrometer is shown in Figure 29, where the arrows indicate that one parameter acts on another.

Detailed analysis of the ESR spectra is presented in Chapter IX, but the salient features in optimizing the flow system are as follows. The random (no flow) X-band ESR spectrum of the drug-DNA complexes consists of an asymmetrical three-line hyperfine pattern (due to interaction with the ^{14}N nucleus of the phenothiazine drug) which is a superposition of the three parallel hyperfine lines and the unresolved perpendicular resonance line. If the drug radical cation intercalates with the DNA helix, then the perpendicular flow ESR spectrum consists of one line and the parallel flow spectrum consists of three lines resembling the random pattern but much better resolved and less asymmetrical, the intensities being more equal. Thus the observed effect in the ESR spectrum with flow is an enhancement of resolution for parallel flow and observance of a single line for perpendicular flow. The higher the degree of

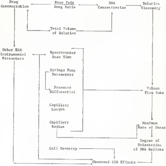

Figure 29 Relationships among the various parameters of the flow system used with the Varian E-3 ESR spectrometer. Arrows indicate which other parameters a given parameter affects.

orientation of DNA helices with intercalated molecules and the larger the fraction of total values commensurate with flow strictly parallel or perpendicular to the applied field, the more pronounced the observed effects become. Most of the remaining discussion will be devoted to the parallel flow cells, which are more interesting and show more striking results than the perpendicular cells.

Results and Optimization of the Flow System

The first cell constructed was the PA14A cell, the other cells being constructed as a consequence of efforts to optimize the system. The sample of choice for experiments optimizing the system was the CPZ-DNA complex since comparison with previous data [209] was possible. Flowing CPZ-DNA solutions through the PA14A cell yielded distinct although not extraordinary results. Orientation effects were clearly recognizable. The PA37B cell was the end result of optimization of the parallel flow system. Figure 30 compares parallel flow spectra obtained with both of these cells. As can be seen from Figure 30 the orientation effect, evident as enhanced resolution in the spectrum, is much greater for the PA37B cell than it is for the PA14A cell. It should be noted that the values of G_M given in Figure 30 are the values calculated from Eq. (104) using the measured volume flow rate. Comparison of G_M values is valid only for constant capillary radius and viscosity and variable flow rate or for constant flow rate and viscosity and variable capillary radius. Since both capillary radius and volume flow rate differ in the two spectra shown in Figure 30, a comparison of the G_M values there is somewhat misleading. For constant flow rates the G_M values for the two types of capillary tubing used here are related by the expressions $G_M(\mathrm{PA14A})/G_M(\mathrm{PA37B}) = [r(\mathrm{PA37B})/r(\mathrm{PA14A})]^3 = 0.14$. Hence, for a G_M value

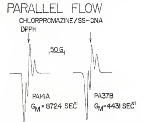

Figure 30. Comparison of parallel flow ESR spectra obtained using the PA14A and PA37B cells discussed in the text, illustrating the effect of different cell designs on the observed spectrum

of 4431 sec^{-1} for the FA37B cell, the corresponding value of G_M in the FA14A cell for the same volume flow rate would be 620 sec^{-1}. Thus the difference in the rates of shear for comparable flow volumes arises from the difference in capillary radius. Since a shear rate of 8724 sec^{-1} in the FA14A cell corresponds to a shear rate of 62,314 sec^{-1} for equal volume flow rate in the FA37B cell, it is evident from Figure 30 that the FA37B cell is indeed far superior to the FA14A cell.

The effect on the flow spectrum of the cell geometry lies essentially in the amount of parallel versus random volume available for a given capillary radius and rate of shear. Comparison of results obtained using the FA14A cell ($V_R/V_{||}$ = 0.7739) and the FA28A cell ($V_R/V_{||}$ = 0.4349), as well as the FA25B cell ($V_R/V_{||}$ = 0.4220) and the FA37B cell ($V_R/V_{||}$ = 0.2910), showed that the larger the parallel volume (compared to the random volume) the more pronounced the effect observed for constant capillary radius and shear rate, using a solution of the same viscosity throughout. Therefore, optimization of the cell geometry within the dimensions dictated by consideration of the cavity requires minimizing $V_R/V_{||}$ by having as many parallel sections through the flat part of the cell as is possible without inflicting flow-retarding kinks in the looped sections from too drastic curvature in the coiled configuration of the parallel flow cells.

From Eq. (104) it is evident that the maximum rate of shear (and thereby the degree of orientation) may be increased by either increasing the volume flow rate or decreasing the capillary radius. Since G_M varies inversely as a^3, decreasing the capillary radius has a large effect. This is also clear from the comparison of the FA14A and FA37B spectra in Figure 30. A minor disadvantage of decreasing the capillary radius is that reduction of the inlet orifice tends to increase the back pressure in the syringe so that smaller syringe sizes must be used. Of course, that means smaller sample volumes can be used, a distinct advantage with precious biological materials.

Figure 31 shows ESR spectra obtained with the PA37B cell and illustrates the effect of increasing rate of shear on the observed spectrum. Figure 32 compares perpendicular flow spectra obtained using the PE1A and PE3B cells. Results from experiments with all cells indicate that there is a limit to the effects observed with increasing shear rate. Although this is also true of the perpendicular flow cells, it is more noticeable in the parallel flow situation where the observed spectral changes are more striking. The results show that increasing the shear rate above about 12,000 sec^{-1} does not lead to increased orientation effects in the spectrum for a given sample solution and cell. In the case of the perpendicular flow cells this is attributed to the rather insensitive nature of the observed flow spectrum and to the fact that, as Lerman [205] points out, the DNA molecule in solution appears to be a statistical coil of limited flexibility and only partial orientation can be expected. Furthermore, perfect orientation requires infinitely great shear and that is hardly the case here. In the case of parallel flow it must be remembered that the loops in the cell configuration provide thoroughly random orientation which is not changed by flow. Consequently, the observed spectrum for parallel flow is always a superposition of random and parallel spectral features. Ideally, parallel flow should enhance the appearance of the parallel hyperfine lines and cause the near or total disappearance of the unresolved perpendicular triplet. The inherent random orientation of the loops means there will

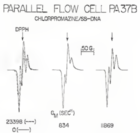

Figure 31 Parallel flow ESR spectra obtained using the PA37B cell discussed in the text, illustrating the effect of increasing rate of shear on the spectrum observed

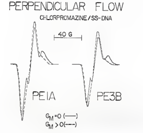

Figure 32. Comparison of perpendicular flow ESR spectra obtained using the PE1A and PE3B cells discussed in the text.

always be intensity contributions from the perpendicular line. Since the linewidth of the perpendicular line is sufficient that it overlaps at least one of the parallel lines and probably distorts another, it is not unlikely that there is a point beyond which further orientation of the DNA helices contributes such small changes to the spectrum that they are lost in the contribution from the random orientation. However, this imperfection of the parallel flow cell does not impede its use because the major objective is to observe the effects of flowing solutions and as long as the effect is of sufficient magnitude it is unnecessary to press for total elimination of the random configuration. Indeed, Ohnishi and McConnell [209] attribute the asymmetry of their ESR spectra to incomplete orientation of the DNA helices. Presumably their apparatus did not include inherent random orientation in the parallel flow configuration.

The capillary length and radius, solution viscosity, and the pressure differential between the entrance and exit affect the degree of orientation through the rate of shear. The capillary length is not particularly amenable to change in the present situation and the pressure differential depends on the rate at which the syringe pump is operated for a given syringe and capillary size. For the present experiments the solution viscosity is determined by the presence of DNA molecules. It is well known [204-207] that, since the DNA molecule becomes longer and stiffer on binding an intercalating molecule, an increase in the viscosity of DNA solutions is characteristically observed as a consequence of the intercalation process. The lower the nucleotide base pair to radical cation ratio (BP/R), the larger the number of intercalating molecules becomes and so the solution viscosity increases as BP/R decreases. Consider, for example, two CPZ-DNA solutions, one with BP/R = 9 and one with BP/R = 3. From Eq. (104) it can be seen that for the same pressure gradient (P/L) and capillary radius, the rates of shear for two solutions differing only in viscosity are related by their viscosities. For the present example, it is seen that $G_M(BP/R = 9)/G_M(BP/R = 3) = \eta(BP/R = 3)/\eta(BP/R = 9)$. Since it is to be expected that $\eta(BP/R = 3) > \eta(BP/R = 9)$, then clearly it is also expected that $G_M(BP/R = 9) > G_M(BP/R = 3)$. Results using the present system show these considerations to be correct. Figure 33 shows the results obtained for a CPZ/SS-DNA complex using the PA37B cell and varying BP/R from 9 to 3 (DNA concentration constant, drug concentration varied). The decrease in the observed parallel orientation effect as BP/R varies from 9 to 3 is evident from Figure 33 and illustrates the effect that the value of BP/R and solution viscosity have on the observed effects. The values of G_M shown in Figure 33 are those calculated from volume flow rates and hence do not accurately depict the true relative values among the spectra shown.

The effects of other parameters in the experimental flow system may be inferred from Figure 29. In practice concentrations of drug radicals less than about 10^{-4} M are not desirable since the sensitivity of the Varian E-3 rapidly deteriorates at lower concentrations, at least for the present system. Consequently, drug radical concentrations were typically on the order of 5×10^{-4} M and BP/R was typically about 5. With the PA37B cell either 3-cc or 1-cc syringes were used, larger syringe sizes being impractical because severe back pressure hindered smooth pumping action. The syringe pump could be used over the entire range of percent-flow settings. A microwave power of about 5 mW was typically used. Gain settings were usually on the 10^5 scale with a modulation amplitude of about 3.2 G and a time constant of 0.3 sec. A scan time of 4 minutes usually gave satisfactory results. Although shorter scan times could

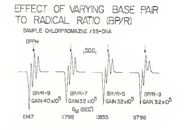

Figure 33 Effects of varying the nucleotide base pair to radical drug cation ratio (BP/R) on the observed orientation effects, illustrating their dependence on solution viscosity

be used, the quality of the observed spectra was not as acceptable. Attempts to connect sample solutions with higher DNA concentrations and thereby higher radical concentrations for BP/B about 5 in order to allow use of lower modulation amplitudes in the hope of resolving additional hyperfine structure were unsuccessful. Preparing the solutions usually caused some fibrous precipitation and those prepared were so viscous that useful flow studies were rather impractical. Attempts to shear the concentrated solutions (thereby lowering the viscosity) by several days of stirring at moderate speeds yielded some workable solutions but the ESR data were inconclusive.

CHAPTER IX

THE ESR SPECTRA OF PHENOTHIAZINE DRUG RADICAL COMPLEXES WITH DNA

Ohnishi and McConnell [209] have demonstrated that the radical cation of the phenothiazine drug derivative chlorpromazine interacts with calf thymus DNA and *E. coli* transfer RNA through an intercalative mode of binding similar to that described by Lerman [204,205,248] for the acridine dyes. In the case of intercalation, the aromatic molecular plane of CPZ would be perpendicular to the DNA helical axis. Ohnishi and McConnell [209] found that such was the case through the use of electron spin resonance studies of the CPZ-DNA complex. The present study duplicates and confirms their results for the CPZ/CT-DNA complex and extends the study to the CPZ/SS-DNA complex as well as the complexes with CT-DNA and SS-DNA of two other phenothiazine drugs, triflupromazine (TFP) and methiomeprazine (MMP).

The Experimental Spectra

As discussed in Chapter VIII, the interaction of the drug radical cation with DNA is examined by ESR in the following way. Three types of ESR spectra are required: (1) randomly oriented (no flow) DNA-bound drug radicals, (2) the 'perpendicular flow' ESR spectrum of DNA-bound drug radicals, where the DNA helical axis is oriented perpendicular to the applied magnetic field by flowing the solution through a capillary tube in the resonance cavity, and (3) the corresponding 'parallel flow" ESR spectrum. Figure 34 shows the X-band ESR spectrum of the CPZ/SS DNA

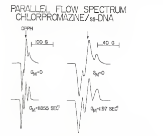

Figure 34 X-band ESR spectrum of the chlorpromazine radical cation complex with salmon sperm DNA. Upper spectra are for random orientation (no flow), lower spectra are for parallel flow. Spectra on the right are expanded compared to those on the left

complex in both the random and parallel flow orientations. Figure 35 shows the corresponding spectrum for the TFP/SS-DNA complex and Figure 36 shows the spectrum of the MMP/SS-DNA complex. The perpendicular flow spectrum in all cases is similar to those shown in Figure 32 (see Chapter VIII). Spectra obtained for complexes of CPZ, TFP, and MMP radical cations with CT-DNA are similar to the spectra in Figures 34, 35 and 36. This is to be expected in view of the similar nucleotide base content of these two types of DNA (see Chapter VI). Figure 37 shows the X-band ESR spectrum of the CPZ/CT-DNA complex in the random and parallel flow orientations. The spectrum shown in Figure 37 was obtained for a solution of CPZ/CT-DNA complex that had been stored under refrigeration at 4°C for a period of 6 months after its initial preparation. The spectrum is essentially unchanged from that recorded when the complex was first formed. Similar results were obtained with the CPZ/SS-DNA complex, as well as DNA complexes with TFP and MMP radical cations, and illustrates the marked stability of the drug-DNA complexes. These findings are in accord with the observations of Ohnishi and McConnell [209], who found the CPZ radical to be markedly stabilized by the presence of CT-DNA.

Discussion: The A-Tensor

Mechanism of Hyperfine Interaction in Conjugated Systems

The mechanism of the hyperfine interaction in conjugated systems is well understood [38-41,43,44,76,77,79]. The unpaired electron in a π-type radical is expected to be distributed over the molecular framework. In planar conjugated hydrocarbon radicals, for example, proton hyperfine splittings are proportional to the unpaired π-electron density on the carbon atom adjacent to the proton. This is expressed by McConnell's

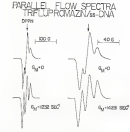

Figure 35. X-band ESR spectrum of the triflupromazine radical cation complex with salmon sperm DNA. Upper spectra are for random orientation (no flow), lower spectra are for parallel flow. Spectra on the right are expanded compared to those on the left.

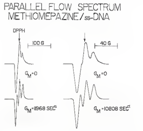

Figure 36 X-band ESR spectrum of the methiomepazine radical cation complex with salmon sperm DNA. Upper spectra are for random orientation (no flow), lower spectra are for parallel flow. Spectra on the right are expanded compared to those on the left

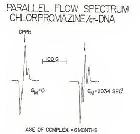

Figure 37. X-band ESR spectrum of the chlorpromazine radical cation complex with calf thymus DNA. Spectrum on the left is for random orientation (no flow), spectrum on the right for parallel flow. The spectrum is for a sample 6 months old

relation [251,252]

$$a_i = Q\rho_i \ , \qquad (108)$$

where the a_i are the isotropic proton hyperfine splittings, ρ_i are the π-electron spin densities on the carbon atoms, and Q is a proportionality constant having a value in the range of −20 to −30 G (not to be confused with the use of Q for the cavity quality factor, as discussed previously in Chapter VIII). Isotropic proton hyperfine splittings arise when there is net unpaired-electron density at the proton. The unpaired electron in π-radicals resides in a π-molecular orbital constructed from a linear combination of carbon $2p_z$ atomic orbitals. Each $2p_z$ orbital has a node in the plane of the molecule and because this plane also contains the protons there should be no unpaired-electron density at the proton and hence no hyperfine splitting. Since experimental evidence indicates that isotropic proton hyperfine interactions do occur in π-radicals, the concept of unpaired-electron density must be examined in more detail.

Spin density is a function of many electrons and can be defined as

$$\rho_i = P_i(\alpha) - P_i(\beta) \ , \qquad (109)$$

where ρ_i is the spin density in region i of the molecule and $P_i(\alpha)$ and $P_i(\beta)$ are the total probability densities of electrons possessing α and β spin, respectively, in the region i. $P_i(\alpha)$ and $P_i(\beta)$ are obtained by summing the densities of all α-spin and β-spin electrons, respectively. Consider a C-H fragment of a conjugated system with the $2p_z$ atomic orbital of the carbon atom perpendicular to the C-H bond and the carbon $2p_x$ and $2p_y$ atomic orbitals hybridizing with the carbon 2s atomic orbital to form trigonal sp^2 orbitals, one of which bonds to the hydrogen atom.

If spin α is arbitrarily assigned to the one electron in the $2p_z$ carbon orbital, there are two possibilities for assigning the spins in the C-H σ bond, namely, $Csp^2(\alpha)H1s(\beta)$ and $Csp^2(\beta)H1s(\alpha)$. If there were no electrons in the carbon $2p_z$ orbital, these two electron configurations would be equally probable and the spin density at the proton would be zero. When the $2p_z$ carbon electron is present, however, the configurations $Csp^2(\beta)H1s(\alpha)$ and $Csp^2(\alpha)H1s(\beta)$ are no longer equally probable. It is well known that, when two different orbitals on the same atomic nucleus are singly occupied by electrons, the more stable arrangement for the ground state is that with the higher multiplicity, that is, as stated by one of Hund's rules, that one with the electron spins parallel ($\alpha\alpha$ or $\beta\beta$). Thus, the configuration $C2p_z(\alpha)Csp^2(\alpha)H1s(\beta)$ is slightly preferred because of the favorable exchange interaction between the π-electron and the carbon σ-electron, whose spins are parallel. The spins of the electrons in the C-H σ-bond are therefore slightly polarized, that is, there will be a net negative spin density (excess of β-spin over α-spin) at the proton. There will also be a net positive spin density at the carbon atom. If there is one unpaired electron in the $2p_z$ orbital, the negative spin density at the proton will produce a negative proton hyperfine splitting, the magnitude of which is denoted by Q. The effect is often called spin polarization. In a conjugated radical system the unpaired electron density ρ_i at a given carbon atom will usually be less than unity and the hyperfine splitting can be obtained from Eq. (108). The negative sign of a_i has been confirmed experimentally and it is clear that Q should be negative.

In the above discussion it was necessary to consider only the interaction of the π-spin density with the σ-electrons in one bond, the C-H bond. In the case of nuclei which form part of the framework of a conjugated molecule, interactions with several bonds must be considered In the above discussion a positive spin density at the carbon nucleus is induced by the same mechanism which produces a negative spin density at the proton of the C-H group. Experimental ^{13}C hyperfine splittings, however, indicate that the splittings are not simply proportional to the π-spin density on the same carbon atom. It is thus necessary that contributions from π-spin densities on neighboring carbon (or other) atoms be considered. Consider the fragment

The several interactions can be characterized by the Q parameters Q^H_{CH}, Q^C_{CH}, $Q^C_{CC'}$, $Q^C_{C'C}$ and the parameter S^C, where the superscript identifies the atom causing the hyperfine splitting, the first subscript identifies the atom on which the π-spin density is contributing to the spin polarization, the two subscripts together identify the bond being polarized, and S^C is a parameter that characterizes the polarization of the carbon 1s electrons by the local π-spin density. By analogy with the C-H fragment, Q^C_{CH} and $Q^C_{CC'}$ are expected to be positive and $Q^C_{C'C}$ and Q^H_{CH} negative. The combined contributions can be expressed as

$$a_i^C = (S^C + \sum_{j=1}^{3} Q^C_{CX_j})\rho_i + \sum_{j=1}^{3} Q^C_{X_jC}\rho_j \,, \qquad (110)$$

where the atoms X_j are bonded to carbon atom i

In nitrogen heterocyclic aromatic molecules the ^{14}N nucleus substitutes for carbon and Eq (110) might be expected to apply Although in principal correct, evidence indicates that the effect of π-spin densities on neighboring atoms is small that is, $Q^N_{C'N}$ must be small in view of small contributions from neighboring atoms many workers use the simpler equations,

$$a_1^N = Q^N_{N(C_2H)}\rho_N , \qquad (111a)$$

$$a_1^N = Q^N_{N(C_2P)}\rho_N , \qquad (111b)$$

for ^{14}N hyperfine splittings. Equation (111a) applies to protonated nitrogen sites and Eq. (111b) to nonprotonated nitrogen sites, the P designating the lone pair of electrons on ^{14}N. Values of Q in Eq. (111a) range from +27 to +30 G and from +23 to +26 G in Eq. (111b). The major contribution to the nitrogen hyperfine splitting derives from the π-spin density on the nitrogen atom itself and positive hyperfine splittings are expected and have been confirmed experimentally.

Virtually all nitrogen-containing aromatic radicals have well resolved ^{14}N hyperfine structure if there is any π-spin density on the nitrogen atom. In oriented systems the anisotropic hyperfine tensors (see Chapter III) of both ^{13}C and ^{14}N depend primarily on the unpaired-electron density in the appropriate $2p_z$ atomic orbital of the same atom and the isotropic hyperfine interaction measures the s-character of the odd electron. If the unpaired electron were localized entirely in a $2p_z$ orbital the traceless dipolar hyperfine tensor would necessarily be axially symmetric, small departures from axial symmetry arising from the presence of unpaired electrons on other parts of the molecule. The general features of ^{14}N hyperfine splittings in oriented π-electron radicals are very similar to those of ^{13}C and the dipolar hyperfine tensors are usually close to being axially symmetric.

Interpretation of Observed Spectra

The observed ESR spectra are readily interpreted in terms of Lerman's intercalation model [204,205,248] where the DNA helix axis is perpendicular to the aromatic plane of the phenothiazine nucleus of the drug molecules. In the intercalation model the drug molecules bind to the DNA double helix by sliding between adjacent nucleotide base pairs with local extension and unwinding of the deoxyribose-phosphate backbone. The observed hyperfine splitting is in all cases due to interaction with the ^{14}N nucleus of the phenothiazine ring system. The CPZ case is used as an example. The isotropic ^{14}N hyperfine splitting, $A_{iso}(^{14}N)$, measured from the solution spectrum of free CPZ radical cations is about 6 G [223,224,227]. By analogy with known ^{13}C anisotropic π-electron hyperfine interactions in the $CH(COOH)_2$ radical [249], a hyperfine splitting ($A_{||}$) parallel to the π-orbital axis of the aromatic nitrogen atom is expected to be approximately twice the isotropic splitting and the hyperfine splitting ($A_{\perp}$) perpendicular to the π-orbital axis is expected to be much less than the isotropic splitting. Such expectations are borne out, for example, by the anisotropy of the ^{14}N hyperfine interaction in di-t-butylnitroxide, $(CH_3)_3CNOC(CH_3)_3$, where $A_{||}(^{14}N)/A_{iso}(^{14}N) = 2.35$ and $A_{\perp}(^{14}N)/A_{iso}(^{14}N) = 0.33$ [250]. Therefore, a ^{14}N hyperfine splitting of $A_{||}(^{14}N) = 2.35 \times 6 = 14.1$ G is expected when the plane of CPZ is perpendicular to the applied magnetic field, that is, the field is parallel to the π-orbital axis of the aromatic nitrogen atom. Ohnishi and McConnell [209] observed a triplet splitting of about 17 G in their parallel flow spectrum of the CPZ/CT-DNA complex and no hyperfine splitting in the perpendicular flow spectrum. These are the results expected if the plane of the CPZ radical cation is perpendicular to the DNA helical axis. The same results are observed in the present work (see Figures 34, 35 and 36 for example). Ohnishi and McConnell [209] attribute the asymmetry of their Q-band ESR spectra to incomplete orientation of the

DNA helices, a result not unexpected since, as Lerman [204,205,248] points out, the DNA molecule in solution appears to be a statistical coil of limited flexibility and thus only partial orientation in a flowing solution can be expected.

The argument favoring perpendicularity of the plane of the CPZ radical to the helix axis is more general than that just discussed. As Ohnishi and McConnell [209] observe, when $|A_{||}| >> |A_{\perp}|$, the hyperfine splittings just detectable in the random (no flow) spectrum must be equal to $|A_{||}|$, irrespective of the relative orientation of the CPZ radical to the DNA helical axis. Therefore, the observed equality of the splittings for random orientation and orientation in the instance of parallel flow is a necessary condition for perpendicularity of the CPZ plane to the helical axis. A sufficient condition for perpendicularity is that this equality must persist for all laminar rates of shear, no matter how high. Ohnishi and McConnell [209] verified this for the CPZ/CT-DNA complex up to a maximum shear rate of about 9000 sec^{-1}. The present results have shown an equality in the hyperfine splitting over a range of shear rates of about 400 to 25,000 sec^{-1} for CPZ, TFP, and MMP radical cation complexes with CT-DNA and SS-DNA.

Discussion: The g-Tensor

General Consideration of the g-Tensor in Aromatic Radicals

Observed values of g_{iso} (see Eq. (29), Chapter III) for aromatic radicals are typically about 0.0002 to 0.004 higher than the free-spin g-factor, g_e = 2.0023 [253]. Single-crystal measurements indicate that molecular g-tensors of aromatic radicals are anisotropic and $g_{||}$ and $g_{\perp}$ usually also exceed g_e [253].

Qualitatively such observations can be explained in terms of spin-orbit interaction which mixes σ and π configurationally excited states with the ground state. Consider an axially symmetric planar aromatic radical where $g_{||}$ and $g_{\perp}$ refer to magnetic field directions perpendicular and parallel to the plane of the aromatic ring, respectively. Excitations of the type $\sigma^* \leftarrow \pi$ with average energy ΔE_1 involve excitation of the odd π-electron into an antibonding σ-orbital, σ^*, and reduce $g_{\perp}$ by $2\lambda/\Delta E_1$, where λ is the 2p spin-orbit coupling parameter (compare Eqs (B4) through (B6) in Chapter III). The $\pi \leftarrow \sigma$ excitations increase $g_{\perp}$ by $2\lambda/\Delta E_2$ and involve excitation of σ-bonding electrons to π-orbital states with average energy ΔE_2. On the other hand, $g_{||}$ must be close to g_e because only highly energetic, and therefore relatively unimportant, $\sigma^* \leftarrow \sigma$ transitions or very weak multicenter spin-orbit interactions involving $\pi^* \leftarrow \pi$ transitions can contribute to $g_{||}$ [253]. Thus, $g_{iso} \cong (g_e + 2g_{\perp})/3$ and $g_{iso} > g_e$ if $\Delta E_1 > \Delta E_2$. The inequality corresponds to the qualitatively reasonable conclusion that σ^* states are more energetically antibonding than the σ states are bonding [253]. Most heteroatom substitutions are predicted to further increase g_{iso} and $g_{\perp}$ because typical substituents have larger λ values and several hetero groups have nonbonding (n) n-electrons which show low energy $\pi \leftarrow n$ transitions which reduce the effective ΔE_2. These effects are proportional to the odd-electron density on the heteroatom.

The Observed g-Tensor Behavior

Ohnishi and McConnell [209] observed g-factor anisotropies ($g_{||}$ = 2.003, $g_{\perp}$ = 2.006, g_{iso} = 2.005) for the CPZ/CT-DNA complex commensurate with the intercalation geometry and the above considerations concerning g-factor anisotropies in π-electron radicals. The results of the present work with CPZ, TFP, and MMP radical complexes with CT-DNA and SS-DNA exhibit similar g-factor anisotropies, as is detailed in a later section. Furthermore, the observed g-factor anisotropies for DNA-bound drug radicals are in agreement with recently observed [254] g-tensor anisotropies in ESR spectra of solid perchlorate salts of several phenothiazine free radicals, all of which show similar but not identical g-tensor anisotropy [88]. The results are also in qualitative agreement with the published value of $g_{iso} = 2.0034$ for both chlorpromazine and triflupromazine [226].

The Observed Magnetic Parameters

It is expected and observed that $A_{\perp}(^{14}N)$ is much less than $A_{iso}(^{14}N)$. Indeed, no perpendicular hyperfine splittings were resolved. It is of some interest to obtain reasonable estimates of the magnitude of $A_{\perp}(^{14}N)$ in order to generate computer-simulated spectra using the exact magnetic parameters available and so that some idea of the magnitude of the anisotropic or dipolar part of the hyperfine tensor, A_{dip}, may be obtained. From Eq. (78) in Chapter III the following relations may be obtained

$$A_{iso} = (A_{||} + 2A_{\perp})/3 , \tag{112a}$$

$$A_{dip} = (A_{||} - A_{\perp})/3 . \tag{112b}$$

Using Eq. (112a), known values of $A_{iso}(^{14}N)$ from solution studies, and experimentally determined values of $A_{||}(^{14}N)$ for the drug-DNA complexes, a reasonable estimate of $A_{\perp}(^{14}N)$ may be obtained. Use of Eq. (112b) then permits estimation of $A_{dip}(^{14}N)$. For CPZ a value of $A_{iso}(^{14}N) = 5.6$ G is available [223,224]. For TFP a value of $A_{iso}(^{14}N) = 7.2$ G is available from the work of Fenner [255]. Isotropic hyperfine constants for MMP are apparently not available in the literature. However, Fenner [256] has determined isotropic parameters for a structurally similar compound, thioridazine. Assuming that the differences in the 10-alkyl

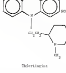

Thioridazine

groups of thioridazine and methiomeprazine (see Chapter VI) exert a negligible effect on the isotropic ^{14}N hyperfine interaction for the ring nitrogen, the value of $A_{iso}(^{14}N) = 7.0$ G for thioridazine may be used as an approximation to $A_{iso}(^{14}N)$ for MMP. In view of Eqs. (111) and (112) and the fact that $A_{||} < 3A_{iso}$, the sign of $A_{||}$ and $A_{\perp}$ seems clearly positive here. The magnetic parameters derived from the present experiments are given in Table XVI (the g- and A-values are the same within experimental tolerance for both the CT-DNA and SS-DNA complexes). The isotropic hyperfine coupling constant, A_{iso}, is related to the unpaired spin density at the nucleus, $|\psi(0)|^2$, according to Eq. (79) in Chapter III, while the anisotropic or dipolar coupling parameter, A_{dip}, is given by Eq. (80) in Chapter II and is expected to be positive for contributions arising only from pπ electrons. From Table XVI it is seen that

TABLE XVI

Magnetic Parameters for DNA-Bound Radical Cations of Chlorpromazine (CPZ), Triflupromazine (TFP) and Methiomeprazine (MMP)

Drug	$g_{\|\|}$	$g_{\perp}$	$A_{\|\|}$(G)	$A_{\perp}$(G)[a]	A_{iso}(MHz)	A_{dip}(MHz)
CPZ	2.003	2.006	16.25	0.275	15.7[b]	14.9
TFP	2.003	2.006	17.24	2.18	20.2[c]	14.1
MMP	2.003	2.007	14.80	3.10	19.6[d]	10.9

[a] Calculated from the relation $A_{iso} = (A_{\|\|} + 2A_{\perp})/3$ as discussed in the text. A-values are considered accurate to ±0.5 G.

[b] From [223,224].

[c] From [225].

[d] From [256].

all three DNA-bound drug radicals exhibit considerable anisotropy in the A-tensor (if $A_\perp$ were equal to $A_{||}$, then of course the A-tensor would be isotropic).

Fenner [255,256] has shown that for the phenothiazine ring system

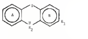

delocalization of the unpaired electron occurs principally in ring A for electron-accepting substituents such as $-CF_3$ (and $-Cl$) as the $-R_1$ group and in ring B for electron-donating substituents such as $-SCH_3$ in the $-R_1$ position. Fenner also noted that $-CF_3$ is anomalous for electron-accepting substituents in that some delocalization of the unpaired electron can be detected on this substituent (Fenner also studied $-CN$ and COC_3H_7 at $-R_1$). Borg and Cotzias [223,224] concluded that their ESR data for CPZ indicate that the following resonance form is likely to be the stable one for the radical cation:

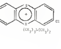

Thus there is evidently an asymmetry of charge distribution, or at least a delocalization of charge distribution, over the phenothiazine ring system depending on the nature of the 2-substituent.

Consideration of the magnetic parameters in Table XVI indicates that there is also delocalization of the unpaired electron in the DNA-bound drug radicals. For example, the wavefunction for the odd electron in the ground state of the drug radical can be written as an LCAO,

$$\Psi(\text{drug}) = c_1\phi(\text{N2s}) + c_2\phi(\text{N2p}_z) + \sum_{i>2} c_i\phi_i \ , \qquad (113)$$

where $\phi(\text{N2s})$ is the 2s atomic orbital of the nitrogen, $\phi(\text{N2p}_z)$ is the $2p_z$ atomic orbital of the nitrogen which participates in the π-system, the ϕ_i represent the atomic orbitals of all other atoms i in the aromatic system contributing to the LCAO, c_1 is the coefficient of the nitrogen 2s AO, c_2 the coefficient of the nitrogen $2p_z$ AO, and the c_i are the coefficients of the corresponding ϕ_i. To a first approximation the s- or p-character of the odd electron at a particular nucleus can be obtained by taking the ratio of A_{iso}(molecule)/A_{iso}(atom) or A_{dip}(molecule)/A_{dip}(atom), respectively (see Chapter III). Then from Eq. (113) this approximation can be used as follows:

$$c_1^2 = A_{iso}^N(\text{drug-DNA complex})/A_{iso}^N(\text{atom}), \qquad (114a)$$

$$c_2^2 = A_{dip}^N(\text{drug-DNA complex})/A_{dip}^N(\text{atom}) \ . \qquad (114b)$$

Using Eqs. (114) and the magnetic parameters in Table XVI, the results of Table XVII are obtained. The s-character of the odd electron is small, as expected, while the p-character indicates considerable delocalization of the odd electron. This procedure is only approximate, of course, and depends upon the doubtful supposition that the atomic properties are unchanged in the molecule. However, it is readily applied and provides

TABLE XVII

Estimations of the Coefficients of the Nitrogen 2s and $2p_z$ Atomic Orbitals in the Molecular Orbital of the Odd Electron of DNA-bound Drug Radicals

Drug	$\frac{A_{iso}^{N}(\text{complex})^{a}}{A_{iso}^{N}(\text{atom})}$	$\frac{A_{dip}^{N}(\text{complex})^{a}}{A_{dip}^{N}(\text{atom})}$
CPZ	0.0102	0.3117
TFP	0.0131	0.2950
MMP	0.0127	0.2280

[a] Atomic values of $A_{iso}(^{14}N) = 1540$ MHz and $A_{dip}(^{14}N) = 47.8$ MHz were used from [44].

useful qualitative information. It is to be expected that the spin distribution in the radical cations is little affected by complexing with DNA. It is interesting that the change in spin distribution in going from the native drug molecule to the radical causes a change in the mode of interaction with DNA. The radical cation interacts through an intercalative mode of binding whereas according to the work of Mele [220] native phenothiazine drugs mixed with DNA at pH 5 leads to formation of an insoluble complex, presumably due to interaction of the negatively charged phosphate groups of DNA and the cationic groups of the side chains of the drugs. This precipitation phenomenon was confirmed in the present work, native CPZ, TFP, and MHP all forming insoluble complexes with CT-DNA and SS-DNA.

Computer Simulation

Since the X-band ESR spectra obtained in the present work possess a qualitative appearance different from that of the Q-band ESR spectra obtained for the CPZ/CT-DNA complex by Ohnishi and McConnell [209], it is of interest to generate computer simulated spectra of the random (no flow) orientation to better understand the observed ESR spectrum. The computer program [257] allows simulation for the theoretical case of axial symmetry for S = 1/2 with hyperfine splitting due to a single nucleus with I = 1. Figure 38 compares the results for X-band ($\nu \cong 9.4$ GHz) and Q-band ($\nu \cong 35$ GHz) ESR spectra using the magnetic parameters for DNA-bound CPZ given in Table XVI. The effects of varying the absorption line width (ΔH) in the program are illustrated for both cases. For $\Delta H = 0$ the program assumes a δ function for the absorption line width. The stick spectrum shown along with the X-band simulations is strictly

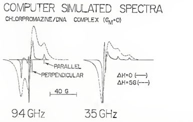

Figure 38 Computer simulated spectrum of the chlorpromazine radical cation complex with DNA (random orientation). Spectra on the left are for X-band ($\nu \cong 9.4$ GHz) and those on the right for Q-band ($\nu = 35$ GHz). The effects of varying the line width (ΔH) are illustrated in both cases. Stick spectrum of parallel and perpendicular lines in spectrum on the left is strictly qualitative in intensity relations and is intended to designate magnetic field positions of these lines more clearly.

qualitative in intensity relations and is intended to indicate field positions for parallel and perpendicular lines more clearly. Figure 39 shows the computer simulated X-band ESR spectra for random orientation of SS-DNA complexes of the radical cations of CPZ, TFP, and MMP. Clearly the line shapes observed experimentally are those expected on theoretical grounds. Comparison of the X-band and Q-band simulations in Figure 38 clearly demonstrates line shifts due to g-tensor effects and accounts for the difference in appearance of spectra obtained in the present work and those obtained by Ohnishi and McConnell [209]. Comparison of the simulated spectra for $\Delta H = 0$ in which the parallel and perpendicular lines are well resolved and for $\Delta H = 5$ G in which the perpendicular components are no longer resolved shows the effect of absorption line width on the spectrum.

It is worth noting that the computer simulated spectra, while indicating clearly that the experimentally observed spectra are those theoretically expected, do not provide an exact overlap. The general shapes and line positions are identical but relative intensities, resolutions and line widths are not rigidly equivalent. The computer simulations are sensitive to the value of $A_\perp$ and the fact that the closest correspondence to experimental spectra comes from using the $A_\perp$ values in Table XVI provides further confirmation of the validity of the estimation of $A_\perp$ from values of A_{iso} and $A_{||}$. The computer simulations are also very sensitive to the line width specified to the computer program. Using the magnetic parameters in Table XVI for CPZ, computer simulations were generated for ΔH values of 1, 2, 3, 4, 5, 6, 7, 8, 10, 15 and 20 G. The effect on the shape of the spectrum is striking; however, these results indicated that a line width of 5 to 6 G is appropriate for generating spectra very similar to those observed experimentally.

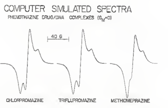

Figure 39 Computer simulated ESR spectra of the random orientation of complexes of the radical cations of chlorpromazine, triflupromazine, and methiomeprazine with salmon sperm DNA.

Like all spectroscopic lines, ESR lines have a finite width, the origins of which are complex [38-41,43,44,68-71,72-78]. Two basic processes can lead to broadening of ESR spectroscopic lines. Secular broadening is caused by processes that generate varying local magnetic fields, thereby altering slightly the energy separation between electron spin states. For a given microwave frequency a range of fields will be found at which resonance can occur and therefore a broad line is generated. The local variation in magnetic fields can be dynamic, that is, the paramagnetic entity experiences a time fluctuation in the local magnetic field, or spatial, that is, the local field may vary from one paramagnetic entity to another but remains constant for a given paramagnetic entity. Dynamic broadening is a homogeneous broadening and spatial broadening is an inhomogeneous broadening. In general homogeneous broadening leads to Lorentzian lineshapes and inhomogeneous broadening to Gaussian lineshapes. The second source of line broadening is lifetime broadening of quantum mechanical origin. Since a spin state has a finite lifetime, Δt, the energy of that state has a finite width, ΔE, determined by the Heisenberg uncertainty principle, that is,

$$\Delta E \Delta t \cong h/2\pi \,, \qquad (115a)$$

$$\Delta \nu \Delta t \cong 1/2\pi \,. \qquad (115b)$$

From the resonance condition, $h\nu = g\beta_e H$,

$$\Delta \nu = (g\beta_e/h)\Delta H \,, \qquad (116)$$

and, therefore,

$$\Delta H \cong h/2\pi g\beta_e \Delta t \,. \qquad (117)$$

Any process that increases the transition rate between the spin states decreases Δt and thereby increases the linewidth, ΔH. Lifetime broadening is homogeneous broadening because the process applies equally to all members of the spin system.

Inhomogeneous broadening can arise from anisotropic interactions in randomly oriented solid-state systems. In this case the local distribution of magnetic fields resulting from anisotropic g and hyperfine interactions leads to inhomogeneity and the line shape may be highly unsymmetrical. Unresolved hyperfine structure may also lead to inhomogeneous line broadening. In the present experiments only the ^{14}N hyperfine structure is resolved, and even here only the parallel component. Thus there is certainly the possibility of experimental line broadening due to unresolved nuclear hyperfine structure arising from protons on the phenothiazine ring, on the α-carbon of the 10-alkyl side chain, and even on the protons of the $-SCH_3$ group of MMP, as well as ^{19}F hyperfine interaction from the trifluoromethyl group of TFP. Furthermore, the DNA-bound drug systems are not truly solid-state systems but can be thought of as pseudopolycrystalline samples. The anisotropy of the random orientation is a consequence of the high viscosity of the solution as well as binding to the DNA helix. It is thus likely that slow tumbling of the molecules tends to average out the anisotropy somewhat, thereby leading to additional line broadening.

Experimentally it is important to use a modulation frequency, f_m, which is much less than the peak-to-peak derivative line width, ΔH_{pp} (expressed in frequency units as Δf_{pp}), that is,

$$\Delta f_m << \Delta f_{pp} = (g\beta_e/h)\Delta H_{pp} \tag{118}$$

A modulation frequency of 100 kHz (as used with the Varian E-3) can be used for linewidths as narrow as 0.1 G, but the same f_m will considerably distort lines less than 0.1 G. As the modulation amplitude, H_m, is gradually increased, the observed line width remains unchanged as long as $H_m << \Delta H_{pp}$. When H_m is close to ΔH_{pp}, the observed line begins to broaden and distort. When $H_m << \Delta H_{pp}$, the ESR signal amplitude increases linearly with H_m, whereas when $H_m > \Delta H_{pp}$, the signal decreases with increasing H_m. The ESR signal reaches a maximum near $H_m \cong 3\Delta H_{pp}$. When determining ESR spin concentrations and line shapes, it is best to have $H_m << \Delta H_{pp}$ and a practical criterion is to keep $H_m \leq \Delta H_{pp}/5$. When attempting to detect very weak signals, setting $H_m \cong 3\Delta H_{pp}$ suffices for maximum sensitivity. In the present experiments H_m was typically 3.2 G and the observed ΔH_{pp} at this modulation amplitude was about 15 G for perpendicular flow and 6 to 8 G for parallel flow. Thus H_m was roughly about $\Delta H_{pp}/5$ and experience showed that H_m near 3.2 G gave the best results. It should be noted, however, that long before the signal amplitude reaches a maximum, ΔH_{pp} is significantly increased. This is another source of line broadening in the experimental spectra. Furthermore, since $\Delta H_{pp} \cong 15$ G for the perpendicular line and $A_{||}$ is approximately the same magnitude, it is clear that there is considerable overlap of parallel and perpendicular components in the random orientation spectrum.

The preceding considerations indicate some of the reasons why perfect correlation between computer-simulated and experimental ESR spectra is not expected in the present work. Furthermore, it should be noted that the experimental spectrometer frequency is a program variable. The values of ν used are somewhat in error because the Varian E-3 is not equipped for reliable frequency measurements. This means that minor g-factor shifts can occur in the simulated spectra as compared to the experimental spectra, thereby altering the correspondence between calculation and experiment. Finally, it should be noted that the computer program used [257] employs a second-order perturbation treatment of the axial spin Hamiltonian and was originally designed (and is extensively used) to treat $^2\Sigma$ molecules, usually diatomic species studied via the matrix isolation technique applied to NbO (see Chapters I through V). Therefore, the correlation between computer-simulated spectra and observed spectra for DNA-bound phenothiazine drug radical cations is not expected to be perfect. What the computer simulations do establish, however, is that the random (no flow) orientation ESR spectrum of DNA-bound phenothiazine radical cations corresponds to the theoretical powder pattern ESR spectrum of a case with axial symmetry, $S = 1/2$, and a hyperfine splitting from one nucleus with $I = 1$. Thus the computer simulations are useful in better understanding the derivative spectra in the present work and are considered adequate for their intended purpose as they are, without the additional expense of trying to achieve a perfect match between simulated and observed spectra.

Concluding Remarks

The results of the present study may be summarized as follows. A flow system has been developed for use with the Varian E-3 ESR spectrometer which is useful in ascertaining whether or not planar aromatic radicals interact with double helical nucleic acids through an intercalative mode of binding. The apparatus has been used to demonstrate intercalation of the radical cations of the phenothiazine drugs chlorpromazine, triflupromazine, and methiomeprazine with calf thymus and salmon sperm DNA.

The development of these experimental techniques provides a convenient method which may be extended to further studies with other phenothiazine drugs or other paramagnetic intercalating agents. In addition, such a technique should prove useful in extended and inherently more interesting studies such as probing the interaction of phenothiazine drug radicals with chromatin, the DNA-protein complex found in the eukaryotic nucleus and which is active as a template for RNA synthesis [258].

APPENDIX A

DIAGONALIZATION OF THE NbO EFFECTIVE SPIN HAMILTONIAN

The effective spin Hamiltonian for the NbO molecule given by Eq (49) in Chapter III of the text is

$$(\mathcal{H}_{spin})_{op} = g_{\parallel}\beta_e H_z S_z + 2g_{\perp}\beta_e(H_x S_x + H_y S_y)$$

$$+ A_{\parallel} I_z S_z + 2A_{\perp}(I_x S_x + I_y S_y) \qquad (119)$$

This applies to the ESR transition $M_S = +1/2 \leftrightarrow M_S = -1/2$. S is taken to be 1/2 and z is identified with the symmetry axis of the molecule. Following a procedure first outlined by Bleaney [82] and considered thoroughly since in a number of references [72,80,258], the spin Hamiltonian in Eq. (119) can be rearranged to give a form diagonal in the Zeeman terms and which is convenient for interpretation of the experimental data. The Zeeman term is considered first.

Changing to another set of axes x', y', and z' such that z' is parallel to H, it is evident that

$$(\mathcal{H}_z)_{op} = g\beta_e H S'_z \qquad (120)$$

For a linear molecule the direction of H can be taken as the polar axis and θ the angle between z and H. Since y can arbitrarily be chosen orthogonal to H, y = y' and only x and z need be rotated. Since H_x = Hsinθ, H_z = Hcosθ, and H_y = 0.

$$(H_z)_{op} = \beta_e(g_{||}\cos\theta S_z + 2g_{\perp}\sin\theta S_x)H \qquad (121)$$

Choosing new direction cosines,

$$d_z = g_{||}\cos\theta/g \ , \qquad (122a)$$

$$d_x = 2g_{\perp}\sin\theta/g \ , \qquad (122b)$$

where $g = (g_{||}^2\cos^2\theta + 4g_{\perp}^2\sin^2\theta)^{1/2}$, then $(H_e)_{op}$ can be written as in Eq (123),

$$(H_z)_{op} = g\beta_e(d_zS_z + d_xS_x)H \ . \qquad (123)$$

A rotation of the coordinates of the electron then yields

$$(H_z)_{op} = g\beta_e S_z' H \ . \qquad (124)$$

where $S_z' = d_zS_z + d_xS_x$, $S_x' = -d_xS_z + d_zS_x$, and $S_y' = S_y$. For the nuclear hyperfine terms,

$$(H_{hf})_{op} = A_{||}S_zI_z + 2A_{\perp}(S_xI_x + S_yI_y) \ . \qquad (125)$$

$\bar{I}$ is rotated by

$$I_z = d_z^N I_z' - d_x^N I_x' \ , \qquad (126a)$$

$$I_x = d_x^N I_z' + d_z^N I_x' \ , \qquad (126b)$$

$$I_y = I_y' \ , \qquad (126c)$$

where the d_i^N are the direction cosines for the nuclear coordinate system relative to the electronic coordinates. By inverting the relations for S_z, S_x', and S_y', expressions for S_z, S_x, and S_y analogous to those in Eqs (126) are obtained. Substituting into Eq (125) and defining

$$d_z^N = A_{||}g_{||}\cos\theta/Ag, \qquad (127a)$$

$$d_x^N = 4A_{\perp}g_{\perp}\sin\theta/Ag\ , \qquad (127b)$$

where $A^2g^2 = A_{||}^2g_{||}^2\cos^2\theta + 16A_{\perp}^2g_{\perp}^2\sin^2\theta$, the following relation is obtained for Eq (119)

$$\begin{aligned}(H_{spin})_{sp} = {} & g\beta_e HS'_z + AI'_zS'_z + (2A_{||}A_{\perp}/A)I'_xS'_x \\ & + [(4A_{\perp}^2 - A_{||}^2)/A](2g_{||}g_{\perp}/g^2)\sin\theta\cos\theta I'_zS'_x \\ & + 2A_{\perp}I'_yS'_y \qquad (128)\end{aligned}$$

Dropping the primes and using the operators $S^+ = S_x + iS_y$ and $S^- = S_x - iS_y$, Eq (129) is obtained, which is diagonal in the Zeeman terms and identical to Eq (50) in Chapter III of the text.

$$\begin{aligned}(H_{spin})_{sp} = {} & g\beta_e HS_z + AI_zS_z + [(4A_{\perp}^2 - A_{||}^2)/A](2g_{||}g_{\perp}/g^2) \\ & \times \sin\theta\cos\theta I_zS_x + (A_{\perp}/2)[(A_{||} + A)/A] \\ & \times (I^+S^- + I^-S^+) + (A_{\perp}/2)[(A_{||} - A)/A] \\ & \times (I^+S^+ + I^-S^-) \qquad (129)\end{aligned}$$

Here g and A are the same as defined in the above discussion and in the text in Chapter III.

APPENDIX B

COMPUTER TECHNIQUES FOR THE NbO MOLECULE

The form of the effective spin Hamiltonian for NbO that is diagonal in the Zeeman terms has been discussed in Chapter III of the text and in Appendix A. A computer program was written to diagonalize this spin Hamiltonian and generate the appropriate eigenvalues and eigenvectors for the specific case of the NbO molecule with $S = 1/2$ and $I = 9/2$. The program consists of a driver routine to generate the spin Hamiltonian matrix elements which are given in tridiagonal form for $\theta = 90°$ to a diagonalization subroutine for computation of the eigenvalues and eigenvectors. The diagonalization subroutine was obtained from Carnahan, Luther, and Wilkes [260] and employs an iterative method, credited to Jacobi, for transforming a real symmetric matrix A into diagonal form. The method consists of applying to A a succession of plane rotations designed to reduce the off-diagonal elements to zero. That the method leads to the desired results was established by Forsythe and Henrici [261]. The original version of the program for treatment of the NbO molecule was written by Dr. J. M. Brom, Jr., to whom the author is deeply grateful. Extensive modifications to the original program were written by the author. Documentation of the program in the remainder of this appendix follows standard practice [260,262,263].

The subroutine implementing Jacobi's method for finding the eigenvalues and eigenvectors of an $n \times n$ real symmetric matrix A takes into account the symmetry of the starting matrix and its subsequent transformations so that calculations do not involve elements in the strictly lower triangular portion of A [260]. The starting matrix and all its subsequent transformations are denoted by the common symbol A, while the product of the successive orthogonal annihilation matrices is the matrix $T = IU_1U_2U_3 \ldots$; for each Jacobi iteration, each element in the strictly upper triangular portion of A is annihilated row by row in the order $a_{12}, a_{13}, \ldots, a_{1n}, a_{23}, a_{24}, \ldots, a_{2n}, a_{n-1,n}$. If an element a_{ij} is already smaller in magnitude than some value ϵ_2, it is simply ignored in the iterations. Before the first iteration the sum of squares S of all elements in the full matrix A is computed. The sum of the squares of the diagonal elements of A before and after each complete Jacobi iteration is computed and saved in σ_1 and σ_2, respectively. The criterion for ending the procedure is normally $[1 - (\sigma_1/\sigma_2)] < \epsilon_3$. At this point both σ_1 and σ_2 should almost equal S. An upper limit, k_{max}, is also placed on the total number of iterations. The eigenvalues $\lambda_1, \lambda_2, \ldots, \lambda_n$ are the diagonal elements of the final transformed matrix A. The elements of the corresponding eigenvectors are in successive columns of T. The flow diagram of the main program QSIGMA2 (see Figure 40) and the diagonalization subroutine EIGN (see Figure 41), the list of principal program variables (see Table XVIII) and the listing of the actual program given in this appendix are for the form of the program used most frequently, particularly in defining the θ versus H curves discussed in the text in Chapter III. In determining the precise values of the magnetic parameters of NbO from the initial estimates of the g- and A-values, an iterative calculation of the A-values is done by adding several statements to the main program at the point of return from the diagonalization subroutine. Since to a first approximation

$(h\nu)_{obs} \cong \lambda_{20} - \lambda_{10} = 2g_{\perp}\beta_e H_{\perp} + 2M_I A_{\perp}$ for the perpendicular lines, a quantity $Q = (\lambda_{20} - \lambda_{10}) + 9A_{\perp} - 2g_{\perp}\beta_e H_{\perp}$ can be defined for the $M_I = -9/2$ perpendicular line. The quantity Q can be calculated after diagonalization and a new value of $A_{\perp}$ obtained from

$$A_{\perp} = [Q + 2g_{\perp}\beta_e H_{\perp} - (\lambda_{20} - \lambda_{10})]/9 . \qquad (130)$$

A new value of $A_{||}$ can then be calculated from Kasai's expression [3] for the parallel resonances as discussed in the text in Chapter III. The new A-values are then used to generate new matrix elements and the entire diagonalization procedure starts again. Usually about five iterations are all that are required for convergence of the A-values for a given set of g-values.

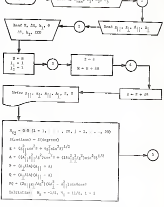
Begin
Read n, k_{max}, ϵ_1, ϵ_2, ϵ_3
1
Read $g_{||}$, $g_{\perp}$, $A_{||}$, $A_{\perp}$
2
Read H, ΔH, k_1, θ
$\Delta\theta$, k_2, ICD
$H \leftarrow H$
$I_1 = 1$
$I_2 = 1$
3
$\theta \leftarrow \theta$
$H \leftarrow H + \Delta H$
4
$\theta \leftarrow \theta + \Delta\theta$
Write $g_{||}$, $g_{\perp}$, $A_{||}$, $A_{\perp}$, θ, H
$H_{ij} = 0.0$ (i = 1, . . . , 20, j = 1, . . . , 20)
θ(radians) ← θ(degrees)
$g \leftarrow (g_{||}^2\cos^2\theta + 4g_{\perp}^2\sin^2\theta)^{1/2}$
$A \leftarrow ((A_{||}^2 g_{||}^2/g^2)\cos^2\theta + (16A_{\perp}^2 g_{\perp}^2/g^2)\sin^2\theta)^{1/2}$
$P \leftarrow (A_{\perp}/2A)(A_{||} + A)$
$Q \leftarrow (A_{\perp}/2A)(A_{||} - A)$
$PQ \leftarrow (2g_{||}g_{\perp}/Ag^2)(4A_{\perp}^2 - A_{||}^2)\sin\theta\cos\theta$
Initialize: $M_S = -1/2$, $M_I = 11/2$, i = 1
5

Figure 40 Flow diagram of program QS:C4A2 used to solve spin Hamiltonian matrix for YbO

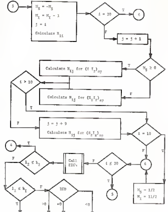

Figure 40 continued

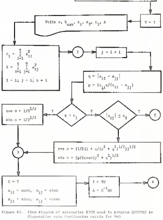
Enter
1
Input n, k_{max}, A, ε_1, ε_2, ε_3
T ← I
Write n, k_{max}, ε_1, ε_2, ε_3, A
$\sigma_1 \leftarrow \sum_{i=1}^{n} a_{ii}^2$
$S \leftarrow \sum_{i=1}^{n} \sum_{j=1}^{n} a_{ij}^2$
i = 1; j = 1, k = 1
2
j = i + 1
$q \leftarrow |a_{ii} - a_{jj}|$
$p \leftarrow 2a_{ij}q/(a_{ii} - a_{jj})$
T
$q < \varepsilon_1$
F
$|a_{ij}| \le \varepsilon_2$
T
2
$\cos\alpha \leftarrow 1/2^{1/2}$
$\sin\alpha \leftarrow 1/2^{1/2}$
3
$\cos\alpha \leftarrow (1/2(1 + q/(p^2 + q^2)^{1/2}))^{1/2}$
$\sin\alpha \leftarrow (p/2\cos\alpha(p^2 + q^2)^{1/2}$
U ← I
$u_{ii} \leftarrow \cos\alpha$, $u_{ij} \leftarrow \sin\alpha$
$u_{ji} \leftarrow \sin\alpha$, $u_{jj} \leftarrow -\cos\alpha$
T ← TU
$A \leftarrow U^{-1}AU$
4

Figure 41. Flow diagram of subroutine EIGN used in program QSIGMA2 to diagonalize spin Hamiltonian matrix for NbO

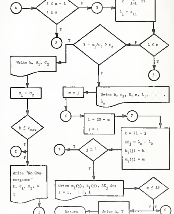
4
i ≤ n - 1
j ≤ n
F
5
$\sigma_2 \leftarrow \sum_{i=1}^{n} a_{ii}^2$
$\lambda_i \leftarrow a_{ii}$
T
2
T
$1 - \sigma_1/\sigma_2 > \varepsilon_e$
F
i ≤ n
T
5
Write k, σ_1, σ_2
F
$\sigma_1 \leftarrow \sigma_2$
m = 1
Write k, σ_2, S, n, λ_1, . λ_n
6
i = 20 - m
j = 1
7
$k \le k_{max}$
T
2
F
k = 21 - j
$\Delta E_j = \lambda_m - \lambda_k$
$k_1(j) = k$
$m_1(j) = m$
7
T
j ≤ i
F
Write 'No Convergence'
k, σ_1, σ_2, A
T
Write $m_1(j)$, $k_1(j)$, ΔE_j for j = 1, , i
m ≤ 19
F
T
6
1
Return
Write λ, T

Figure 41 continued

TABLE XVIII

FORTRAN Implementation: List of Principal Variables

Program Symbol	Definition
Main Program QSIGMA2	
A	Value of $[(A_{\parallel}^2 g_{\parallel}^2/g^2)\cos^2\theta + (16A_{\perp}^2 g_{\perp}^2/g^2)\sin^2\theta]^{1/2}$
ANGINC	Value by which θ is incremented (in degrees) for successive calculations
ANGLE	Initial value of θ (in degrees)
APAR	Value of $A_{\parallel}$ (in erg)
APER	Value of $A_{\perp}$ (in erg)
C	Value of $(g_{\parallel}^2\cos^2\theta + 4g_{\perp}^2\sin^2\theta)^{1/2}$
GPAR	Value of $g_{\parallel}$
GPER	Value of $g_{\perp}$
BFIELD	Value of magnetic field (in gauss) used in a particular calculation
BINC	Value (in gauss) by which magnetic field is incremented for successive calculations
BSPIN	Spin Hamiltonian matrix
BSTART	Initial value (in gauss) of magnetic field
ICD	Counter for program termination or continuation with new data set
K1	Counter for number of different values of magnetic field H to be used in calculations
K2	Counter for number of different values of θ to be used in calculations
P	Value of $(A_{\perp}/2)(A_{\parallel} + A)/A$
PQ	Value of $(2g_{\parallel}g_{\perp}/g)(4A_{\perp}^2 - A_{\parallel}^2)\sin\theta\cos\theta/A$
Q	Value of $(A_{\perp}/2)(A_{\parallel} - A)/A$

TABLE XVIII (continued)

Program Symbol	Definition
THETA	Value of θ (in degrees) used in a particular calculation
XMI	Value of M_I quantum number
XMS	Value of M_S quantum number
Diagonalization Subroutine EIGN	
A	Upper triangular matrix, A
AIK	Vector used for temporary storage
EIGEN	Vector of the eigenvalues
EPS1	Tolerance ε_1
EPS2	Tolerance ε_2; a_{ij} is bypassed if $\lvert a_{ij}\rvert < \varepsilon_2$
EPS3	Tolerance ε_3 used in termination criterion
ESR	Particular unique eigenvalue difference
ITER	Counter for number of complete Jacobi iterations
ITMAX	Maximum number of iterations permitted, k_{max}
N	Dimension n of the matrix A
OFFDSQ	Sum of squares of off-diagonal elements of A
S	Sum of squares of all elements in the full starting matrix
SIGMA1 SIGMA2	Sums, σ_1 and σ_2, of the squares of the diagonal elements of A before and after an iteration, respectively
T	Product of rotation matrices, ultimately contains eigenvectors

QSIGMA2 Program Listing

```
      IMPLICIT REAL*8(A-H,O-Z)
C
C
C     THIS PROGRAM IS USED TO CALCULATE ENERGY EIGENVALUES
C     AND ALL POSSIBLE UNIQUE DIFFERENCES BETWEEN THEM FOR
C     THE EXPLICIT CASE OF A QUARTET SIGMA GROUND ELECTRONIC
C     STATE MOLECULE WITH A HYPERFINE SPLITTING FROM A
C     NUCLEUS OF SPIN 9/2   FOR A GIVEN SET OF G AND A
C     VALUES, CALCULATIONS MAY BE DONE FOR ANY COMBINATION
C     OF RESONANCE FIELD POSITION AND ANGLE THETA,  WHERE
C     THETA IS THE ANGLE BETWEEN THE MOLECULAR AXIS AND
C     THE DIRECTION OF THE APPLIED MAGNETIC FIELD   THIS
C     PROGRAM WAS INITIALLY CONCEIVED TO TREAT THE CASE
C     OF THE DIATOMIC OXIDE NBO
C
C     REFERENCE: P H  KASAI, J  CHEM  PHYS, 49, 4979 (1968)
C
C
C     DATA INPUT INSTRUCTIONS
C
C     CARD 1   N, ITMAX                  FORMAT(2(12X,I3))
C
C              N = DIMENSION OF SPIN HAMILTONIAN MATRIX
C              ITMAX = NUMBER OF ITERATIONS ALLOWABLE FOR
C                      CONVERGENCE TEST IN DIAGONALIZATION
C                      OF SPIN HAMILTONIAN MATRIX
C
C     CARD 2   EPS1, EPS2, EPS3          FORMAT(3(21X,E9.2))
C
C              EPS1 = TOLERANCE USED IN DIAGONALIZATION
C                     SUBROUTINE
C              EPS2 = TOLERANCE USED IN DIAGONALIZATION
C                     SUBROUTINE
C              EPS3 = TOLERANCE USED IN DIAGONALIZATION
C                     SUBROUTINE
C
C     CARD 3:  GPAR, GPER, APAR, APER    FORMAT(4E15.7)
C
C              GPAR = VALUE OF G PARALLEL
C              GPER = VALUE OF G PERPENDICULAR
C              APAR = VALUE OF A PARALLEL IN ERGS
C              APER = VALUE OF A PERPENDICULAR IN ERGS
C
C     CARD 4:  HSTART, HINC, K1          FORMAT(2F10.4,I4)
C
C              HSTART = INITIAL VALUE OF MAGNETIC FIELD IN
C                       GAUSS
C              HINC = VALUE IN GAUSS BY WHICH MAGNETIC
C                     FIELD IS INCREMENTED FOR SUCCESSIVE
C                     CALCULATIONS
```

```
C               K1 = NUMBER OF DIFFERENT VALUES OF MAGNETIC
C                    FIELD THAT WILL BE USED IN CALCULATIONS
C
C       CARD 5  ANGLE, ANGINC, K2           FORMAT(2F10.2,I4)
C
C               ANGLE = INITIAL VALUE OF THETA IN DEGREES
C               ANGINC = VALUE IN DEGREES BY WHICH THETA IS
C                        INCREMENTED FOR SUCCESSIVE CALCULATIONS
C               K2 = NUMBER OF DIFFERENT VALUES OF THETA
C                    THAT WILL BE USED IN CALCULATIONS
C
C       CARD 6: ICD                         FORMAT(I2)
C
C               IF (ICD.LT.0)   PROGRAM TERMINATES
C               IF (ICD.EQ.0)   NEW VALUES OF HSTART AND
C                               ANGLE ARE READ BUT PREVIOUS
C                               SET OF C AND A VALUES WILL
C                               BE USED IN CALCULATIONS
C               IF (ICD.GT.0)   NEW G AND A VALUES ARE READ
C                               AND THE SAME OR NEW VALUES
C                               OF HSTART AND ANGLE MUST BE
C                               READ IN IMMEDIATELY THEREAFTER
C
C
C
        DIMENSION HSPIN(20,20)
C
C       READ DATA AND WRITE MAGNETIC PARAMETERS
C
        READ(5,100) N,ITMAX,EPS1,EPS2,EPS3
      1 READ(5,101) GPAR,GPER,APAR,APER
      2 READ(5,102) HSTART,HINC,K1
        READ(5,102) ANGLE,ANGINC,K2
        READ(5,103) ICD
        HFIELD=HSTART
        DO 9 LONE=1,K1
        THETA1=ANGLE
        HFIELD=HFIELD+HINC
        DO 9 LTWO=1,K2
        THETA1=THETA1+ANGINC
        WRITE(6,104) GPAR,GPER,APAR,APER,THETA1,HFIELD
C
C       INITIALIZE SPIN HAMILTONIAN MATRIX ELEMENTS TO ZERO
C
        DO 3 I=1,20
        DO 3 J=1,20
      3 HSPIN(I,J)=0.0
C
C       CONVERT THETA FROM DEGREES TO RADIANS
C
        THETA=THETA1*0.017453292519943
C
C       CALCULATE KASAI'S C
```

```
      GC=GPAR*DCOS(THETA)
      GS=2.*GPER*DSIN(THETA)
      GG=GC*GC+GS*GS
      G=DSQRT(GG)
C
C     CALCULATE KASAI'S A
C
      AGC=APAR*GC
      AGS=APAR*GS*Z
      AA=(AGC*AGC+AGS*AGS)/GG
      A=DSQRT(AA)
C
C     CALCULATE COEFFICIENTS FOR I AND S LADDER
C     OPERATOR TERMS IN SPIN HAMILTONIAN
C
      P=(APER/(2.*A))*(APAR+A)
      Q=(APER/(2.*A))*(APAR-A)
C
C     CALCULATE CROSS TERM SIN(THETA)COS(THETA) IN SPIN
C     HAMILTONIAN.  THIS CROSS TERM (PQ) NECESSARY FOR
C     THETA NOT 0 OR 90 DEGREES
C
      PQ=2.*GPAR*GPER*DSIN(THETA)*DCOS(THETA)*(4.*APER*
     1APER-APAR*APAR)/(A*G*G)
C
C     INITIAL VALUES FOR ELECTRON AND NUCLEAR SPIN
C     QUANTUM NUMBERS
C
      XMS=-0.5
      XMI=5.5
C
C     CALCULATE ELEMENTS OF SPIN HAMILTONIAN MATRIX
C     HSPIN(I,J).  THIS DO LOOP GENERATES MATRIX ELEMENTS
C     (I,I) AND (I,I+1)
C
      DO 4 I=1,20
      XMS=-XMS
      XMI=XMI-1.0
      J=I
C
C     CALCULATE DIAGONAL ELEMENTS
C
      HSPIN(I,J)=G*9.27410D-21*HFIELD*XMS +A*XMS*XMI
C
C     ELIMINATE CONSTANT FACTOR IN ALL MATRIX ELEMENTS
C
      HSPIN(I,J)=1.0D+16*HSPIN(I,J)
C
      IF(I.EQ.20) GO TO 4
      J=J+1
C
C     CALCULATE OFF-DIAGONAL ELEMENTS
C
      STEP1=DSQRT(24.75-XMI*(XMI-1.0))
      IF(XMS)6,5,5
    5 HSPIN(I,J)=Q*STEPI
C
C     ELIMINATE CONSTANT FACTOR IN ALL MATRIX ELEMENTS
C
      HSPIN(I,J)=1.0D+16*HSPIN(I,J)
C
      GO TO 7
    6 HSPIN(I,J)=P*STEPI
C
C     ELIMINATE CONSTANT FACTOR IN ALL MATRIX ELEMENTS
C
      HSPIN(I,J)=1.0D+16*HSPIN(I,J)
C
    7 IF(I.GT.10) GO TO 77
      J=J+9
      HSPIN(I,J)=PQ*XMI*0.5D+16
   77 IF(I.EQ.10) GO TO 8
      GO TO 4
    8 XMS=0.5
      XMI=5.5
    4 CONTINUE
C
C     CALL DIAGONALIZATION SUBROUTINE EIGN
C
      CALL EIGN(HSPIN,N,ITMAX,EPS1,EPS2,EPS3)
    9 CONTINUE
C
C     INSTRUCTIONS FOR READING NEXT SET OF DATA OR
C     TERMINATING PROGRAM
C
      IF(ICO)10,2,1
C
C     FORMATS FOR I/O STATEMENTS
C
  100 FORMAT(2(12X,I3)/3(11X,E9.2))
  101 FORMAT(4E15.7)
  102 FORMAT(2F10.4,I4)
  103 FORMAT(I2)
  104 FORMAT(1H1,/////,4X,
     1'CALCULATIONS FOR QUARTET SIGMA MOLECULES',//4X,
     2'RESULTS FOR SPECIFIC MAGNETIC PARAMETERS",//7X,
     3'(1)  SPIN HAMILTONIAN MATRIX',/7X,
     4'(2)  EIGENVALUES AND EIGENVALUE DIFFERENCES',/7X,
     5'(3)  FINAL TRANSFORMED SPIN HAMILTONIAN MATRIX',/7X,
     6'(4)  EIGENVECTOR MATRIX',
     7        ////4X,'**********************************
     1**********************',/4X,'*
     2                        *',/4X,'*  GPAR = ',F15.7,10
     3X'GPER = ',E15.7,'  *',/4X,'*
     4                        *',/4X,'*  APAR = ',E15.7,10X,'
     5APER = ',E15.7,'  *',/4X,'*
     6                        *',/4X,'*  THETA = ',F14.2,10X,'
     7HFIELD = ',F13.2,'  *',/4X,'*
     8                    *',/4X,'************************
     9*************************',/////)
  10 STOP
     END

     SUBROUTINE EIGN(A,N,ITMAX,EPS1,EPS2,EPS3)
C
C
C    EIGENVALUES AND EIGENVECTORS BY THE JACOBI METHOD
C
C    ONLY THE UPPER TRIANGULAR PART OF THE REAL SYMMETRIC
C    STARTING MATRIX A IS READ.  T IS AN N BY N ORTHOGONAL
C    MATRIX, BEING THE PRODUCT OF THE SEQUENCE OF TRANS-
C    FORMATION MATRICES USED TO ANNIHILATE SUCCESSIVELY
C    THE OFF-DIAGONAL ELEMENTS OF A, AND CONSEQUENTLY TO
C    REDUCE A ITERATIVELY TO NEAR-DIAGONAL FORM.  SIGMA1
C    AND SIGMA2 ARE THE VALUES OF SIGMA A(I,I)**2 BEFORE
C    AND AFTER ONE COMPLETE ITERATION.  SINCE ANNIHILATION
C    OF AN ELEMENT MAY CAUSE ANOTHER ALREADY ANNIHILATED
C    ELEMENT TO ASSUME A NON-ZERO VALUE, THE ITERATIVE
C    PROCESS IS REPEATED UNTIL THE CONVERGENCE TEST IS
C    PASSED(1-SIGMA1/SIGMA2 LESS THAN EPS3) OR ITMAX COM-
C    PLETE ITERATIONS HAVE FAILED TO PRODUCE CONVERGENCE.
C    AN OFF-DIAGONAL ELEMENT SMALLER IN MAGNITUDE THAN
C    EPS2 IS IGNORED IN THE ANNIHILATION PROCESS.  EPS1
C    IS COMPARED WITH (A(I,I)-A(J,J)) TO DETERMINE THE
C    METHOD OF COMPUTING SCS AND SNA,  THE COSINE AND SINE
C    OF THE ROTATION ANGLE, RESPECTIVELY.  WHEN A HAS BEEN
C    REDUCED TO DIAGONAL FORM, THE EIGENVALUES WILL BE
C    FOUND IN THE DIAGONAL POSITIONS AND ARE SAVED IN
C    EIGEN(1)...EIGEN(N).  THE ASSOCIATED EIGENVECTORS
C    ARE IN CORRESPONDING COLUMNS OF THE FINAL TRANSFOR-
C    MATION MATRIX T.  S IS THE SUM OF THE SQUARES OF ALL
C    ELEMENTS IN THE ORIGINAL MATRIX A, AND SHOULD BE
C    THEORETICALLY EQUAL TO THE VALUE OF SIGMA2.
C
C    REFERENCE FOR SUBROUTINE EIGN:  B. CARNAHAN, H. A.
C    LUTHER, AND J. O. WILKES, APPLIED NUMERICAL METHODS,
C    NEW YORK:  JOHN WILEY & SONS, INC., 1969, PP. 250-260.
C
C
     IMPLICIT REAL*8(A-H,O-Z)
     DIMENSION A(20,20),T(20,20),AIK(20),EIGEN(20)
     DIMENSION ESR(20),KONE(20),MONE(20)
C
C    READ PARAMETERS
C
     DO 2 I=1,20
     DO 2 J=1,20
   2 T(I,J)=0.0
     NM1=N-1
     WRITE(6,201) N,ITMAX,EPS1,EPS2,EPS3
     WRITE(6,2011)
```

```
      DO 3 I=1,N
    3 WRITE(6,202) (A(I,J),J=1,N)
C
C     SET UP INITIAL MATRIX T AND COMPUTE SIGMA1 AND S
C
      SIGMA1=0.0
      OFFDSQ=0.0
      DO 5 I=1,N
      SIGMA1=SIGMA1+A(I,I)**2
      T(I,I)=1.0
      IP1=I+1
      IF(I.GE.N) GO TO 6
      DO 5 J=IP1,N
    5 OFFDSQ=OFFDSQ+A(I,J)**2
    6 S=2.0*OFFDSQ+SIGMA1
C
C     BEGIN JACOBI ITERATION
C
      DO 26 ITER=1,ITMAX
      DO 20 I=1,NM1
      IP1=I+1
      DO 20 J=IP1,N
      Q=DABS(A(I,I)-A(J,J))
C
C     CALCULATE SINE AND COSINE OF ROTATION ANGLE
C
      IF(Q.LE.EPS1) GO TO 9
      IF(DABS(A(I,J)).LE.EPS2)GO TO 20
      P=2.0*A(I,J)*Q/(A(I,I)-A(J,J))
      SPQ=DSQRT(P*P+Q*Q)
      CSA=DSQRT((1.0+Q/SPQ)/2.0)
      SNA=P/(2.0*CSA*SPQ)
      GO TO 10
    9 CSA=1.0/DSQRT(2.0D0)
      SNA=CSA
   10 CONTINUE
C
C     UPDATE COLUMNS I AND J OF T, EQUIVALENT TO
C     MULTIPLICATION BY THE ANNIHILATION MATRIX
C
      DO 11 K=1,N
      HOLDKI=T(K,I)
      T(K,I)=HOLDKI*CSA+T(K,J)*SNA
   11 T(K,J)=HOLDKI*SNA-T(K,J)*CSA
C
C     CALCULATE NEW ELEMENTS OF A IN ROWS I AND J
C
      DO 16 K=I,N
      IF(K.GT.J) GO TO 15
      AIK(K)=A(I,K)
      A(I,K)=CSA*AIK(K)+SNA*A(K,J)
      IF(K.NE.J) GO TO 14
      A(J,K)=SNA*AIK(K)-CSA*A(J,K)
   14 GO TO 16
   15 HOLDIK=A(I,K)
      A(I,K)=CSA*HOLDIK+SNA*A(J,K)
      A(J,K)=SNA*HOLDIK-CSA*A(J,K)
   16 CONTINUE
C
C     CALCULATE NEW ELEMENTS OF A IN COLUMNS I AND J
C
      AIK(J)=SNA*AIK(I)-CSA*AIK(J)
C
C     WHEN K IS LARGER THAN I
C
      DO 19 K=1,J
      IF(K.LE.I) GO TO 18
      A(K,J)=SNA*AIK(K)-CSA*A(K,J)
      GO TO 19
   18 HOLDKI=A(K,I)
      A(K,I)=CSA*HOLDKI+SNA*A(K,J)
      A(K,J)=SNA*HOLDKI-CSA*A(K,J)
   19 CONTINUE
   20 A(I,J)=0.0
C
C     FIND SIGMA2 FOR TRANSFORMED A AND TEST FOR
C     CONVERGENCE
C
      SIGMA2=0.0
      DO 21 I=1,N
      EIGEN(I)=A(I,I)
   21 SIGMA2=SIGMA2+EIGEN(I)**2
      IF(1.0-SIGMA1/SIGMA2.GE.EPS3) GO TO 25
      WRITE(6,205) ITER,SIGMA2,S,N
      WRITE(6,2051)
      WRITE(6,211) (I,EIGEN(I),I=1,N)
      WRITE(6,209)
C
C     THIS DO LOOP CALCULATES AND WRITES ALL POSSIBLE
C     UNIQUE EIGENVALUE DIFFERENCES FOR ELECTRON SPIN
C     RESONANCE TRANSITIONS.
C
      DO 22 M=1,19
      NUTS=20-M
      DO 221 J=1,NUTS
      K=21-J
      ESR(J)=EIGEN(M)-EIGEN(K)
      KONE(J)=K
  221 MONE(J)=M
      WRITE(6,210) (MONE(J),KONE(J),ESR(J),J=1,NUTS)
   22 CONTINUE
C
C
      WRITE(6,206)
      DO 23 I=1,N
   23 WRITE(6,202) (A(I,J),J=1,N)
      WRITE(6,207)
      DO 24 I=1,N
   24 WRITE(6,202) (T(I,J),J=1,N)
      RETURN
   25 WRITE(6,203) ITER,SIGMA1,SIGMA2
   26 SIGMA1=SIGMA2
C
C     IF ITER EXCEEDS ITMAX:  NO CONVERGENCE
C
      WRITE(6,204) ITER, S, SIGMA1,SIGMA2
      DO 27 I=1,N
   27 WRITE(6,202) (A(I,J),J=1,N)
      WRITE(6,208)
      DO 28 I=1,N
   28 WRITE(6,202) (T(I,J)J=1,N)
      RETURN
C
C     FORMATS FOR I/O STATEMENTS
C
  201 FORMAT(/,4X,49('*'),/,4X,'*',47(' '),'*',/,4X,
     1'* DETERMINATION OF EIGENVALUES BY JACOBI METHOD *',
     2/4X,'*',47(' '),'*',/,4X,'*  N = ',I4,32(' '),'*',/,
     34X,'*  ITMAX = ',I4,32(' '),'*',/,4X'*  EPS1 = ',
     4E12.3,24(' '),'*',/,4X,'*  EPS2 = ',E12.3,24(' '),
     5'*',/,4X,'* EPS3 = ',E12.3,24(' '),'*',/,4X,'*',
     647(' '),'*',/,4X,49('*'))
 2011 FORMAT(1H1,//4X,'THE SPIN HAMILTONIAN MATRIX IS',
     1/4X,30('-'),//)
  202 FORMAT(1X,8E15.7/1X,8E15.7/1X,4E15.7///)
  203 FORMAT(//,6X,'ITER = ',I5,10X,'SIGMA1 = ',E15.7,10X,
     1'SIGMA2 = ',E15.7)
  204 FORMAT(///,4X,'NO CONVERGENCE WITH',//,6X,'ITER = ',
     1I5,5X,'S = ',E15.7,5X,'SIGMA1 = ',E15.7,5X,'SIGMA2 = '
     2,E15.7,//,5X,'THE CURRENT SPIN HAMILTONIAN MATRIX IS'
     3,//)
  205 FORMAT(///,4X,'CONVERGENCE HAS OCCURRED WITH ',//,6X,
     1'ITER = ',I5,5X,'SIGMA2 = ',E15.7,5X,'S = ',E15.7,5X,
     2'N = ',I5)
 2051 FORMAT(1H1,//4X,'THE EIGENVALUES EIGEN(1)...,EIGEN(N)
     1 ARE',/4X,39('-'),//)
  206 FORMAT(1H1,//4X,'THE FINAL TRANSFORMED SPIN HAMILTONIAN
     1 MATRIX IS',/4X,48('-'),//)
  207 FORMAT(1H1,4X,'EIGENVECTORS ARE IN CORRESPONDING
     1COLUMNS OF THE FOLLOWING T MATRIX',/,5X,67('-'),//)
  208 FORMAT(1H0,4X,'THE CURRENT T MATRIX IS'/1H)
  209 FORMAT(1H1,///5X,'UNIQUE EIGENVALUE DIFFERENCES:
     1POSSIBILITIES FOR ESR TRANSITIONS',/5X,65('-'),///)
  210 FORMAT(3(5X,I2,'-',I2,' ESR = ',E15.7))
  211 FORMAT(10X,'EIGENVALUE (',I2,') = ',E15.7)
      END
```

BIBLIOGRAPHY

1 T.M. Dunn, in Molecular Spectroscopy: Modern Research, edited by K.N. Rao and C.W. Mathews, New York: Academic, 1972, p. 231 ff.

2 D.W. Green, W. Korfmacher and D.M. Gruen, J. Chem. Phys. 58, 404 (1973).

3 P.H. Kasai, J. Chem. Phys. 49, 4979 (1968).

4 D. Premaswarup and R.F. Barrow, Nature 180, 602 (1957).

5 C.J. Cheetham and R.F. Barrow, Trans. Far. Soc. 63, 1835 (1967)

6 W. Weltner, Jr. and D. McLeod, Jr., J. Chem. Phys. 42, 882 (1965).

7 W. Weltner, Jr. and D. McLeod, Jr., J. Phys. Chem. 69 3488 (1965).

8 V.R. Rao, Ind. J. Phys. 24, 35 (1950)

9 U. Uhler, Arkiv Fysik 8, 265 (1954).

10 W. Weltner, Jr., Science 155, 155 (1967).

11 D.S. Birney, Modern Astronomy, Boston: Allyn and Bacon, 1969.

12 L.H. Aller, Astrophysics, The Atmospheres of the Sun and Stars, 2nd Edition, New York: Ronald, 1963.

13 Stellar Atmospheres, edited by J.L. Greenstein, Chicago: University of Chicago, 1960.

14 B.E. Turner, Sci. Amer. 228 (3), 51 (1973).

15 D.N. Davis and P.C. Keenan, Publ. Astron. Soc. Pac. 81, 230 (1969).

16 W. Espe, Materials of High Vacuum Technology, Volume I, Metals and Metalloids, New York: Pergamon, 1966.

17 Handbook of Chemistry and Physics, 46th Edition, Cleveland: Chemical Rubber Co., 1965

18 F. Rosebury, Handbook of Electron Tube and Vacuum Techniques, Reading, Massachusetts: Addison Wesley, 1965

19 E. Frieden, Sci. Amer. 227(1), 52 (1972)

20 W. Weltner, Jr. Adv. High Temp. Chem. 2, 85 (1969)

21. A.M. Bass and H.P. Broida, *Formation and Trapping of Free Radicals*, New York: Academic, 1960.

22. M.E. Jacox and D.E. Milligan, Appl. Opt. 3, 873 (1964).

23. J.W. Hastie, R.H. Hauge and J.L. Margrave, in *Spectroscopy in Inorganic Chemistry*, Volume 1, edited by C.N.R. Rao and J.R. Ferraro, New York: Academic, 1970.

24. L. Andrews, Ann. Rev. Phys. Chem. 22, 109 (1971).

25. W. Weltner, Jr., and J.R.W. Warn, J. Chem. Phys. 37, 292 (1962).

26. M.J. Linevsky, J. Chem. Phys. 34, 587 (1961).

27. P.H. Kasai, E.B. Whipple and W. Weltner, Jr., J. Chem. Phys. 44, 2581 (1966).

28. W. Weltner, Jr., D. McLeod, Jr. and P.H. Kasai, J. Chem. Phys. 46, 3172 (1967).

29. L.B. Knight, Jr., W.C. Easley and W. Weltner, Jr., J. Chem. Phys. 52, 1489 (1970).

30. W.C. Easley and W. Weltner, Jr., J. Chem. Phys. 52, 1489 (1970).

31. L.B. Knight, Jr., W.C. Easley and W. Weltner, Jr., J. Chem. Phys. 54, 1610 (1971).

32. L.B. Knight, Jr. and W. Weltner, Jr., J. Chem. Phys. 54, 3875 (1971).

33. L.B. Knight, Jr. and W. Weltner, Jr., J. Chem. Phys. 55, 2061 (1971).

34. L.B. Knight, Jr., J.M. Brom, Jr. and W. Weltner, Jr., J. Chem. Phys. 56, 1152 (1972).

35. J.M. Brom, Jr. and W. Weltner, Jr., J. Chem. Phys. 57, 3379 (1972).

36. J.M. Brom, Jr., W.R.M. Graham and W. Weltner, Jr., J. Chem. Phys. 57, 4116 (1972).

37. R.F. Barrow, in *Essays in Structural Chemistry*, edited by A.J. Downs, D.A. Long and L.A.K. Staveley, London: Macmillan, 1971, p. 383 ff.

38. P.B. Ayscough, *Electron Spin Resonance in Chemistry*, London: Methuen, 1967.

39. R.S. Alger, *Electron Paramagnetic Resonance: Techniques and Applications*, New York: Wiley-Interscience, 1968.

40. C.P. Poole, Jr., *Electron Spin Resonance*, New York: Wiley-Interscience, 1967.

41. A. Carrington and A.D. McLachlan, *Introduction to Magnetic Resonance*, New York: Harper & Row, 1967.

42. J.H. Freed, Ann. Rev. Phys. Chem. 23, 265 (1972)

43. C.P. Slichter, *Principles of Magnetic Resonance*, New York: Harper & Row, 1963

44. J.E. Wertz and J.R. Bolton, *Electron Spin Resonance*, New York: McGraw-Hill, 1972

45. B. Taylor, W. Parker and D. Langenberg, Rev. Mod. Phys. 41, 375 (1969).

46. H.R. Crane, Sci. Amer. 218 (1), 72 (1968).

47. J. Berkowitz, W.A. Chupka and M.G. Inghram, J. Chem. Phys. 27, 87 (1957)

48. M.G. Inghram, W.A. Chupka and J. Berkowitz, J. Chem. Phys. 27, 569 (1957)

49. A.V. Lapitskii, Y.P. Simanov and E.P. Artamonova, Zh. Neorgan. Khim. 2, 80 (1957), English translation, p. 122

50. S.I. Alyamovskii, G.P. Shveikin and P.V. Gel'd, Zh. Neorgan. Khim. 3, 2437 (1958), English translation, p. 6

51. Chem. Abstr. 55, 1116b (1961), abstract of I.V. Golubtsov, A.V. Lapitskii and V.K. Shiryaev, Izvest. Vysshikh Ucheb. Zavedenii, Khim. i Khim. Tekhnol. 3, 571 (1960)

52. S.A. Shchukarev, G.A. Semenov and K.E. Frantseva, Zh. Neorgan. Khim. 11, 233 (1966), English translation, p. 129.

53. A. Taylor and N.J. Doyle, J. Less-Common Metals 13, 313 (1967).

54. E.A. Gulbransen, Corrosion (NACE) 26, 19 (1970).

55. A. Reisman and F. Holtzberg, in *High Temperature Oxides, Part II, Oxides of the Rare Earths, Titanium, Zirconium, Hafnium, Niobium, and Tantalum*, edited by A.M. Alper, New York: Academic, 1970, p. 217 ff.

56. J.L. Margrave, *The Characterization of High-Temperature Vapors*, New York: Wiley, 1967.

57. C.K. Jen, S.N. Foner, E.L. Cochran and V.A. Bowers, Phys. Rev. 112, 1169 (1958)

58. W. Weltner, Jr., P.N. Walsh and C.L. Angell, J. Chem. Phys. 40, 1299 (1964)

59. W. Weltner, Jr. and D. McLeod, Jr., J. Chem. Phys. 40, 1305 (1964).

60. W. Weltner, Jr. and D. McLeod, Jr., J. Chem. Phys. 45, 3096 (1966).

61. W.C. Easley and W. Weltner, Jr., J. Chem. Phys. 52, 197 (1970).

62. G.W. Ewing, Instrumental Methods of Chemical Analysis, 3rd Edition, New York: McGraw-Hill, 1969, Table 5-2, p. 127.

63. H.H. Willard, L.L. Merritt, Jr., and J.A. Dean, Instrumental Methods of Analysis, 4th Edition, Princeton, New Jersey: Van Nostrand, 1965, Table 5-1, p. 128.

64. J.S. Griffith, The Theory of Transition Metal Ions, Cambridge: Cambridge University, 1961.

65. A. Abragam and M.H.L. Pryce, Proc. Roy. Soc. 205, 135 (1951).

66. B.A. Goodman and J.B. Raynor, Adv. Inorg. Chem. Radiochem. 13, 135 (1970).

67. R.M. Assenheim, Introduction to Electron Spin Resonance, New York: Plenum, 1966.

68. C.P. Poole, Jr. and H.A. Farach, The Theory of Magnetic Resonance, New York: Wiley-Interscience, 1972.

69. S.A. Al'tshuler and B.M. Kozyrev, Electron Paramagnetic Resonance, New York: Academic, 1964.

70. J.D. Memory, Quantum Theory of Magnetic Resonance Parameters, New York: McGraw-Hill, 1968.

71. A. Abragam and B. Bleaney, Electron Paramagnetic Resonance of Transition Ions, London: Oxford University, 1970.

72. W. Low, Paramagnetic Resonance in Solids, New York: Academic, 1960.

73. I.N. Levine, Quantum Chemistry, Volume II, Boston: Allyn and Bacon, 1970.

74. Paramagnetic Resonance, Volumes I and II, edited by W. Low, New York: Academic, 1963.

75. Electron Paramagnetic Resonance, edited by S. Geschwind, New York: Plenum, 1972.

76. H.M. Swartz, J.R. Bolton and D.C. Borg, Biological Applications of Electron Spin Resonance, New York: Wiley-Interscience, 1972.

77. D.J.E. Ingram, Biological and Biochemical Applications of Electron Spin Resonance, New York: Plenum, 1969.

78. G.E. Pake, Paramagnetic Resonance, New York: Benjamin, 1962.

79. S.P. McGlynn, T. Azumi and M. Kinoshita, Molecular Spectroscopy of the Triplet State, Englewood Cliffs, New Jersey: Prentice-Hall, 1969.

80. Hyperfine Interactions, edited by A.J. Freeman and R.B. Frankel, New York: Academic, 1967.

81. B. Bleaney, Proc. Roy. Soc. 63, 407 (1950).

82. B. Bleaney, Phil. Mag. 42, 441 (1951).

83. R.H. Sands, Phys. Rev. 99, 1222 (1955).

84. D.S. O'Reilly, J. Chem. Phys. 29, 1188 (1958).

85. J.W. Searl, R.C. Smith and S.J. Wyard, Proc. Phys. Soc. 74, 491 (1959).

86. B. Bleaney, Proc. Phys. Soc. 75, 621 (1960).

87. E.M. Roberts and W.S. Koski, J. Amer. Chem. Soc. 82, 3006 (1960).

88. P.K. Kneubuhl, J. Chem. Phys. 33, 1074 (1960).

89. R. Neiman and D. Kivelson, J. Chem. Phys. 35, 156 (1961).

90. J.A. Ibers and J.D. Swalen, Phys. Rev. 127, 1914 (1962).

91. M.R. Gersmann and J.D. Swalen, J. Chem. Phys. 36, 3221 (1962).

92. J.D. Swalen and H.M. Gladney, IBM J. Res. Develop. 8, 515 (1964).

93. T.S. Johnston and H.G. Hecht, J. Mol. Spec. 17, 98 (1965).

94. M.M. Malley, J. Mol. Spec. 17, 210 (1965).

95. L.D. Rollmann and S.I. Chan, J. Chem. Phys. 50, 3416 (1969).

96. J.C. Eisenstein and M.H.L. Pryce, Proc. Roy. Soc. 229, 20 (1955).

97. M.W.P. Strandberg, Microwave Spectroscopy, London: Methuen, 1954, Chapter 11.

98. B. Mile, Angew. Chem. 7, 507 (1968).

99. R.L. Morehouse, J.J. Christiansen and W. Gordy, J. Chem. Phys. 45, 1751 (1966).

100. F.J. Adrian, E.L. Cochran and V.A. Bowers, J. Chem. Phys. 47, 5441 (1967).

101. J.W. Searl, R.C. Smith and S.J. Wyard, Proc. Phys. Soc. 78, 1174 (1961).

102. The International Dictionary of Applied Mathematics, edited by W.F. Freiberger, New York: Van Nostrand, 1960.

103. C.H. Townes and A.L. Schawlow, Microwave Spectroscopy, New York: McGraw-Hill, 1955, p. 225 ff.

104. W. Gordy and R.L. Cook, Microwave Molecular Spectra, 2nd Edition, Wiley-Interscience, New York, 1970, p. 551 ff.

105. E. A. C. Lucken, Nuclear Quadrupole Coupling Constants, New York: Academic, 1969

106. B. Bleaney, Physica 17, 175(1951).

107. H. Kopfermann, Nuclear Moments, New York: Academic, 1958

108. R. A. Frosch and H. M. Foley, Phys. Rev. 88, 1337 (1952)

109. E. Fermi, Z. Physik 60, 320 (1930).

110. C. F. Fischer, Tabulation of Hartree-Fock Results, Vancouver: University of British Columbia, 1968.

111. S. Goudsmit, Phys. Rev. 43, 636 (1933)

112. R. G. Barnes and W. V. Smith, Phys. Rev. 93, 95 (1954).

113. C. E. Moore, Atomic Energy Levels, Washington, D.C.: Natl. Bur. Std. U.S., Circ. 467, 1949.

114. R. A. Berg and O. Sinanoglu, J. Chem. Phys. 32, 1082 (1960).

115. J.T. Hougen, G.E. Leroi and T.C. James, J. Chem. Phys. 34, 1670 (1961)

116. C.K. Jørgensen, Mol. Phys. 7, 417 (1964)

117. G. Herzberg, Atomic Spectra and Atomic Structure, New York: Dover, 1944

118. G. Herzberg, Molecular Spectra and Molecular Structure I. Spectra of Diatomic Molecules, 2nd Edition, New York: van Nostrand, 1950

119. E.U. Condon and G.H. Shortley, The Theory of Atomic Spectra, Cambridge: Cambridge University, 1957

120. R.E. Robertson and H.M. McConnell, J. Chem. Phys. 64, 70 (1960).

121. R.L. Belford, J. Chem. Phys. 34, 318 (1961).

122. K.D. Carlson and C. Moser, J. Phys. Chem. 67, 2644 (1963)

123. M.H.L. Pryce, Proc. Phys. Soc. 63, 25 (1950)

124. A.J. Stone, Proc. Roy. Soc. 271, 424 (1963).

125. W. Weltner, Jr. and D. McLeod, Jr., J. Mol. Spec. 17, 276 (1965)

126. A. Lagerqvist and I.-E. Selin, Arkiv Fysik 12, 663 (1957).

127. V.R. Rao and D. Premaswarup, Ind. J. Phys. 27, 393 (1963).

128. International Tables of Selected Constants, Spectroscopic Data Relative to Diatomic Molecules, edited by B. Rosen, New York: Pergamon, 1970

129. R.S. Mulliken, Rev. Mod. Phys. 2, 60 (1930).

130. R.S. Mulliken, Phys. Rev. 57, 500 (1940).

131. L. Veseth, J. Phys. B6, 1473 (1973).

132. L. Veseth, J. Phys. B6, 1484 (1973).

133. S.H. Snyder, S.P. Banerjee, H.I. Yamamura and D. Greenberg, Science 184, 1243 (1974).

134. J.C. Krantz, Jr., C.J. Carr and B.N. LaDu, Jr., The Pharmacological Principles of Medical Practice, 7th Edition, Baltimore: Williams and Wilkins, 1969.

135. E.F. Domino, R.D. Hudson and G. Zografi, in Drugs Affecting the Central Nervous System, edited by A. Burger, New York: Dekker, 1968, p. 327 ff.

136. C.L. Zirkle and C. Kaiser, in Medicinal Chemistry, 3rd Edition, Part II, edited by A. Burger, New York: Wiley-Interscience, 1970, p. 1410 ff.

137. T. Charpentier, U.S. Patent 2,519,886 (1950); U.S. Patent 2,530,451 (1950).

138. S. Courvoisier, J. Fournel, R. Ducrot, M. Kolsky and P. Koetschet, Arch. Int. Pharmacodyn. 92, 305 (1952).

139. J. Delay, P. Deniker and J.M. Harl, Ann. Med. Psychol. 110, 112 (1952).

140. H.E. Lehmann and G.E. Hanrahan, Arch. Neurol. Psychiat. 71, 227 (1954).

141. E. Schenker and H. Herbst, Prog. Drug Res. 5, 260 (1963).

142. P. Bradley, Physiol. Pharmacol. 1A, 417 (1963).

143. M. Gordon, in Medicinal Chemistry, 2nd Edition, edited by A. Burger, New York: Wiley Interscience, 1960, p. 397 ff.

144. M. Gordon, in Psychopharmacological Agents, Volume II, edited by M. Gordon, New York: Academic, 1967, p. 1 ff.

145. C. Bodea and I. Silberg, Adv. Heterocyclic Chem. 9, 321 (1968).

146. A. Korolkovas, Essentials of Molecular Pharmacology, New York: Wiley-Interscience, 1970.

147. C.C. Porter and C.A. Stone, Ann. Rev. Pharmacol. 7, 15 (1967).

148. C.J. Cavallito, Ann. Rev. Pharmacol. 8, 39 (1968).

149 J.G. Wagner, Ann. Rev. Pharmacol. 8, 67 (1968).

150 J.H. Peters, Ann. Rev. Pharmacol. 8, 427 (1968).

151 L.E. Hollister, Ann. Rev. Pharmacol. 8, 491 (1968).

152 P.S. Portoghese, Ann. Rev. Pharmacol. 10, 51 (1970).

153 H.E. Himwich and H.S. Alpers, Ann. Rev. Pharmacol. 10, 313 (1970).

154. A. Albert, Ann. Rev. Pharmacol. 11, 13 (1971).

155 I. Izquierdo and J.A. Izquierdo, Ann. Rev. Pharmacol. 11, 189 (1971).

156 H. Fenner, Pharmakopsychiat. Neuro-Psychopharmakol. 11, 189 (1972).

157 H. Fenner, Deut. Apoth.-Ztg. 111, 1495 (1971).

158 M. Wilhelm and R. Kuhn, Pharmakopsychiat. Neuro-Psychopharmakol. 3, 317 (1970).

159 C. Kaiser, A.M. Pavloff, E. Garvey, P.J. Fowler, D.H. Tedeschi and C.L. Zirkle, J. Med. Chem. 15, 665 (1972).

160 M. Hoang and J.W. Daly, J. Med. Chem. 15, 458 (1972).

161 P.R. Andrews, J. Med. Chem. 15, 1069 (1972).

162 M.K. Orloff and D.D. Fitts, Biochim. Biophys. Acta 47, 596 (1961).

163. B. Pullman, in *Electronic Aspects of Biochemistry*, edited by B. Pullman, New York: Academic, 1964, p. 559 ff.

164 L.B. Kier, *Molecular Orbital Theory in Drug Research*, New York: Academic, 1971.

165 A.E. Takemori, Ann. Rev. Biochem. 43, 15 (1974).

166. T.K. Lin, J. Med. Chem. 17, 151 (1974).

167. C. Kaiser, P.J. Fowler, D.H. Tedeschi, B.M. Lester, E. Garvey, C.L. Zirkle, N.A. Nedliff and A.J. Saggiomo, J. Med. Chem. 17, 57 (1974).

168 C. Kaiser, R.J. Warren and C.L. Zirkle, J. Med. Chem. 17, 131 (1974).

169 H.R. Mahler and E.H. Cordes, *Biological Chemistry*, 1st Edition, New York: Harper & Row, 1966.

170 E.E. Conn and P.K. Stumpf, *Outlines of Biochemistry*, 2nd Edition, New York: Wiley, 1966.

171 P. Karlson, *Introduction to Modern Biochemistry*, 3rd Edition, New York: Academic, 1968.

172. A White, P Handler and E L Smith, Principles of Biochemistry, 4th Edition, New York McGraw-Hill, 1968

173. G E Wilkinson, in Comprehensive Biochemistry, Volume 8, Part 2, edited by M Florkin and E H Stotz, New York Elsevier, 1963, p. 289 ff

174. J M Clark, Jr., Experimental Biochemistry, San Francisco: Freeman, 1964

175. E Chargaff and R Lipshitz, J. Amer Chem Soc 75, 3658 (1953).

176. J.D. Watson and F.H.C. Crick, Nature 171, 737 (1953)

177. J.D. Watson and F H C Crick, Nature 171, 964 (1953)

178. P H von Hippel and J D McGhee, Ann Rev Biochem 41, 231 (1972)

179. J E. Hearst and M Botchan, Ann Rev Biochem. 39, 151 (1970)

180. C. Attardi and F Amaldi, Ann Rev Biochem 39, 183 (1970)

181. P T. Gilham, Ann Rev Biochem 39, 227 (1970).

182. C.R. Cantor and C Katz, Ann Rev. Phys Chem 22, 25 (1971)

183. I.H. Goldberg and P A Friedman, Ann Rev Biochem 40, 775 (1971)

184. M Goulian, Ann Rev Biochem 40, 855 (1971)

185. D.R Helinski and D B Clewell, Ann. Rev Biochem 40, 899 (1971)

186. D H Gauss, F von der Haar, A Maelicke and F Cramer, Ann. Rev Biochem, 40, 1045 (1971)

187. A Klein and F Bonhoeffer, Ann Rev Biochem. 41, 301 (1972)

188. P Borst, Ann Rev Biochem 41, 333 (1972)

189. C.G. Kurland, Ann Rev Biochem 41, 377 (1972)

190. R. Losick, Ann Rev Biochem 41, 409 (1972)

191. M Meselson, R Yuan and J Heywood, Ann Rev Biochem 41, 447 (1972)

192. J P Comstock and W F Anderson, Adv Gerontol Res 4, 81 (1972)

193. R.G. Cutler, Adv Gerontol Res 4, 219 (1972)

194. C Weissmann, M A Billeter, H M Goodman, J Hindley and H Weber, Ann Rev Biochem 42, 303 (1973)

195. R A Weinberg, Ann Rev Biochem 42, 329 (1973)

196. J.A. Huberman, Ann. Rev. Biochem. 42, 335 (1973).

197. B.A. Hamkalo and O.L. Miller, Jr., Ann. Rev. Biochem. 42, 379 (1973).

198. U.Z. Littauer and H. Inouye, Ann. Rev. Biochem. 42, 439 (1973).

199. H.B. Younghusband and R.B. Inman, Ann. Rev. Biochem. 43, 605 (1974).

200. D.D. Brown and R. Stern, Ann. Rev. Biochem. 43, 667 (1974).

201. H. Kasamatsu and J. Vinograd, Ann. Rev. Biochem. 43, 695 (1974).

202. W.A. Salser, Ann. Rev. Biochem. 43, 923 (1974).

203. J.M. Gottesfeld, J. Bonner, G.K. Radda and I.O. Walker, Biochem. 13, 2937 (1974).

204. L.S. Lerman, J. Mol. Biol. 3, 18 (1961).

205. L.S. Lerman, Proc. Natl. Acad. Sci. U.S. 49, 94 (1963).

206. H.M. Sobell, Prog. Nucleic Acid Res. Mol. Biol. 13, 153 (1973).

207. H.M. Sobell, Sci. Amer. 231(2), 82 (1974).

208. V.E. Marquez, J.W. Cranston, R.W. Ruddon and J.H. Burckhalter, J. Med. Chem. 17, 856 (1974).

209. S. Ohnishi and H.M. McConnell, J. Amer. Chem. Soc. 87, 2293 (1965).

210. J.-B. LePecq and C. Paoletti, J. Mol. Biol. 27, 87 (1967).

211. N.F. Ellerton and I. Isenberg, Biopolymers 8, 767 (1969).

212. L.M. Chan and Q. Van Winkle, J. Mol. Biol. 40, 491 (1969).

213. V. Kleinwachter, Z. Balcarova and J. Bohacek, Biochim. Biophys. Acta 174, 188 (1969).

214. S. Aktipis and W.W. Martz, Biochem. 13, 112 (1974).

215. R.D. Wells, Progress in Molecular and Subcellular Biology, New York: Springer-Verlag, 1971, p. 21.

216. E.J. Gabbay, R. DeStefano and K. Sanford, Biochem. Biophys. Res. Commun. 46, 155 (1972).

217. E.J. Gabbay, R.E. Scofield and C.S. Baxter, J. Amer. Chem. Soc. 95, 7850 (1973).

218. P.E. Brown, Biochim. Biophys. Acta 213, 282 (1970).

219. S. Ehrenpreis, Prog. Drug Res. 14, 59 (1970).

220. P. Hele, Biochim. Biophys. Acta 76, 647 (1963).

221. L.H. Piette, G. Bulow and I. Yamazaki, Biochim. Biophys. Acta 88, 120 (1964).

222. F. Passero, E.J. Gabbay, B. Gaffney and T. Kurucsev, Macromolecules 3, 158 (1970).

223. D.C. Borg and G.C. Cotzias, Proc. Natl. Acad. Sci. U.S. 48, 617 (1962).

224. D.C. Borg and G.C. Cotzias, Proc. Natl. Acad. Sci. U.S. 48, 623 (1962).

225. D.C. Borg and G.C. Cotzias, Proc. Natl. Acad. Sci. U.S. 48, 643 (1962).

226. G.W. Schleser and L.D. Tuck, J. Pharm. Sci. 51, 694 (1962).

227. L.H. Piette and I.S. Forrest, Biochim. Biophys. Acta 57, 419 (1962).

228. J.P. Lloyd and G.E. Pake, Phys. Rev. 94, 574 (1954).

229. J.B. Burgess, J. Phys. Radium 19, 845 (1958).

230. D.J. Cram and R.A. Reeves, J. Amer. Chem. Soc. 80, 3094 (1958).

231. J.E. Wertz, D.C. Reitz and F. Dravnieks, in Free Radicals in Biological Systems, edited by M.S. Blois, Jr., New York: Academic, 1961, p. 183.

232. R.J. Faber and G.K. Fraenkel, J. Chem. Phys. 47, 2462 (1967).

233. B. Segal, M. Kaplan and G. Fraenkel, J. Chem. Phys. 43, 4191 (1965).

234. J.A. Weil and J.K. Anderson, J. Chem. Soc., 5567 (1965).

235. D.F. Williams, J. Chem. Soc., 7535 (1965).

236. Model 355 Syringe Pump Instruction Manual, Cambridge, Massachusetts: Sage Instruments, 1973.

237. Y. Beers, Introduction to the Theory of Error, Reading, Massachusetts: Addison-Wesley, 1957.

238. R.D. Bowman and N. Davidson, Biopolymers 11, 2601 (1965).

239. Chemical Engineers' Handbook, 4th Edition, edited by R.H. Perry, C.H. Chilton and S.D. Kirkpatrick, New York: McGraw-Hill, 1963, p. 5-34.

240. K.J. Mysels, Introduction to Colloid Chemistry, New York: Wiley Interscience, 1959.

241. W.F. Hughes and J.A. Brighton, Theory and Problems of Fluid Dynamics, New York: McGraw-Hill, 1967.

242. R. V. Giles, Fluid Mechanics and Hydraulics, 2nd Edition, New York: McGraw-Hill, 1962.

243. C. Tanford, Physical Chemistry of Macromolecules, New York: Wiley, 1961.

244. R. E. Harrington, Biopolymers 6, 105 (1968).

245. C. S. Lee and N. Davidson, Biopolymers 6, 531 (1968).

246. F. F. H. Yew and N. Davidson, Biopolymers 6, 659 (1968).

247. P. R. Callis and N. Davidson, Biopolymers 7, 335 (1969).

248. L. S. Lerman, J. Mol. Biol. 10, 367 (1964).

249. H. M. McConnell and R. W. Fessenden, J. Chem. Phys. 31, 1688 (1959).

250. N. Edelstein, A. Kwok and A. H. Maki, J. Chem. Phys. 41, 179 (1964).

251. H. M. McConnell, J. Chem. Phys. 24, 764 (1956).

252. H. M. McConnell and D. B. Chesnut, J. Chem. Phys. 28, 107 (1958).

253. H. M. McConnell and R. E. Robertson, J. Phys. Chem. 61, 1018 (1957).

254. L. Levy, T. N. Tozer, L. D. Tuck and D. B. Loveland, J. Med. Chem. 15, 898 (1972).

255. R. Fenner, Archiv Pharm. 304, 36 (1971).

256. H. Fenner, Archiv Pharm. 304, 47 (1971).

257. J. V. Martinez, Ph.D. Dissertation, University of Florida, 1974.

258. J. Bonner, M. E. Dahmus, D. Fambrough, R. C. Huang, K. Marushige and D. Y. H. Tuan, Science 159, 47 (1968).

259. K. D. Bowers and J. Owen, Reports Prog. Phys. 18, 304 (1955).

260. B. Carnahan, H. A. Luther and J. O. Wilkes, Applied Numerical Methods, New York: Wiley, 1969, p. 250 ff.

261. G. E. Forsythe and P. Henrici, Trans. Amer. Math. Soc. 94, 1 (1960).

262. F. W. Merrill and C. L. Smith, FORTRAN IV Programming for Engineers and Scientists, Scranton, Pennsylvania: International Textbook, 1968.

263. R. H. Pennington, Introductory Computer Methods and Numerical Analysis, New York: MacMillan, 1965.

BIOGRAPHICAL SKETCH

Clifton Howard Durham, Jr., was born on January 24, 1947, in Temple, Texas, and is the son of Mr. and Mrs. Clifton H. Durham of Austin, Texas. He graduated from Pecos High School, Pecos, Texas, as Valedictorian in May, 1965, and entered the University of Texas at Austin in September, 1965. In August, 1970, he was graduated *cum laude* from the University of Texas at Austin with a Bachelor of Science in Chemistry and a Bachelor of Arts with a major in Mathematics. Since September, 1970, he has pursued a course of study leading to a Doctor of Philosophy degree in Chemistry at the University of Florida, Gainesville, Florida. He is a member of the American Chemical Society. Clifton Howard Durham, Jr., is married to Susan Diane Baughman and has one child.

I certify that I have read this study and that in my opinion it conforms to acceptable standards of scholarly presentation and is fully adequate, in scope and quality, as a dissertation for the degree of Doctor of Philosophy

William Weltner Jr

William Weltner, Jr., Chairman
Professor of Chemistry

I certify that I have read this study and that in my opinion it conforms to acceptable standards of scholarly presentation and is fully adequate, in scope and quality, as a dissertation for the degree of Doctor of Philosophy

Wallace S Brey Jr

Wallace S. Brey, Jr.
Professor of Chemistry

I certify that I have read this study and that in my opinion it conforms to acceptable standards of scholarly presentation and is fully adequate, in scope and quality, as a dissertation for the degree of Doctor of Philosophy.

Samuel O. Colgate

Samuel O. Colgate
Associate Professor of Chemistry

I certify that I have read this study and that in my opinion it conforms to acceptable standards of scholarly presentation and is fully adequate, in scope and quality, as a dissertation for the degree of Doctor of Philosophy.

Edward J. Gabbay
Associate Professor of Chemistry

I certify that I have read this study and that in my opinion it conforms to acceptable standards of scholarly presentation and is fully adequate, in scope and quality, as a dissertation for the degree of Doctor of Philosophy

Kenneth C. Leibman

Kenneth C. Leibman
Professor of Pharmacology

This dissertation was submitted to the Graduate Faculty of the Department of Chemistry in the College of Arts and Sciences and to the Graduate Council, and was accepted as partial fulfillment of the requirements for the degree of Doctor of Philosophy.

December, 1974

Dean, Graduate School